

AD-A201 081

NTIC FILE COPY

25072.1-EG-SBI

VRA-TR-88-01

(2)

PNS PREDICTIONS OF  
LARGE-ANGEL-OF-ATTACK  
VISCOS HYPERSONIC FLOWS

BILAL A. BHUTTA and CLARK H. LEWIS

VRA, Inc.  
Post Office Box 50  
Blacksburg, Va 24060

SBIR Phase I Final Report for Period  
July 1987 thru January 1988

Contract No. DAAL03-87-C-0015

March 1988

DTIC  
ELECTED  
OCT 1 9 1988  
S D  
H

DISTRIBUTION STATEMENT A  
Approved for public release;  
Distribution Unlimited

88 10 10 003

ADA201081

UNCLASSIFIED

SECURITY CLASSIFICATION OF THIS PAGE

MASTER COPY

FOR REPRODUCTION PURPOSES

## REPORT DOCUMENTATION PAGE

1a. REPORT SECURITY CLASSIFICATION <u>Unclassified</u>		1b. RESTRICTIVE MARKINGS	
2a. SECURITY CLASSIFICATION AUTHORITY		3. DISTRIBUTION/AVAILABILITY OF REPORT Approved for public release; distribution unlimited.	
2b. DECLASSIFICATION/DOWNGRADING SCHEDULE			
4. PERFORMING ORGANIZATION REPORT NUMBER(S)		5. MONITORING ORGANIZATION REPORT NUMBER(S) ARO 25072.1-EG-SBI	
6a. NAME OF PERFORMING ORGANIZATION VRA, Inc.	6b. OFFICE SYMBOL (If applicable)	7a. NAME OF MONITORING ORGANIZATION U. S. Army Research Office	
6c. ADDRESS (City, State, and ZIP Code) Post Office Box 50 Blacksburg, VA 24060		7b. ADDRESS (City, State, and ZIP Code) P. O. Box 12211 Research Triangle Park, NC 27709-2211	
8a. NAME OF FUNDING/SPONSORING ORGANIZATION U. S. Army Research Office	8b. OFFICE SYMBOL (If applicable)	9. PROCUREMENT INSTRUMENT IDENTIFICATION NUMBER DAAL03-87-C-0015	
8c. ADDRESS (City, State, and ZIP Code) P. O. Box 12211 Research Triangle Park, NC 27709-2211		10. SOURCE OF FUNDING NUMBERS PROGRAM ELEMENT NO.      PROJECT NO.      TASK NO.      WORK UNIT ACCESSION NO.	
11. TITLE (Include Security Classification) PNS Predictions of Large-Angel-Of-Attack Viscous Hypersonic Flows			
12. PERSONAL AUTHOR(S) Bilal A. Bhutta and Clark H. Lewis			
13a. TYPE OF REPORT Final	13b. TIME COVERED FROM 7/1/87 TO 1/31/88	14. DATE OF REPORT (Year, Month, Day) March 1988	15. PAGE COUNT 123
16. SUPPLEMENTARY NOTATION The view, opinions and/or findings contained in this report are those of the author(s) and should not be construed as an official Department of the Army position, policy, or decision, unless so designated by other documentation.			
17. COSATI CODES FIELD      GROUP      SUB-GROUP		18. SUBJECT TERMS (Continue on reverse if necessary and identify by block number)	
19. ABSTRACT (Continue on reverse if necessary and identify by block number)			
20. DISTRIBUTION/AVAILABILITY OF ABSTRACT <input type="checkbox"/> UNCLASSIFIED/UNLIMITED <input type="checkbox"/> SAME AS RPT. <input type="checkbox"/> DTIC USERS		21. ABSTRACT SECURITY CLASSIFICATION Unclassified	
22a. NAME OF RESPONSIBLE INDIVIDUAL		22b. TELEPHONE (Include Area Code)	22c. OFFICE SYMBOL

## PROJECT SUMMARY

Over the last several years a real need has emerged for numerical schemes to predict hypersonic flows around three-dimensional configurations. Recently, the Army has shown considerable interest in applying 3-D PNS schemes to study supersonic/hypersonic flowfields around projectiles and missiles. Although the existing noniterative PNS schemes offer an attractive combination of accuracy and affordability, such schemes suffer from several numerical instability and inaccuracy problems. In this SBIR Phase I effort we have developed a new 3-D PNS scheme with significantly enhanced stability and accuracy characteristics. This work was done by VRA, Inc., for US Army under contract number DAAL03-87-C-0015. Dr. Clark H. Lewis was the principal investigator for this work, and Dr. Thomas L. Doligalski of the Army Research Office, Durham, NC, served as the contract monitor.

In this SBIR Phase I study a new three-dimensional fully-iterative PNS scheme has been developed to study viscous hypersonic flows at large angles of attack. The three-dimensional PNS scheme developed under this SBIR Phase I effort is inherently stable in the subsonic as well as the supersonic flow regions and, thus, does not require any sublayer approximation. Furthermore, it uses a generalized PNS formulation to treat perfect-gas and equilibrium-air gas models in a unified manner. A second-order smoothing approach is used to damp the solution oscillations, while a pseudo-unsteady approach is used to dramatically improve the solution efficiency without compromising the solution accuracy. A new fully-implicit and crossflow-coupled shock-fitting approach has been developed, along with a new predictor-corrector solution scheme to treat large crossflow separated regions.

In order to test this new 3D-PNS scheme we studied the flow around a 15 deg sphere-cone configuration at a Mach number of 10.6 and an angle of attack of 20 deg. This test case corresponds to one of the wind-tunnel tests conducted by Cleary (1969). Four different calculations were done to evaluate the effects of grid refinement and gas model, and the numerical predictions were compared with the available experimental data on wall heat-transfer rates. The results are very encouraging and fully substantiate the accuracy, efficiency and stability claims of the new fully-iterative three-dimensional PNS scheme.

PROJECT SUMMARY

Accession For	
NTIS GRA&I <input checked="" type="checkbox"/>	
DTIC TAB <input type="checkbox"/>	
Unannounced <input type="checkbox"/>	
Justification	
By _____	
Distribution/	
Availability Codes	
Dist	Avail and/or Special
R-1	

## TABLE OF CONTENTS

<b>I. INTRODUCTION .....</b>	<b>1</b>
<b>II. GOVERNING EQUATIONS .....</b>	<b>4</b>
2.1. Coordinate System .....	4
2.2. Governing Equations .....	6
<b>III. NUMERICAL SOLUTION SCHEME .....</b>	<b>8</b>
3.1. Delta-Form of the Governing Equations .....	8
3.1.1. Perfect-Gas Model .....	8
3.1.2. Equilibrium-Air Gas Model .....	11
3.2. Predictor-Corrector Solution Scheme .....	12
3.2.1. Predictor Step .....	13
3.2.2. Crossflow-Coupled Shock Solution .....	14
3.2.3. Corrector Step .....	14
3.3. Pseudo-Unsteady Solution Algorithm .....	15
3.4. Boundary Conditions .....	16
3.4.1. Initial Conditions .....	17
3.3.2. Wall Boundary Conditions .....	17
3.3.3. Boundary Conditions at the Shock .....	18
3.3.4. Circumferential Boundary Conditions .....	18
<b>IV. FULLY-IMPLICIT SHOCK-FITTING PROCEDURE .....</b>	<b>19</b>
4.1. Development of the Shock-Fitting Equations .....	19
4.2. Coupling of the Shock-Point Solution With the Inner Flowfield .....	26
<b>V. A SIMPLIFIED ANALYSIS FOR DEPARTURE .....</b>	<b>28</b>
5.1. Inviscid Limit .....	31
5.2. Viscous Limit .....	32
<b>VI. RESULTS AND DISCUSSION .....</b>	<b>34</b>
6.1. Perfect-Gas Calculations .....	35
6.1.1. Predictions of Surface-Measurable Quantities .....	35
6.1.2. Shock-Shape Predictions .....	36
6.1.3. Effects of Crossflow Grid Refinement .....	37
6.2. Equilibrium-Air Calculations .....	38
6.3. Computing Times .....	40
<b>VII. CONCLUSIONS .....</b>	<b>42</b>
<b>Appendix A. DERIVATION OF 3-D PNS EQUATIONS .....</b>	<b>45</b>
<b>Appendix B. EXPRESSIONS FOR THE JACOBIAN MATRICES .....</b>	<b>51</b>
<b>Appendix C. SECOND-ORDER ACCURATE SMOOTHING TERMS .....</b>	<b>55</b>
<b>Appendix D. A MODEL DIFFERENTIAL/ALGEBRAIC MARCHING PROBLEM ..</b>	<b>59</b>
D.1. Formulation I .....	61
D.2. Formulation II .....	62
D.3. Numerical Solution of the Model Problem .....	67
D.3.1. Explicit Lax Method .....	69
D.3.2. Bidiagonal Implicit Method .....	73

D.3.3. Concluding Remarks on the Numerical Solution .....	77
<b>REFERENCES .....</b>	<b>91</b>

## LIST OF ILLUSTRATIONS

Figure 1. Coordinate system. . . . .	96
Figure 2. Coordinate transformation. . . . .	97
Figure 3. Sphere-cone vehicle geometry. . . . .	98
Figure 4. Axial distribution of wall pressures. . . . .	99
Figure 5. Crossflow distribution of wall pressures. . . . .	100
Figure 6. Axial distribution of skin-friction coefficient. . . . .	101
Figure 7. Crossflow distribution of skin-friction coefficient. . . . .	102
Figure 8. Axial distribution of wall heat-transfer rates. . . . .	103
Figure 9. Crossflow distribution of wall heat-transfer rates. . . . .	104
Figure 10. Axial variation of bow shock shape. . . . .	105
Figure 11. Crossflow variation of bow shock shape. . . . .	106
Figure 12. Effects of crossflow grid refinement on the wall heat-transfer rates. .	107
Figure 13. Effects of crossflow grid refinement on the crossflow skin-friction coefficient. . . . .	108
Figure 14. Effects of gas model on the axial distribution of wall pressures. . . . .	109
Figure 15. Effects of gas model on the crossflow distribution of wall pressures. .	110
Figure 16. Effects of gas model on the axial distribution of the skin-friction coefficient. . . . .	111
Figure 17. Effects of gas model on the crossflow distribution of the skin-friction coefficient. . . . .	112
Figure 18. Effects of gas model on the axial distribution of the wall heat-transfer rates. . . . .	113
Figure 19. Effects of gas model on the crossflow distribution of the wall heat-transfer rates. . . . .	114
Figure 20. Effects of gas model on the axial variation of the bow shock shape. .	115
Figure 21. Effects of gas model on the crossflow variation of the bow shock shape. .	116

Figure 22. Crossflow separated region predicted with a perfect-gas model. . . . .	117
Figure 23. Crossflow separated region predicted with an equilibrium-air model. .	118
Figure 24. Detailed leeward pressure contours predicted using a perfect-gas model. .	119
Figure 25. Detailed leeward pressure contours predicted using a equilibrium-air model. . . . .	120
Figure 26. Effects of gas model on the crossflow pressure contours. . . . .	121
Figure 27. Effects of gas model on the crossflow temperature contours. . . . .	122
Figure 28. Effects of gas model on the crossflow density contours. . . . .	123

## LIST OF TABLES

Table 1. Freestream conditions for test case .....	94
Table 2. Comparison of total computing times .....	95

## NOMENCLATURE

$a$	= local speed of sound
CFS	= streamwise skin-friction coefficient
CFW	= crossflow skin-friction coefficient
$C_p$	= specific heat at constant pressure
$h$	= static enthalpy of the mixture
$J$	= determinant of the transformation Jacobian
$k$	= mixture thermal conductivity
M	= Mach number
$m_{njk}$	= $\xi_{n,x_j} \xi_{n,x_k}$
n	= iteration number
$P, p$	= static pressure
PHI	= circumferential angle measured from the windward side, $\phi$
PINF	= freestream static pressure, $p_\infty$
Pr	= Prandtl number
PW	= wall pressure
QW	= total wall heat-transfer rate in Btu/ft <sup>2</sup> /sec
RB	= local body radius
Re	= Reynolds number, $(\rho^* V^* Rn^*) / \mu^*$
RN, Rn	= nose radius
RSHK	= radial location of the bow shock

T	= static temperature
t	= time
u	= x-component of mass-averaged velocity
$u_j$	= u, v and w for $j = 1, 2$ and 3
$U_j$	= contravariant velocities, $u_k \xi_{j,k}$
UINF	= freestream velocity, $V_\infty$
V	= total mass-averaged velocity
v	= y-component of mass-averaged velocity
w	= z-component of mass-averaged velocity
X,x	= coordinate along body axis
$x_j$	= x, y and z for $j = 1, 2$ and 3
$\alpha$	= angle of attack
$\gamma$	= specific-heat ratio
$\epsilon$	= $M_\infty / Re_\infty$
$\mu$	= mixture viscosity
$\xi_1$	= marching or streamwise coordinate
$\xi_2$	= coordinate measured from the body to the outer bow shock
$\xi_3$	= coordinate measured from the windward to the leeward direction
$\rho$	= mixture density
$\phi$	= circumferential angle measured from the windward side

#### Superscript

j	= index in $\xi$ direction
n	= index for iteration
T	= vector or matrix transpose
*	= dimensional quantity

#### Subscript

,	= represents partial derivative
$\infty$	= freestream quantity
i	= represents i-th chemical species
j,k,l	= indicial notation representing 1, 2 and 3
s	= shock quantity
w	= wall quantity

#### Vector and Matrix Notation

Vector	= bold lower-case character
Matrix	= bold upper-case character
•	= vector dot product

## I. INTRODUCTION

Over the past several years significant advances have been made in the field of Computational Fluid Mechanics (CFD). Several recent advances in computer facilities, their speed and storage capabilities have made it possible to develop accurate and sophisticated numerical prediction schemes for various high-speed, fluid-flow problems. On the other hand the development of high-speed experimental facilities and their operation has remained as an extremely expensive option.

The existing methodology for external-flow prediction over ballistic geometries consists of Navier-Stokes (NS), Parabolized Navier-Stokes (PNS) and Viscous Shock-Layer (VSL) schemes. The NS schemes (Sahu, 1986; Sahu, 1987, Sahu and Nietubicz, 1987; Richardson, 1986; Kumar, 1986; and Rizk et al., 1981) are typically very time consuming and not well suited for various parametric studies required for design and analysis purposes. On the other hand, the existing noniterative PNS schemes (Weinacht et al., 1986; Guidos and Sturek, 1987; Kaul and Chaussee, 1983; and Stalnaker, 1985) suffer from instabilities and inaccuracies. Apart from being noniterative, such PNS schemes require a substantial approximation in the way the subsonic sublayer region is treated. There are generally large global conservation-of-mass (as well as momentum and energy) errors associated with these PNS methods, which originate from the basic solution scheme.

The existing VSL schemes (Thareja et al., 1983a and 1983b; Thompson et al., 1983; and Bhutta et al., 1985b) have a basic limitation of being parabolic in the crossflow direction and, consequently, can not march through crossflow separated regions. This prevents the VSL scheme from accurately predicting the aerodynamic response of complex projectile/missile configurations, which may experience strong crossflow separation either due a large-angle-of-attack condition or simply due the 3-D nature of the geometry being considered (such as finned configurations, etc.). However, even under these conditions the flowfield in the nose region is attached, and the VSL schemes represent an accurate and efficient way of generating the nose solutions for starting other (more accurate) afterbody methods which can treat crossflow separation (such as the PNS schemes).

In this Phase I effort we have extended our basic PNS scheme to study three-dimensional supersonic/hypersonic flowfields using a general curvilinear coordinate system. However, only axisymmetric geometries have been considered in this Phase I study. Treatment of complex three-dimensional geometries requires additional considerations related to grid generation and geometry modeling, and will be addressed in the follow-on Phase II effort. In this Phase I study substantial effort was also devoted to the development of a new fully-implicit and crossflow-coupled shock-fitting scheme in which the bow shock shape is predicted as the solution marches down the body. Furthermore, a new predictor-corrector solution scheme was developed and used to treat the strong crossflow coupling effects in and around the crossflow separated region. This 3-D perfect-gas PNS scheme was further extended to include an equilibrium-air gas model.

The 3-D PNS scheme developed under this Phase I effort can treat flows over a Mach number range of 3 to 30 and for freestream Reynolds numbers as low as  $10^3$  (based on

nose radius). The present scheme has been tested for angles of attack up to 20 deg; however, it should also be applicable at higher angles of attack as long as the flow remains axially attached. Although this Phase I study was restricted to laminar flows, the solution scheme can be easily extended to include turbulent flow modeling.

This final report discusses in detail the various mathematical and numerical developments done under this Phase I effort. One large angle of attack test case was considered to validate and demonstrate this 3-D PNS capability. This test case deals with the flow over a sphere-cone vehicle at a Mach number of 10.6 and an angle of attack of 20 deg. These conditions correspond to one of the test cases studied by Cleary (1969), and was chosen because in this case most of the flow was laminar (except for some turbulence effects on the lee side). Both perfect-gas and equilibrium-air gas models were used to study this test case. Perfect-gas flowfield predictions were done using three different computational grids (Cases 1, 2, and 3), and the results were compared with the experimental predictions. The equilibrium-air flowfield predictions were done using a fine crossflow grid (Case 4), which was similar to the fine grid used for the corresponding perfect-gas calculations (Case 1). The results of these numerical tests are very encouraging and demonstrate quite well the various salient features of the new 3-D PNS scheme.

## II. GOVERNING EQUATIONS

### 2.1. Coordinate System

The coordinate system used for the present 3-D PNS scheme is a general curvilinear coordinate system  $(\xi_1, \xi_2, \xi_3)$  shown in Fig. 1. Also, a body-fixed orthogonal (Cartesian) coordinate system is chosen such that the origin of the Cartesian coordinate system is at the tip of the blunt nose, and the x-axis is aligned with the axis of the body. The z-axis is chosen as pointing downward such that the windward surface of the vehicle is on the positive z-axis side (see Fig. 1). For convenience of notation we will also refer to the x coordinate as  $x_1$ , the y coordinate as  $x_2$  and the z coordinate as  $x_3$ .

The  $\xi_1$  coordinate is along the body and is also the marching direction. The  $\xi_2$  coordinate stretches from the body to the outer bow shock and lies in an axis-normal plane. The  $\xi_3$  coordinate is measured in the crossflow direction from the windward pitch plane. In general, it is assumed that the  $(x, y, z)$  space is uniquely transformable to the  $(\xi_1, \xi_2, \xi_3)$  space through relations of the form

$$\xi_j = \xi_j(x, y, z) \quad (2.1)$$

The uniqueness property is automatically satisfied as long as coordinate lines of the same family do not cross, and it is important that the inverse transform of Eq. (2.1) is definable. Suppose we denote the marching step at which we seek the solution as 'j+1' and the previous step as 'j', then the transformation of Eq. (2.1) is chosen such that the physical (x, y, z) grid between 'j' and 'j+1' steps transforms to a rectangle in the computational ( $\xi_1, \xi_2, \xi_3$ ) plane. The body surface corresponds to the  $\xi_2 = 0$  curve, whereas the outer bow shock corresponds to  $\xi_2 = \text{LMAX}$  curve (LMAX being the number of grid points in the  $\xi_2$  coordinate direction). In the windward pitch plane  $\xi_3 = 0$ , and in the leeward pitch plane  $\xi_3 = \text{KMAX}$ , where KMAX is the number of circumferential grid points. Also,  $\xi_1 = 0$  at the j-th step and  $\xi_1 = 1$  at the j+1 step. Thus, at each marching step, every grid cell in the x-y-z space between the j and the j+1 step is transformed into a unit cube in the  $\xi_1, \xi_2, \xi_3$  plane with  $\Delta\xi_1 = \Delta\xi_2 = \Delta\xi_3 = 1$  (see Fig. 2).

The transformation given by Eq. (2.1) is generally difficult to obtain. However, if we assume for the present that the (x, y, z) grid at the j+1 step were known (subsequent sections will discuss this in more detail), then the metric derivatives for the inverse transform

$$x_j = x_j(\xi_1, \xi_2, \xi_3) \quad (2.2)$$

can be easily obtained numerically. At each grid point, this information about the inverse-transform metrics is used to determine the transformation Jacobians (J) and the metric derivatives ( $\xi_{j,x_i}$ ) for the transformation given by Eq. (2.1).

## 2.2. Governing Equations

The full Navier-Stokes equations governing the three-dimensional flow problem can be written in a nondimensional form as (see Appendix A)

$$(e_j - \varepsilon g_j)_{,x_j} = p \quad (2.3)$$

We choose our unknowns to be the density ( $\rho$ ), the density-velocity products ( $\rho u$ ,  $\rho v$  and  $\rho w$ ), the density-temperature product ( $\rho T$ ) and the pressure ( $p$ ). Thus our vector of unknowns is

$$\mathbf{q} = [\rho, \rho u, \rho v, \rho w, \rho T, p]^T \quad (2.4)$$

Following the approach of Peyret and Viviand (1975), it can be shown that Eq. (2.3) can be transformed into the general curvilinear coordinate system ( $\xi_j$ ), i.e.,

$$(f_j - \varepsilon s_j)_{,\xi_j} = h \quad (2.5)$$

It is assumed that in the freestream the gas mixture behaves like a perfect gas, and the nondimensionalization used in the above equations is shown in Appendix A.

Equation (2.5) is elliptic in  $\xi_1$ ,  $\xi_2$  and  $\xi_3$  directions. If we neglect the viscous dissipation effects in the  $\xi_1$  direction, we can combine Eqs. (2.5) and (2.3) in the following vectorial equation:

$$f_{j,\xi_j} - \varepsilon s_{2,\xi_2} - \varepsilon s_{3,\xi_3} = h \quad (2.6)$$

where the various components of this vectorial equations are defined in Appendix A.

These five equations representing the differential conservation of mass, momentum and energy are mathematically closed by using the equation of state for the particular gas model being used. This equation of state can be written in a general functional form as

$$f(\rho, T, p) = 0 \quad (2.7)$$

In the case of a perfect-gas model, the gas is assumed to be thermally as well as calorically perfect. The equation of state for this case is written in the simple algebraic form as

$$f(\rho, T, p) = \gamma p - \rho T = 0 \quad (2.8)$$

In the case of an equilibrium-air gas model, the equation of state is written in the following functional form.

$$f(\rho, T, p) = \rho - \rho(p, T) = 0 \quad (2.9)$$

Here the mixture density is a function of pressure and temperature and is available in the form of a table.

## **III. NUMERICAL SOLUTION SCHEME**

This chapter discusses in detail the procedure used to numerically solve the governing PNS equations.

### **3.1. Delta-Form of the Governing Equations**

In this 'delta formulation' we solve for the changes in the flowfield variables from one iteration to the next. The approach used is separately discussed for perfect-gas and equilibrium-air gas models.

#### **3.1.1. Perfect-Gas Model**

Let us denote the iteration level by the index 'n', so that the iteration at which we seek the solution is represented by the superscript 'n + 1', and the previous iteration (the solution to which is known) is represented by the superscript 'n'. Thus, for the 'n + 1' iteration at the 'j + 1' marching step we can write Eq. (2.6) as

$$f_{j,\xi_j}^{j+1,n+1} - \varepsilon s_{2,\xi_2}^{j+1,n+1} - \varepsilon s_{3,\xi_3}^{j+1,n+1} = h^{j+1,n+1} \quad (3.1)$$

If we assume that the solution at the 'n+1' level is close to the solution at the n-th iteration, we can use a first-order Taylor series expansion around the previous iteration to write

$$\begin{aligned} f_j^{j+1,n+1} &\approx f_j^{j+1,n} + A_j^n \cdot \Delta q^{n+1} \\ s_2^{j+1,n+1} &\approx s_2^{j+1,n} + M_2^n \cdot \Delta q^{n+1} \\ s_3^{j+1,n+1} &\approx s_3^{j+1,n} + M_3^n \cdot \Delta q^{n+1} \\ h^{j+1,n+1} &\approx h^{j+1,n} + A_0^n \cdot \Delta q^{n+1} \end{aligned} \quad (3.2)$$

where

$$\Delta q^{n+1} = q^{j+1,n+1} - q^{j+1,n} \quad (3.3)$$

and the matrices  $A_0$ ,  $M_2$  and  $M_3$  are called the jacobian matrices (not to be confused with the transformation Jacobian matrix). The forms of these matrices are given in Appendix B. It should be noted that in evaluating the jacobian matrices and doing the Taylor series expansion around the n-th iteration, we only consider the flowfield variables as the unknowns. Although the grid also changes from one iteration to the next, it is assumed that these changes are small and do not contribute to the jacobian matrices.

Thus, we see that by expanding the solution around the n-th iteration and using two-point streamwise differencing, we can write Eq. (3.1) as

$$\begin{aligned} (A_1/\Delta \xi_1 - A_0)^n \cdot \Delta q^{n+1} - [(A_2^n - \varepsilon M_2^n) \cdot \Delta q^{n+1}]_{,\xi_2} - [(A_3^n - \varepsilon M_3^n) \cdot \Delta q^{n+1}]_{,\xi_3} \\ = - [f_{j,\xi_j} - \varepsilon s_{2,\xi_2} - \varepsilon s_{3,\xi_3} - h]^{j+1,n} = g^{j+1,n} \end{aligned} \quad (3.4)$$

It has been shown by Bhutta and Lewis (1985a-d) and Bhutta et al. (1985a) that for the iterative process of Eq. (3.1), the simple two-point streamwise differencing is conservative in the limit of convergence. This is not only important from a storage point of view, but it also gives the present scheme a significantly improved capability for treating strong compression discontinuities.

Equation (3.1) is elliptic in the  $\xi_2$  and  $\xi_3$  directions so that for second-order accuracy we use central-differenced approximations for all  $\xi_2$  and  $\xi_3$  derivatives. However, the use of central-differenced schemes is typically associated with solution oscillations (Bhutta and Lewis, 1985a-d; Schiff and Steger, 1979; and Shanks et al., 1979). This oscillatory behavior becomes more pronounced if the local velocities are small, so that the diagonal terms of the jacobian matrices become relatively small also. In order to damp these solution oscillations, it is necessary to add some additional higher-order diffusion terms to Eq. (3.1). In our earlier work (Bhutta and Lewis, 1985a-d) we developed a second-order accurate fully-implicit smoothing approach which is accurate and simple to use. It is shown in Appendix C that by extending the basic approach of Bhutta and Lewis (1985a-d) we can write Eq. (3.1) as

$$f_{i,\xi_j}^{j+1,n+1} = \varepsilon s_{2,\xi_2}^{j+1,n+1} + \varepsilon s_{3,\xi_3}^{j+1,n+1} + h^{j+1,n+1} + \pi_1(q)(\Delta\xi_2)^2 + \pi_2(q)(\Delta\xi_3)^2 \quad (3.5)$$

where the form of the vectors  $\pi_1$  and  $\pi_2$  is chosen as

$$\begin{aligned} \pi_1(q) = & \{(A_1/\Delta\xi_1 - A_0) \cdot q,_{\xi_2\xi_2} + [(A_2 - \varepsilon M_2) \cdot q,_{\xi_2\xi_2}]_{\xi_2} + \\ & [(A_3 - \varepsilon M_3) \cdot q,_{\xi_2\xi_2}]_{\xi_3}\}/4 \end{aligned} \quad (3.6a)$$

$$\begin{aligned} \pi_2(q) = & \{(A_1/\Delta\xi_1 - A_0) \cdot q,_{\xi_3\xi_3} + [(A_2 - \varepsilon M_2) \cdot q,_{\xi_3\xi_3}]_{\xi_2} + \\ & [(A_3 - \varepsilon M_3) \cdot q,_{\xi_3\xi_3}]_{\xi_3}\}/4 \end{aligned} \quad (3.6b)$$

It has been shown in Appendix C that (to second-order accuracy) we can rewrite Eq. (3.5) in terms of an intermediate solution  $\chi^{j+1}$  as

$$[f_j(\chi^{j+1})]_{,\xi_j} = \varepsilon[s_2(\chi^{j+1})]_{,\xi_2} + \varepsilon[s_3(\chi^{j+1})]_{,\xi_3} + h(\chi^{j+1}) + O(\Delta\xi_2)^2 + O(\Delta\xi_3)^2 \quad (3.7)$$

The actual solution that we seek at the  $j+1$  step is related to this intermediate solution by

$$(\chi^*)^{j+1} = \chi^{j+1} + \chi_{,\xi_3\xi_3} \Delta\xi_3^2/4 \quad (3.8a)$$

$$q^{j+1} = (\chi^*)^{j+1} + (\chi^*)_{,\xi_2\xi_2} \Delta\xi_2^2/4 \quad (3.8b)$$

For this perfect-gas model the mixture viscosity was obtained using the Sutherland formula (White, 1974), and the specific-heat ratio was assumed to be a constant (1.4 for air). The mixture Prandtl number was also assumed fixed (0.72 for air), and the mixture thermal conductivity was obtained from the definition of mixture Prandtl number.

### 3.1.2. Equilibrium-Air Gas Model

The numerical scheme used for equilibrium-air flows is essentially the same as for the case perfect-gas case, except that the mixture thermodynamic and transport properties are provided in the form of a table. The dependant variables for these tabular data are chosen to be pressure and temperature. The thermodynamic properties involve the mixture enthalpy,  $h(p,T)$ , and mixture density,  $\rho(p,T)$ , data and are based on the tabular data of Miner et al. (1971). The transport properties involve the mixture viscosity data,  $\mu(p,T)$ , the mixture thermal conductivity data,  $k(p,T)$ , and the Prandtl number data,

$\text{Pr}(p,T)$ . The viscosity and thermal conductivity data are based on the data developed by Peng and Pindroh (1962). The Prandtl number data were developed using this viscosity and thermal conductivity data and the mixture specific-heat data obtained by numerically differentiating the aforementioned enthalpy data of Miner et al. (1971). The equilibrium-air thermodynamic and transport property table generated for use in this Phase I study covers the temperature range of 10-15000 Kelvin and the pressure range of 0.0025-15.849 atmospheres. The pressure range of the thermodynamic property data of Miner et al. (1971) is from 0.000025 atmospheres to 39810.72 atmospheres; however, the reduced limits of the current table are due to transport property data of Peng and Pindroh (1962). The orginal transport property data of Peng and Pindroh (1962) are in terms of a table of density and temperature. When these data were rearranged in terms of pressure and temperature, it was observed that out side the limits of 0.0025-15.849 atmospheres, the available data did not completely cover the temperature range of 10-15000 Kelvin. Since a direct extrapolation of these data in terms of pressures may not be accurate, the current table was limited to this pressure and temperature range. It should be noted that this range adequately covers most of the flight regime in which the equilibrium-air effects may be important.

### 3.2. Predictor-Corrector Solution Scheme

Under large angle of attack conditions strong crossflow separated regions may develop on the leeward side. Under these conditions, solution coupling in the crossflow direction is very important. If these coupling effects are not properly considered during the iterative solution, they can cause severe convergence difficulties. In order to address

that problem of crossflow coupling we have developed a new predictor-corrector approach. This predictor-corrector scheme is divided into three different parts; namely, (a) the predictor step, (b) the shock solution and (c) the corrector step. The following discussion summarizes the details of these solution steps.

Using a two-point streamwise differencing and central-differenced approximations in the  $\xi_2$  and  $\xi_3$  directions, the final differenced equations corresponding to Eq. (3.4) can be written in the following block-pentadiagonal form.

$$\begin{aligned}
 & [D \cdot \Delta \chi_{k-1, \ell}] + [A \cdot \Delta \chi_{k, \ell-1}] + [B \cdot \Delta \chi_{k, \ell}] + [C \cdot \Delta \chi_{k, \ell+1}] + [E \cdot \Delta \chi_{k+1, \ell}] \\
 & = -[f_{i, \xi_j} - \varepsilon s_{2, \xi_2} - \varepsilon s_{3, \xi_3} - h]^{j+1, n} = g^{j+1, n}
 \end{aligned} \tag{3.9}$$

### 3.2.1. Predictor Step

In the predictor step we first neglect the implicit crossflow coupling effects in favor of the body-normal coupling effects. With this assumption the governing equations for the predictor step become

$$[A \cdot \Delta \chi_{k, \ell-1}^*] + [B \cdot \Delta \chi_{k, \ell}^*] + [C \cdot \Delta \chi_{k, \ell+1}^*] = g^n \tag{3.10}$$

These equations are inverted from the body to the shock to develop a recursive relationship between the solution at each successive grid point in the body-normal direction. These recursive relations have the form

$$\Delta\chi_{k,\ell}^* = -R_{k,\ell} \cdot \Delta\chi_{k,\ell+1}^* + r_{k,\ell}^n \quad \text{where } k = 1, \dots, KMAX \\ \ell = 1, \dots, LMAX - 1 \quad (3.11)$$

### 3.2.2. Crossflow-Coupled Shock Solution

The crossflow-coupled shock-fitting scheme is discussed in detail in the following section. Briefly speaking, using the recursive relation from the predictor step at  $\ell = (LMAX-1)$  location, the Rankine-Hugoniot shock-crossing equations are solved to obtain the solution at the shock. This shock solution is then used to solve the corrector step.

### 3.2.3. Corrector Step

Just like the shock-point solution, the solution in the corrector step uses the recursive relations from the predictor step to eliminate the  $(k,\ell-1)$  contributions in the difference molecule. Then using the fact that the solution at the  $(k,\ell+1)$  point is known, one can reduce the Eqs. (3.9) to only a coupled system in the crossflow direction. This crossflow corrector solution can be written as

$$D \cdot \Delta\chi_{k-1,\ell} + (B - AR_{k,\ell}) \cdot \Delta\chi_{k,\ell} + E \cdot \Delta\chi_{k+1,\ell} \\ \cong (g^n - A \cdot r_{k,\ell-1}^n) - C \cdot \Delta\chi_{k,\ell+1} \quad (3.12)$$

where it is assumed that

$$\begin{aligned}\Delta \chi_{k,\ell-1} &\cong \Delta \chi_{k,\ell-1}^* = -R_{k,\ell-1} \cdot \Delta \chi_{k,\ell}^* + r_{k,\ell-1}^n \\ &\cong -R_{k,\ell-1} \cdot \Delta \chi_{k,\ell} + r_{k,\ell-1}^n\end{aligned}\quad (3.13)$$

This implicit crossflow solution is obtained using plane-of-symmetry boundary conditions applied in the windward and leeward pitch planes. In this way the flowfield solution is marched from the shock to the body.

### 3.3. Pseudo-Unsteady Solution Algorithm

It should be noted that the right-hand side of Eq. (3.4) as well as the right-hand side of Eq. (3.9) is the governing differential equation corresponding to the fluid mechanics problem written at the  $n$ -th iteration level and goes to zero in the limit of convergence. As discussed by Bhutta and Lewis (1985a-d), under these conditions the exact form of the left-hand implicit terms is of no great consequence except that it affects the convergence path of the solution. With this idea in mind we do not update the Jacobian matrices beyond the first iteration; i.e., we assume that

$$\begin{aligned}A_0^n &\simeq A_0^{n-1} \\ A_j^n &\simeq A_j^{n-1} \\ M_2^n &\simeq M_2^{n-1} \\ M_3^n &\simeq M_3^{n-1}\end{aligned}\quad (3.14)$$

Such a pseudo-unsteady approach has been discussed in depth by Bhutta and Lewis (1985a-d) and interested readers are referred to these references for further details. Using this pseudo unsteady approach we obtain the final differenced equations as

$$\begin{aligned}
 & (A_1/\Delta\xi_1 - A_0)^{n+1} \cdot \Delta\chi^{n+1} + [(A_2 - \varepsilon M_2)^{n+1} \cdot \Delta\chi^{n+1}]_{,\xi_2} + [(A_3 - \varepsilon M_3)^{n+1} \cdot \Delta\chi^{n+1}]_{,\xi_3} \\
 & = - [f_{j,\xi_j} - \varepsilon s_{2,\xi_2} - \varepsilon s_{3,\xi_3} - h]^{j+1,n} = g^{j+1,n}
 \end{aligned} \tag{3.15}$$

The converged limit of Eq. (3.15) is the same as the converged limit of Eq. (3.4). However, Eq. (3.15) is considerably more efficient and faster to solve. With the present pseudo-unsteady approach the time for each iteration after the first iteration ( $n = 2, 3, \dots$ ) is only 10-15% of the time taken by the first iteration.

### 3.4. Boundary Conditions

The problem represented by the governing PNS equations is a split-boundary-value problem; i.e., the equations are hyperbolic-parabolic in the  $\xi_1$  direction and elliptic in the  $\xi_2$  and  $\xi_3$  directions. Thus, in order to solve the problem completely we need initial conditions to be specified at the start of the marching procedure, boundary conditions to be specified at the wall and at the outer bow shock and boundary conditions to be specified in the windward and leeward pitch planes (for flows with a pitch-plane of symmetry).

### 3.4.1. Initial Conditions

The initial conditions to start the perfect-gas and equilibrium-air PNS solutions were obtained from a VSL blunt-body solution scheme for perfect-gas and equilibrium-air flows (Murray and Lewis, 1978; Thareja et al., 1983a; and Thompson et al., 1983). The quality of such VSL solutions has been discussed in great detail by Thompson et al. (1983) and Bhutta et al. (1985b). The VSL blunt-body solution is interpolated to obtain the starting solution at the initial data plane (IDP) for the 3-D PNS afterbody solution. We typically choose the starting location to be approximately 2-3 nose-radii downstream of the nose stagnation-point location.

### 3.3.2. Wall Boundary Conditions

The boundary conditions at the wall consist of six independent relations representing the nature of the gas mixture and the physical conditions at the wall. These conditions are:

- (1) Equation of state of the gas:  $f(\rho, p, T) = 0$
- (2) No-slip condition for 'u' velocity component:  $\rho u = 0$
- (3) No slip condition for 'v' velocity component:  $\rho v = 0$
- (4) No slip condition for 'w' velocity component:  $\rho w = 0$
- (5) Specified wall temperature:  $(\rho T) = \rho T_w$ .

and

- (6) Zero pressure derivative in the  $\xi_2$  direction ( $p_{,\xi_2} = 0$ )

The first five boundary conditions are easy to visualize as they represent the actual physical conditions at the wall. The sixth boundary condition on the pressure derivative comes from a boundary-layer-type analysis performed at the wall. The above set of boundary conditions are well-posed and form a linearly independent set.

### **3.3.3. Boundary Conditions at the Shock**

The boundary conditions at the outer bow shock are, however, much more involved. This boundary condition involves a fully-implicit and crossflow coupled shock-fitting approach, and the bow shock is predicted as the solution marches down the body. This fully-implicit bow shock-fitting scheme will be discussed in detail in Chapter 4.

### **3.3.4. Circumferential Boundary Conditions**

Presently, the proposed three-dimensional nonequilibrium PNS schemes can only treat flows with a pitch plane of symmetry; i.e., the vehicle geometry is symmetric with respect to the pitch plane and there is no yaw. For such a case the boundary conditions at the windward and leeward pitch planes consist of reflective or symmetric boundary conditions. The symmetric and reflective boundary conditions used in the present study are based on the second-order crossflow boundary conditions used by Kaul and Chaussee (1983) and Shanks et al. (1979).

## IV. FULLY-IMPLICIT SHOCK-FITTING PROCEDURE

### 4.1. Development of the Shock-Fitting Equations

In this study we have developed a new fully-implicit and crossflow coupled shock-fitting scheme. In this scheme the bow shock location is iteratively predicted as the solution marches down the body. This chapter provides a brief but complete description of this shock-fitting approach. The important features of this bow shock-fitting approach are:

- (a) The bow-shock shape location is predicted along with the flowfield solution and does not have to be specified a priori.
- (b) Unlike earlier noniterative shock-propagation approaches (Kaul and Chaussee, 1983; Shanks et al., 1979; and Chaussee et al., 1982), the present shock-fitting scheme is fully iterative and treats the various gas models (perfect-gas or equilibrium-air or nonequilibrium-air) accurately and in a unified manner.
- (c) Unlike earlier noniterative shock-propagation approaches (Kaul and Chaussee, 1983; Shanks et al., 1979; and Chaussee et al., 1982), the present approach does not as-

sume the flowfield behind the shock to be inviscid. This can be quite important when strong flowfield gradients exist behind the shock, as may be the case in the nose-dominated region and in regions where the bow shock starts to interact with the imbedded shock waves (or compression waves) originating from the body.

- (d) Unlike the iterative shock-fitting approaches of Helliwell et al. (1980) and Lubard and Helliwell (1973), the present shock fitting approach is not only for a general curvilinear coordinate system but also does not increase the matrix size of the block-tridiagonal solution between the body and the shock.
- (e) Unlike any earlier iterative or noniterative bow shock-fitting scheme, the present shock-fitting scheme does not neglect the crossflow coupling effects at the shock. This results in accurate and smooth shock shapes even when there are strong crossflow variations of the conditions behind the shock. This can be especially important when dealing with complex 3-D configurations (which is one of the main objectives of this study) where the 3-D nature of the body can interact with the bow shock and substantially distort it. Similar strong crossflow variations may also occur on simple configurations when pitched at large angles of attack.

In developing the present bow shock-fitting scheme we assume that from one iteration to the next the shock-points move along the  $\xi_2$  grid line. This direction corresponds to the intersection of the  $\xi_1 = \text{constant}$  and  $\xi_2 = \text{constant}$  surfaces. This assumption allows us to reduce the size of unknowns to be solved, and the final solution has only one additional unknown at the shock which completely defines the spatial movement of the shock point. This smaller size of the unknowns is very important for a faster iterative solution and faster convergence characteristics of the overall implicit shock-prediction scheme. Furthermore, this simplification only represents a certain

constraint on the direction in which the shock-point moves and has no affect on the accuracy of the shock-crossing equations.

Furthermore, in order to simplify the numerical solution, it is assumed that the metric derivatives  $y_{,\xi_2}$  and  $z_{,\xi_2}$  at the shock can be safely assumed as known from the previous iteration; i.e.,

$$\begin{aligned}(y_{,\xi_2})_s^{n+1} &\simeq (y_{,\xi_2})_s^n \\ (z_{,\xi_2})_s^{n+1} &\simeq (z_{,\xi_2})_s^n\end{aligned}\tag{4.1}$$

This is also only a simplification and does not affect the accuracy of the final converged solution. For the case of nonequilibrium-air flows a frozen shock-crossing approximation is used.

Using the first of the aforementioned assumptions we denote the amount by which the shock point moves in the  $\xi_2$  direction as  $\Delta_s$ . In other words

$$(\xi_2)_s^{n+1} \simeq (\xi_2)_s^n + (\Delta)_s^{n+1}\tag{4.2}$$

Thus the corresponding movement of the shock-point coordinates from one iteration to the next can be written as

$$(x_j)_s^{n+1} \simeq (x_j)_s^n + (x_{j,\xi_2})_s^n (\Delta)_s^{n+1}\tag{4.3}$$

Furthermore, we define a set of six unknowns ( $\alpha_i$ ) such that

$$\begin{aligned}
\alpha_1^{n+1} &= (x_{,\xi_1})_s^{n+1} \\
\alpha_2^{n+1} &= (y_{,\xi_1})_s^{n+1} \\
\alpha_3^{n+1} &= (z_{,\xi_1})_s^{n+1} \\
\alpha_4^{n+1} &= (y_{,\xi_3})_s^{n+1} \\
\alpha_5^{n+1} &= (z_{,\xi_3})_s^{n+1}
\end{aligned} \tag{4.4}$$

Where it should be noted that these five unknowns are actually functions of a single unknown  $(\Delta_s)^{n+1}$  such that

$$\begin{aligned}
\alpha_1^{n+1} &= \alpha_1^n + (x_{,\xi_2})_s^n \Delta_s^{n+1} \\
\alpha_2^{n+1} &= \alpha_2^n + (y_{,\xi_2})_s^n \Delta_s^{n+1} \\
\alpha_3^{n+1} &= \alpha_3^n + (z_{,\xi_2})_s^n \Delta_s^{n+1} \\
\alpha_4^{n+1} &= \alpha_4^n + [(y_{,\xi_2})_s^n \Delta_s^{n+1}]_{,\xi_3} \\
\alpha_5^{n+1} &= \alpha_5^n + [(z_{,\xi_2})_s^n \Delta_s^{n+1}]_{,\xi_3}
\end{aligned} \tag{4.5}$$

At this point we define three orthogonal vector directions  $\mathbf{n}$ ,  $\mathbf{t}$  and  $\mathbf{s}$  at the shock surface (note that these are not unit vectors). The vector  $\mathbf{n}$  is normal to the shock surface. The vector  $\mathbf{t}$  is tangent to the shock surface and directed in the  $\xi_3$  direction. The vector  $\mathbf{s}$  is also tangent to the shock surface and orthogonal to vectors  $\mathbf{n}$  and  $\mathbf{t}$

It can be shown that these vectors can be written as

$$\begin{aligned}
\mathbf{s} &= \alpha_1(\alpha_4^2 + \alpha_5^2)\mathbf{i} + \alpha_5(\alpha_2\alpha_5 - \alpha_3\alpha_4)\mathbf{j} - \alpha_5(\alpha_2\alpha_5 - \alpha_3\alpha_4)\mathbf{k} \\
\mathbf{n} &= (\alpha_2\alpha_5 - \alpha_3\alpha_4)\mathbf{i} - \alpha_1\alpha_5\mathbf{j} + \alpha_1\alpha_4\mathbf{k} \\
\mathbf{t} &= \alpha_4\mathbf{i} + \alpha_5\mathbf{k}
\end{aligned} \tag{4.6}$$

Or

$$\begin{aligned}
 \mathbf{s} &= [s_x(\alpha_1, \alpha_4, \alpha_5)]\mathbf{i} + [s_y(\alpha_2, \alpha_3, \alpha_4, \alpha_5)]\mathbf{j} + [s_z(\alpha_2, \alpha_3, \alpha_4, \alpha_5)]\mathbf{k} \\
 \mathbf{n} &= [n_x(\alpha_2, \alpha_3, \alpha_4, \alpha_5)]\mathbf{i} + [n_y(\alpha_1, \alpha_5)]\mathbf{j} + [n_z(\alpha_1, \alpha_4)]\mathbf{k} \\
 \mathbf{t} &= [t_y(\alpha_4)]\mathbf{j} + [t_z(\alpha_5)]\mathbf{k}
 \end{aligned} \tag{4.7}$$

With such a definition of the shock-normal and shock-tangent vectors the velocity components normal and tangent to the shock surface can now be written as

$$\begin{aligned}
 V_s &= (u_s s_x + v_s s_y + w_s s_z) / |\mathbf{s}| \\
 V_n &= (u_s n_x + v_s n_y + w_s n_z) / |\mathbf{n}| \\
 V_t &= (u_s t_x + v_s t_y + w_s t_z) / |\mathbf{t}|
 \end{aligned} \tag{4.8}$$

where  $V_n$ ,  $V_t$  and  $V_s$  are the velocity components in the  $\mathbf{n}$ ,  $\mathbf{t}$  and  $\mathbf{s}$  directions, respectively. Similarly we can also define the freestream velocity components  $(V_n)_\infty$ ,  $(V_t)_\infty$  and  $(V_s)_\infty$ .

Having defined the relevant velocity components for the purpose of writing the five Rankine-Hugoniot shock-crossing equations (representing the conservation of mass, momentum and energy), we note that we have actually seven unknowns at the shock. These seven unknowns are written in a vectorial form as

$$\mathbf{q}_s = [\rho, \rho u, \rho v, \rho w, \rho T, p, \Delta]_s^T \tag{4.9}$$

Thus we need two more equations to close the system of equations at the shock. One of these additional equations is the equation of state of the gas and the other equation is provided by applying the differential continuity of mass equation behind the shock. As we see no approximation other than the assumption of a Rankine-Hugoniot shock has been made. These equations are equally valid whether the conditions behind the

shock are viscous or inviscid dominated or whether substantial flowfield gradients exist behind the shock.

The seven governing equations at the shock can now be written as

$$h + V^2/2 - (h_0)_{\infty} = 0 \quad (4.10a)$$

$$\rho V_n - \rho_{\infty} (V_n)_{\infty} = 0 \quad (4.10b)$$

$$\rho [V_t - (V_t)_{\infty}] = 0 \quad (4.10c)$$

$$\rho [V_s - (V_s)_{\infty}] = 0 \quad (4.10d)$$

$$p - p_{\infty} + \rho (V_n)^2 - \rho_{\infty} (V_n)_{\infty}^2 = 0 \quad (4.10e)$$

along with the equation of state written in the functional form

$$f(\rho, T, p, C_i) = 0 \quad (4.10f)$$

and the differential continuity equation written as

$$(\rho U_i / J)_{,xi} = 0 \quad (4.10g)$$

Equations (4.10a) to (4.10f) are quite straight forward; however, the differential continuity equation [Eq. (4.10g)] needs some further elaboration. Noting the definition of contravariant velocity components ( $U_i$ ), we can re-write this equation as

$$[a_{i,xj}(\rho u_j)]_{,xi} = 0 \quad (4.10g)$$

where

$$\begin{aligned}
a_{1x} &= (z_{,\xi_2} \alpha_4 - y_{,\xi_2} \alpha_5) \\
a_{1y} &= x_{,\xi_2} \alpha_5 \\
a_{1z} &= -x_{,\xi_2} \alpha_4 \\
a_{2x} &= (\alpha_2 \alpha_5 - \alpha_3 \alpha_4) \\
a_{2y} &= -\alpha_1 \alpha_5 \\
a_{2z} &= \alpha_1 \alpha_4 \\
a_{3x} &= (y_{,\xi_2} \alpha_3 - z_{,\xi_2} \alpha_2) \\
a_{3y} &= (z_{,\xi_2} \alpha_1 - x_{,\xi_2} \alpha_3) \\
a_{3z} &= (x_{,\xi_2} \alpha_2 - y_{,\xi_2} \alpha_1)
\end{aligned} \tag{4.11}$$

It should be noted that the dependance of all the quantities appearing in Eqs. (4.10a) to (4.10g) on the seven unknowns at the shock point ( $\mathbf{q}_s$ ) is now completely described. Thus we can write the seven equations [Eqs. (4.10a) thru (4.10g)] at the shock in the vectorial form

$$f_s^{n+1} = f_s(\mathbf{q}_s^{n+1}) = 0 \tag{4.12}$$

These equations can now be linearized around the previous iteration. Using central-differenced approximations for  $\xi_3$  derivatives and backward-differenced approximations for  $\xi_1$  and  $\xi_2$  derivatives, we can rewrite these equations in the form

$$\begin{aligned}
& (\mathbf{A}_s)_k^n \cdot (\Delta \mathbf{q}_s)_{k-1}^{n+1} + (\mathbf{B}_s)_k^n \cdot (\Delta \mathbf{q}_s)_k^{n+1} + (\mathbf{C}_s)_k^n \cdot (\Delta \mathbf{q}_s)_{k+1}^{n+1} \\
& + \begin{bmatrix} (\mathbf{D}_s)_k^n & 0 \\ 0 & 0 \end{bmatrix} \cdot \begin{bmatrix} \Delta \mathbf{q}_{k,LMAX-1}^{n+1} \\ 0 \end{bmatrix} = (\mathbf{g}_s^*)_k^n
\end{aligned} \tag{4.13}$$

Here it should be noted that  $A_s$ ,  $B_s$  and  $C_s$  are  $7 \times 7$  matrices,  $g_s$  is a vector of length 7 and  $D_s$  is a  $6 \times 6$  matrix. This equation represents the final set of equations to be solved at the shock point in conjunction with flowfield solution within the shock-layer.

## 4.2. Coupling of the Shock-Point Solution With the Inner Flowfield

As can be seen with from Eq. (4.13) the solution of the equations at the shock are coupled to the inner flowfield solution through  $\Delta q_{k,LMAX-1}^{n+1}$ . In order to finally solve this system of equations we note that Eq. (3.14) shows that the inner flowfield solution (from  $\ell = 1, 2, 3, \dots, LMAX-1$ ) is decoupled in the crossflow direction. Thus a forward substitution approach is used for all crossflow planes to develop the recursive relations

$$\Delta \chi_{k,\ell}^{n+1} = - R_{k,\ell} \cdot \Delta \chi_{k,\ell+1}^{n+1} + r_{k,\ell} \quad (4.14)$$

Now we note that based on our smoothing approach we can write to a second-order accuracy

$$\Delta q_{k,LMAX-1}^{n+1} \approx \Delta \chi_{k,LMAX-1}^{n+1} \quad (4.15a)$$

$$\Delta q_{k,LMAX}^{n+1} \approx \Delta \chi_{k,LMAX}^{n+1} \quad (4.15a)$$

The inner flowfield solution can now be related to the shock-point solution vector  $\Delta q_s^{n+1}$  through relations of the form

$$\Delta q_{k,LMAX-1}^{n+1} = - [R_{k,LMAX-1} \ 0] \cdot (\Delta q_s)_k^{n+1} + r_{k,LMAX-1} \quad (4.16)$$

After substituting Eq. (4.16) into Eq. (4.13), we can reduce Eq. (4.13) to the form

$$A_k^n \cdot (\Delta q_s)_{k-1}^{n+1} + B_k^n \cdot (\Delta q_s)_k^{n+1} + C_k^n \cdot (\Delta q_s)_{k+1}^{n+1} = g_k^n \quad (4.17)$$

Equation (4.17) is now solved using appropriate reflective and symmetric boundary conditions in the leeward and windward pitch planes of symmetry. This solution gives simultaneously the  $\Delta q_s^{n+1}$  vectors at each shock point ( $k = 1, 2, 3, \dots, KMAX$ ).

Using the shock point solution and the recursive relations of Eq. (4.14), we can obtain the intermediate solution vector  $\Delta \chi^{n+1}$  for all interior points. The final smoothed solution at these interior points is then determined from Eqs. (3.8a) and (3.8b). The x, y and z coordinates of the new shock point locations are now determined using Eq. (4.3) and the grid is updated for the next iteration. This overall iterative process is repeated until the solution converges at all grid points, and then the solution moves on to the next marching step.

## V. A SIMPLIFIED ANALYSIS FOR DEPARTURE

Unlike classical PNS treatments in the present approach the governing PNS equations are written in as a differential/algebraic system rather than a pure differential system. By a differential/algebraic system we mean a system of equations composed of several differential equations coupled together through an algebraic relation. In the present PNS formulation the differential equations governing the conservation of mass, momentum and energy are coupled together through the algebraic relation representing the equation of state. By studying a model differential/algebraic problem (see Appendix D) we have been able to show that unlike classical PNS treatments (Schiff and Steger, 1979; Shanks et al., 1979; Chaussee et al., 1981; and Vigneron et al., 1978) the present formulation is unconditionally time-like (Bhutta and Lewis, 1985c and 1985d). In order to further demonstrate this approach we also studied a simplified version of the governing PNS equations. The general outline and conclusions of this simplified eigenvalue analysis are briefly presented in the following discussion.

In order to simplify the required mathematics, let us restrict ourselves to

- (a) two-dimensional perfect-gas flows, and
- (b) an evenly spaced square grid such that  $\xi_{1,x} = \xi_{2,z} = 1$  and  $\xi_{1,z} = \xi_{2,x} = 0$

The simplification of a perfect gas is done with the understanding that even for the actual multi component reacting-gas case the fluid is still assumed to be a mixture of perfect gases. Consequently the basic numerical scheme has to be at least stable for a single-species perfect-gas model. Furthermore, we choose to approximate the equation of state for a perfect gas by

$$\gamma p - \rho T + \theta(p_{,\xi_1} + p_{,\xi_2}) = 0 \quad (5.1)$$

where the coefficient ' $\theta$ ' is chosen such that  $\theta \approx 0$ , and for all practical purposes

$$\theta p_{,\xi_1} + \theta p_{,\xi_2} + \gamma p - \rho T \approx \gamma p - \rho T$$

It should be noted that the use of this coefficient  $\theta$  is for the sole purpose of the following stability analysis, and not for the actual solution scheme. In other words, the actual solution corresponds to the use of  $\theta = 0$ . The reason for introducing this coefficient ' $\theta$ ' is that it makes the streamwise jacobian matrix nonsingular, so that one can perform certain matrix operations to simplify the stability analysis. Furthermore, there are no mathematical tools available to directly determine the character of differential/algebraic systems. The available mathematical tools are strictly for purely differential systems. Thus, by introducing the coefficient ' $\theta$ ' in Eq. (5.1) we are able to transform our differential/algebraic problem into a purely differential form, which can then be analyzed.

The choice of 'small enough  $\theta$ ' does not adversely affect the resulting conclusions. In other words we can take the limit  $\theta \rightarrow 0$ . This is indeed a heuristic approach, and the justification comes from the model differential/algebraic problem discussed in Appendix D. The use of ' $\theta$ ' in Eq. (5.1) corresponds to the use of the ' $\epsilon$ ' term in Formulation II

of the model problem. For this model problem it has been shown in Appendix D that the choice of  $\epsilon \rightarrow 0^+$  does not produce any singularity in the final solution. This fact has also been numerically demonstrated by the present authors in their earlier work (Bhutta and Lewis, 1985d).

With the equation of state given by Eq. (5.1), and after neglecting the viscous terms containing the contributions of  $w$  and  $w_{,\xi_2}$ , we can write the simplified PNS equations as

$$\begin{aligned} (\mathbf{A}_1^n \cdot \mathbf{d})_{,\xi_1} + (\mathbf{A}_2^n \cdot \mathbf{d})_{,\xi_2} - \epsilon [\mathbf{M}^n \cdot \mathbf{d}]_{,\xi_2} - \mathbf{A}_0^n \cdot \mathbf{d} \\ = - [\mathbf{f}_{1,\xi_1}^n + \mathbf{f}_{2,\xi_2}^n - \epsilon \mathbf{s}_{,\xi_2}^n - \mathbf{h}^n] \end{aligned} \quad (5.2)$$

where

$$\mathbf{d} = \Delta \mathbf{q}^{n+1} \quad (5.3)$$

and  $\mathbf{A}_1^n$ ,  $\mathbf{A}_2^n$  and  $\mathbf{M}^n$  are the jacobian matrices.

If we assume that  $\mathbf{A}_1^n$ ,  $\mathbf{A}_2^n$  and  $\mathbf{M}^n$  do not change with  $\xi_1$  and  $\xi_2$  (a frozen coefficient analysis), we can write

$$\mathbf{A}_1^f \cdot \mathbf{d}_{,\xi_1} + \mathbf{A}_2^f \cdot \mathbf{d}_{,\xi_2} - \mathbf{B}^f \cdot \mathbf{d}_{,\xi_2} + \mathbf{c} = 0 \quad (5.4)$$

Although the above equation is a significantly simplified version of the original PNS equations, it is still difficult to study directly. As a further simplification, we choose to separately look at the viscous and inviscid limits of Eq. (5.4). We also note that as a minimum criterion of streamwise stability (which in this case, and for the class of PNS schemes based on the Schiff-Steger formulation, implies a marching-like character of the

governing equations), the "simplified PNS equations" being studied have to be streamwise stable (i.e., marching-like in the streamwise direction) in the viscous as well as the inviscid limits. In the following sections we look into the streamwise stability (marching-like character) of the viscous and the inviscid limits of Eq. (5.4).

## 5.1. Inviscid Limit

The inviscid limit of Eq. (5.4) can be written as

$$\mathbf{d}_{,\xi_1} + [\mathbf{A}_1^{\Gamma^{-1}} \mathbf{A}_2^{\Gamma}] \cdot \mathbf{d}_{,\xi_2} + \mathbf{A}_1^{\Gamma^{-1}} \cdot \mathbf{c} = 0 \quad (5.5)$$

or

$$\mathbf{d}_{,\xi_1} + \mathbf{N}_1 \cdot \mathbf{d}_{,\xi_2} + \mathbf{c} = 0 \quad (5.6)$$

This equation is now in a form which can be easily studied. For Eq. (5.6) to be stable, the  $\xi_1$  direction should be a valid marching direction. In other words, Eq. (5.6) has to be hyperbolic/parabolic or marching-like always. This condition is satisfied if the eigenvalues of  $\mathbf{N}_1$  are all real. If for simplicity we assume that  $w \ll u$ , then an eigenvalue analysis gives the eigenvalues of  $\mathbf{N}_1$  as (Bhutta and Lewis, 1985d)

$$\lambda_i = (1, w/u, w/u, w/u, w/u) \quad (5.7)$$

Thus, we see that all the eigenvalues of  $\mathbf{N}_1$  are unconditionally real. That is to say, the simplified PNS equations being studied are unconditionally marching-like in the inviscid

limit and represent a stable marching scheme in the subsonic as well as the supersonic flow regions.

It is of interest to consider the case where (like conventional non-iterative PNS schemes) we do not uncouple the pressure terms. In such a case the form of  $A_1^{-1}$  is similar to the one studied by Schiff and Steger (1979). The only difference is that we have  $\rho T$  as the independent variable rather than 'e'. The  $A_1^{-1}$  matrix for such a case is nonsingular and, thus, can be inverted. However, the eigenvalues of  $N_1$  for such a case (where we do not uncouple the pressure) turn out to be complex in the subsonic flow regions, and the marching scheme becomes unstable (not marching-like; i.e., elliptic) unless methods such as the sublayer approximations of Schiff and Steger (1979) or Vigneron et al. (1978) are used.

## 5.2. Viscous Limit

In the viscous limit, Eq. (5.4) simplifies to

$$d_{,\xi_1} = [A_1^{-1} \bar{B}^c] \cdot d_{,\xi_2 \xi_2} + A_1^{-1} \cdot c \quad (5.8)$$

or

$$d_{,\xi_1} = N_2 \cdot d_{,\xi_2 \xi_2} + c \quad (5.9)$$

In this form, the stability analysis becomes much simpler. The criterion of a stable marching scheme requires that Eq. (5.9) should be parabolic. The parabolic character

depends upon the eigenvalues of  $N_2$ , which should be real. Furthermore, in order to have positive diffusion effects in the  $\xi$  direction, these eigenvalues should also be positive. Thus, for the viscous limiting case to be stable, the eigenvalues of  $N_2$  should be real and positive. An eigenvalue analysis of  $N_2$  shows that the eigenvalues are (Bhutta and Lewis, 1985d)

$$\sigma_i = (0, 0, \varepsilon\mu/Pr\rho u, 4\varepsilon\mu/3\rho u, \varepsilon\mu/\rho u) \quad (5.10)$$

Thus, the eigenvalues  $\sigma_i$  are always real; however, they are positive only if  $u > 0$ . That is to say, as long as no flow reversal occurs in the streamwise direction, the viscous limit of the simplified PNS equations is also unconditionally marching-like. Since flow reversal means axial separation, this streamwise stability requirement actually tells us that a "single-sweep" solution of these PNS equations can not be marched through regions of axial flow separation. Of course, this conclusion comes as no surprise and has been a well accepted fact in fluid mechanics for a long time. It may be of value to note that the viscous terms do not include any pressure terms and, thus, for the present scheme as well as the previous PNS schemes the viscous terms do not provide any speed-of-sound contribution to the eigenvalues of the viscous limit. The speed-of-sound contributions to these eigenvalues for the viscous limit can come only from the jacobian matrix corresponding to the streamwise convective terms. For the classical PNS schemes (Schiff and Steger, 1979; Shanks et al., 1979; Chaussee et al., 1981; and Vigneron et al., 1978), this speed-of-sound contribution is the one which causes the problem of negative eigenvalues in the subsonic sublayer region. For the present PNS scheme, although the speed of sound does appear in the streamwise jacobian matrix ( $A_f$ ), it does not contribute to the eigenvalues in the viscous limit.

## VI. RESULTS AND DISCUSSION

In order to test the accuracy and efficiency of the proposed three-dimensional PNS scheme, we studied the flow around a sphere-cone configuration at an angle of attack of 20 deg and at a Mach number of 10.6. This test case has been studied by Cleary (1969) in the NASA Ames hypersonic wind tunnel. The freestream conditions for this case are given in Table 1 and the vehicle geometry is shown in Fig. 3. This sphere-cone geometry consists of a 0.028 m nose radius with a 15 deg aftcone. The vehicle geometry is 17.5 nose radii long. In this study both perfect-gas and equilibrium-air gas models were used to model the gas chemistry.

Cases 1, 2 and 3 represent the three different computational grids used to predict the flowfield using a perfect-gas model. Case 1 uses 31 circumferential planes and 50 points between the body and the shock. Case 2 uses 25 circumferential planes and Case 3 uses 17 circumferential planes. For all of these three perfect-gas calculations (Case 1, 2 and 3) the grid generated was a simple noncylindrical grid based on equally spaced  $\xi_3$  grid at the wall and at the shock. These equally spaced body and shock points were joined using straight lines in the  $\xi_2$  direction. For all of these grids the  $\xi_2$  grid distribution was the same and the grid spacing near the wall was 0.001% of the local shock standoff dis-

tance. The purpose of using a noncylindrical grid was to demonstrate the general-curvilinear-coordinate formulation used in our 3-D PNS scheme.

Case 4 represents the corresponding solution using an equilibrium-air gas model. Like the Case 1 grid, Case 4 uses 31 circumferential planes and 50 points between the body and the shock. However, in this case we used a cylindrical coordinate system in which the  $\xi_3$  (crossflow) grid points were located using equal angular spacing. The grid distribution in the  $\xi_2$  direction was the same as the one used for the perfect-gas calculations (Cases 1, 2 and 3), and the  $\xi_2$  grid spacing at the wall was 0.001% of the local shock standoff distance.

The following sections summarize some of the important results of these studies and discuss the solution accuracy, efficiency and grid-refinement characteristics.

## 6.1. Perfect-Gas Calculations

The following sections discuss the results of the Case 1, Case 2 and Case 3 calculations using a perfect-gas model.

### 6.1.1. Predictions of Surface-Measurable Quantities

Figures 4 thru 9 show the axial and crossflow distributions of the surface-measurable quantities (such as wall pressures, skin-friction coefficient and wall heat-transfer rates) using a perfect-gas model and the fine crossflow grid (Case 1). The axial distribution

of wall pressures is shown in Fig. 4, while the corresponding crossflow distribution is shown in Fig. 5. These results show that the streamwise and crossflow distributions are very smooth. Furthermore, the windward surface has reached an almost self-similar behavior, while the lee side is still undergoing substantial changes. The corresponding axial and circumferential distributions of skin-friction coefficient are shown in Figs. 6 and 7, respectively.

The axial and crossflow distributions of wall heat-transfer rates are shown in Figs. 8 and 9. The corresponding experimental predictions of the wall heat-transfer rates are also shown in these figures. Figure 8 shows the axial distribution of wall heat-transfer rates, and shows that the numerical and experimental predictions are in excellent agreement along the  $\phi = 0$  and  $\phi = 90$  deg planes. The leeward distribution shows a sudden rise in the experimental heat-transfer rates along  $x/R_n = 6$ . This rise is because the experimental flow on the lee side became turbulent around this region. The windward side, however, remained laminar. This can also be seen from the crossflow distribution shown in Fig. 9. This figure shows that the numerical predictions are in excellent agreement with the experimental data up to  $\phi = 160$  deg. Beyond this point the experimental data are higher due to transitional flow conditions.

### 6.1.2. Shock-Shape Predictions

The bow shock shape predicted by the Case 1 calculations is shown in Figs. 10 and 11. Figure 10 shows the axial variation of the bow shock shape along  $\phi = 0, 90$  and  $180$  degs. The crossflow distribution of the bow shock shape at the body end is shown in Fig. 11. These figures show that even under such a large angle-of-attack condition the

bow shock shape predicted by the new fully implicit, crossflow-coupled shock-fitting scheme is very smooth and well behaved. This is despite the large variations in the shock standoff distances between the windward and leeward sides. This clearly reflects on the accuracy of the new implicit shock-fitting scheme.

### 6.1.3. Effects of Crossflow Grid Refinement

We also did some grid-refinement studies to evaluate the effects of crossflow grid refinement on the accuracy and stability of the solution scheme. Three different grids were used with 31, 25 and 17 crossflow planes, respectively. Figure 12 shows the effects of this crossflow grid refinement on the wall heat-transfer rates. This figure shows that while the windward side remains almost unaffected, the lee side is quite sensitive to the grid refinement. Interestingly the coarse 17 plane grid shows a monotonic decrease of wall heat-transfer rate from the windward to the leeward side. The 25 and 31 plane grids, however, show a minimum around the crossflow separated region, followed by a subsequent rise toward the leeward side. Furthermore, the 31 plane solution shows that the numerical predictions of the location and magnitude of the minimum wall heat-transfer rate, are in very good agreement with the corresponding experimental data

Figure 13 shows the crossflow distributions of the crossflow skin-friction coefficient. These results show that actually the coarse 17-plane solution does not even predict any crossflow separation, and this explains the corresponding monotonic decrease in the wall heat-transfer rate. The 25-plane and 31-plane results, however, clearly show a region of crossflow separation between  $\phi = 160$  deg to  $\phi = 180$  deg. The extent of the separated region predicted by these two fine grids is also in good agreement.

These crossflow grid refinement studies show that the grid-refinement capabilities of our 3-D PNS scheme are very good. Furthermore, the results bring forth an important point that in order to maintain acceptable solution accuracy it is essential to use adequate grid-refinement in the crossflow direction. Coarse grids may produce smooth results, but these results may not accurately represent various flowfield details; such as, crossflow separated regions, etc.

## 6.2. Equilibrium-Air Calculations

The current equilibrium-air calculations were done in order to demonstrate the equilibrium-air capability developed in this phase I effort. In terms of the gas chemistry effects, the test case chosen corresponds to relatively low shock-layer temperatures. Peak shock-layer temperatures in the afterbody region are of the order of 400-450 Kelvin. Under these conditions the gas in the shock layer behaves like a perfect gas, and the effects of chemical reactions are negligible. Thus, even if we use an equilibrium chemically-reacting air model, if correctly done, we should not find any significant differences from the corresponding perfect-gas results. Indeed the results of our equilibrium-air calculations confirm these observations. Since the current equilibrium-air calculations are for the purpose of demonstrating the capability, the equilibrium-air calculations were only done up to an axial location of  $10R_n$ .

Figures 14 thru 19 show the effects of the equilibrium-air gas model on the surface measurable quantities. These figures also show the corresponding results of the perfect-gas calculations (Case 1). Figures 14 and 15 show the axial and crossflow dis-

tributions of the wall pressures, while the axial and crossflow distributions of the skin-friction coefficient are shown in Figs. 16 and 17, respectively. As can be seen from these figures, there is negligible difference between the perfect-gas and equilibrium-air predictions for this case. The axial and crossflow distributions of the wall heat-transfer rates are shown in Figs. 18 and 19, respectively. Again, it can be seen that the perfect-gas and equilibrium-air predictions for this test case are almost the same. It should be noted that this close agreement between the perfect-gas and equilibrium-air calculations is because of the low shock-layer temperatures for this wind-tunnel test case. Under higher temperatures, more realistic of free-flight conditions, these differences may be larger.

Figures 20 and 21 show the axial and crossflow variations of the shock-standoff distances predicted by these perfect-gas and equilibrium-air calculations. These shock-standoff distances are the radial distances between the body and the shock. Again we see negligible differences between the perfect-gas and equilibrium-air calculations. Typically, when the shock-layer temperatures are higher, the equilibrium-air effects are larger and the equilibrium-air shock-standoff distances are smaller than the corresponding perfect-gas predictions.

The effects of the gas model on the crossflow separated region on the leeward side are shown in Figs. 22 and 25. Figure 22 shows the leeward separation bubble for the perfect-gas case, while the separation bubble for the equilibrium-air case is shown in Fig. 23. As can be seen the location of separation and the extent of the separated region predicted using the two gas models is in close agreement. The detailed pressure contours on the lee side for the perfect-gas calculations are shown in Fig. 24, while the corresponding equilibrium-air predictions are shown in Fig. 25. These pressure contours in Figs. 24 and 25 correspond to the same pressure values. Note the low pressure region

around the separation bubble on the leeward side. These figures show that the details of the crossflow separated region predicted by the two gas models are also in close agreement with each other. The perfect-gas calculations predict slightly higher pressures in the crossflow separated region; however, these differences are still very small in magnitude.

The general details of the crossflow solution are shown in Figs. 26 thru 28. Figure 26 shows the pressure contours, Fig. 27 shows the temperature contours and the density contours are shown in Fig. 28. The pressure contours show the rapid flow expansion as we move from the windward to the leeward side. The temperature and density contours show clearly the rapid thickening of the viscous layer in the crossflow separated region. Again, it can be seen that the flowfield character predicted by the two models is in close agreement.

### 6.3. Computing Times

The computing times for the various calculations done in this study are shown in Table 2. It should be noted that the computing times presented in this table are for an IBM 3090 machine with scalar LEVEL = 3 optimization. These results show that the overall computing times of our 3-D PNS scheme are very reasonable. Since the solution scheme involves an implicit inversion algorithm to be used in the crossflow direction, the computing times should increase more rapidly than the corresponding increase in the crossflow grid refinement. Even so, the increase is not that much. For example, compared to Case 3, Case 2 shows 4% increase in computing time per grid point. On the

other hand, Case 1 shows only a 14% increase in computing time per grid point. The equilibrium-air (Case 4) computing times show a 20-25% increase over the corresponding perfect-gas (Case 1) calculations. Although this increase is quite reasonable in view of the table-look-up procedure used for the equilibrium-air calculations, it is still slightly more than what we have typically observed in our earlier work (Bhutta et al., 1985a). Typically, we have observed that with our 3-D PNS scheme the equilibrium-air calculations only take 10-15% more time than the corresponding perfect-gas calculations. This increase in the current equilibrium-air computing times is primarily due to the fact that the current 3-D PNS code is of a research nature and has not been fully optimized.

## VII. CONCLUSIONS

In this Phase I study a new three-dimensional and fully-iterative PNS scheme has been developed to study three-dimensional hypersonic flows around axisymmetric ballistic configurations under large angle-of-attack conditions. The flow around a sphere-cone configuration, at a Mach number of 10.6 and an angle of attack of 20 deg, was predicted to study the accuracy and efficiency of this new three-dimensional PNS scheme under large-angle-of-attack conditions. Both perfect-gas and equilibrium-air gas models were used. The perfect-gas calculations were done using three different computational grids, while the equilibrium-air calculation was done using only a fine grid. These results substantiate the following conclusions:

- (1) A new three-dimensional perfect-gas/equilibrium-air PNS scheme has been developed. This scheme is an extension of the axisymmetric perfect-gas PNS scheme of Bhutta and Lewis (1985a). The basic axisymmetric PNS scheme and the present three-dimensional PNS scheme are inherently stable in the subsonic as well as the supersonic flow regions and do not require the use of any sublayer approximation. Furthermore, the schemes permits very fine grids to be used in the near-wall region for improving solution accuracy.

(2) The present PNS scheme uses a second-order accurate smoothing approach which is an extension of the earlier axisymmetric approach of Bhutta and Lewis (1985a,b). In this approach the crossflow smoothing effects are applied to all variables; however, the smoothing effects in the axis-normal direction are limited only to the pressure field. This results in accurate wall heat-transfer and skin-friction predictions even with coarse grids in the axis-normal direction.

(3) A new predictor-corrector solution scheme has been developed to treat the strong crossflow coupling effects in and around the crossflow separated regions. This predictor-corrector scheme involves the same amount of operations as an Approximate Factorization scheme, however, it retains a stronger coupling between the crossflow and body-normal directions.

(4) At the shock a new fully-implicit shock-prediction scheme has been developed and used. This scheme uses a general curvilinear coordinate system and predicts the correct shock location without having to make any approximation about the viscous or inviscid nature of the flow behind the shock. Furthermore this shock-fitting solution is fully coupled in the crossflow direction and results in smoother and more accurate shock-shapes, and has very good stability and convergence characteristics.

(5) It is shown that with a pseudo-unsteady algorithm, the present fully-iterative three-dimensional results can be obtained accurately and efficiently without any significant computing-time penalty. Furthermore, the enhanced solution accuracy permits much larger marching steps to be used and this substantially reduces the total computing times.

(6) Grid refinement studies with the 3-D PNS scheme show that the developed PNS scheme has very good grid-refinement characteristics. Crossflow grid-refinement results show that the present scheme responds favorably to such a refinement, resulting in substantially more accurate solutions. Furthermore, the results clearly indicate that sufficient crossflow refinement is essential to accurately capture various flowfield details which may have a significant impact on the wall heat-transfer and skin-friction predictions.

(7) A three-dimensional PNS scheme has been developed to accurately predict supersonic/hypersonic flowfields around ballistic configurations. The procedure is fast-convergent, very efficient and represents a substantial improvement over existing numerical capabilities for predicting such flows. Furthermore, the scheme is capable of treating various gas models in a unified manner. The scheme shows great promise for extension to study the supersonic/hypersonic flowfields around realistic three-dimensional ballistic configurations with fins and other control surfaces.

## APPENDIX A. DERIVATION OF 3-D PNS EQUATIONS

The general motion of viscous compressible fluids is described by the well known full Navier-Stokes (NS) equations (White, 1974). If we assume (a) Newtonian fluid behavior, (b) Stokes' Hypothesis, and (c) no body forces, we can write the three-dimensional NS equations as

$$(\rho u)_{,x} + (\rho v)_{,y} + (\rho w)_{,z} = 0 \quad (A.1)$$

$$(\rho u^2 + p)_{,x} + (\rho vu)_{,y} + (\rho wu)_{,z} = a_1 \quad (A.2)$$

$$(\rho uv)_{,x} + (\rho v^2 + p)_{,y} + (\rho wv)_{,z} = a_2 \quad (A.3)$$

$$(\rho uw)_{,x} + (\rho vw)_{,y} + (\rho w^2 + p)_{,z} = a_3 \quad (A.4)$$

$$(\rho u\Phi)_{,x} + (\rho v\Phi)_{,y} + (\rho w\Phi)_{,z} = a_4 \quad (A.5)$$

where

$$a_1 = [2\mu u_{,x} - (2\mu/3)\nabla \cdot \mathbf{V}]_{,x} + [\mu(u_{,y} + v_{,x})]_{,y} + [\mu(u_{,z} + w_{,x})]_{,z} \quad (A.6)$$

$$a_2 = [2\mu v_{,y} - (2\mu/3)\nabla \cdot \mathbf{V}]_{,y} + [\mu(v_{,x} + u_{,y})]_{,x} + [\mu(v_{,z} + w_{,y})]_{,z} \quad (A.7)$$

$$a_3 = [2\mu w_{,z} - (2\mu/3)\nabla \cdot \mathbf{V}]_{,z} + [\mu(w_{,x} + u_{,z})]_{,x} + [\mu(w_{,y} + v_{,z})]_{,y} \quad (A.8)$$

and

$$a_4 = \nabla \cdot (k \nabla T) + \nabla \cdot (v \cdot \tau) + a_5 \quad (A.9)$$

Here  $\tau$  is the stress tensor for a Newtonian fluid, and is defined as (White, 1974)

$$\tau_{ij} = \mu [u_{i,x_j} + u_{j,x_i} - (2/3)\delta_{ij}u_{k,x_k}] \quad (A.11)$$

where  $u_1 = u$ ,  $u_2 = v$ ,  $u_3 = w$ ,  $x_1 = x$ ,  $x_2 = y$  and  $x_3 = z$ .

Equation (A.1) corresponds to the conservation of mass, and Eqs. (A.2-A.4) correspond to the conservation of momentum in the x, y and z directions, respectively. Equation (A.5) corresponds to the conservation of energy, and these equations [Eqs. (A.1)-(A.5)] are closed through the use of equation-of-state for the gas mixture written in the functional form

$$f(\rho, T, p) = 0 \quad (A.12)$$

The form of ' $\Phi$ ', ' $a_5$ ' and the functional form of the equation of state depends upon the gas model being used. For a perfect gas model these quantities are defined as

$$\Phi = C_p T + 0.5V^2 \quad (A.13a)$$

$$a_5 = 0 \quad (A.14a)$$

$$f(\rho, T, p) = (y_p - \rho T) = 0 \quad (A.15a)$$

For an equilibrium-air gas model these quantities are defined as

$$\Phi = h(p, T) + 0.5V^2 \quad (A.13b)$$

$$a_5 = 0 \quad (A.14b)$$

$$f(\rho, T, p) = [\rho - \rho(p, T)] = 0 \quad (A.15b)$$

The above equations have been written in a nondimensional form, and the nondimensionalization scheme used is

$$\begin{aligned} u_i &= u_i^* / a_{\infty}^*; \quad \rho = \rho^* / \rho_{\infty}^*; \quad T = T^* / T_{\infty}^*; \quad p = p^* / (\rho_{\infty}^* a_{\infty}^{*2}); \\ \mu &= \mu^* / \mu_{\infty}^*; \quad k = k^* / k_{\infty}^*; \quad x_i = x_i^* / Rn^* \end{aligned} \quad (A.16)$$

Equations (A.1)-(A.5) and Eq. (A.12) can be combined together and written in the following vectorial form:

$$e_{1,x} + e_{2,y} + e_{3,z} = \epsilon(g_{1,x} + g_{2,y} + g_{3,z}) + p \quad (A.17)$$

Using indicial notation we can write Eq.(A.17) as

$$(e_j - \epsilon g_j)_{,x_j} = p \quad (A.18)$$

Or

$$k_{,x_j}^j = p \quad (A.19)$$

Now consider the general coordinate transformation

$$\xi_j = \xi_j(x_k) \quad (A.20)$$

where the orientation of our general curvilinear coordinate system is such that  $\xi_1$  is measured along the body,  $\xi_2$  is measured from the body to the outer bow shock, and  $\xi$

$_3$  is the crossflow direction. Thus, derivatives in the transformed space are related to the derivatives in the physical space by

$$( )_{,\xi_k} = x_{j,\xi_k} ( )_{,x_j} \quad (A.21)$$

If 'J' represents the determinant of the Transformation-Jacobian for Eq. (A.20); i.e.,

$$J = \text{Det}[(\xi_1, \xi_2, \xi_3)/(x_1, x_2, x_3)] \quad (A.22)$$

we can write Eq. (A.19) as

$$(1/J)(\xi_{j,x_k})(k_{k,\xi_j}) = (1/J)p \quad (A.23)$$

Equation (A.23) can be further expanded as

$$[(1/J)(\xi_{j,x_k})k_k]_{,\xi_j} - k_k[(1/J)(\xi_{j,x_k})]_{,\xi_j} = (1/J)p \quad (A.22)$$

Viviand (1974) has shown that the Jacobian satisfies the identity

$$J_{,\alpha} = J(\xi_{j,\alpha})_{,\xi_j} \quad (A.25)$$

where ' $\alpha$ ' is an arbitrary quantity. Equation (A.25) can be used to obtain

$$J_{,x_k} = J(\xi_{j,x_k})_{,\xi_j} \quad (A.26)$$

At the same time the chain rule of differentiation gives

$$J_{,x_k} = (\xi_{j,x_k})J_{,\xi_j} \quad (A.27)$$

Thus, we can see that by combining Eqs. (A.26) and (A.27) we can obtain yet another identity

$$(\xi_{j,x_k})_{,\xi_j} - (1/J)(\xi_{j,x_k})J_{,\xi_j} = 0 \quad (A.28)$$

The chain rule of differentiation also gives

$$[(1/J)\xi_{j,x_k}]_{,\xi_j} = (1/J)[(\xi_{j,x_k})_{,\xi_j} - (1/J)(\xi_{j,x_k})J_{,\xi_j}] \quad (A.29)$$

Thus, from Eqs. (A.28) and (A.29) we obtain

$$[(1/J)\xi_{j,x_k}]_{,\xi_j} = 0 \quad (A.30)$$

Substituting Eq. (A.30) in Eq. (A.24), we see that the NS equations in a general curvilinear coordinate system can be written as

$$[(1/J)\xi_{j,x_k}k_k]_{,\xi_j} = (1/J)p \quad (A.31)$$

If we use the notation

$$f_j = (1/J)\xi_{j,x_k}e_k \quad (A.32)$$

$$s_j = (1/J)\xi_{j,x_k}g_k \quad (A.33)$$

$$h = (1/J)p \quad (A.34)$$

we can write the NS equations in a general curvilinear coordinate system as

$$f_{i,t_j} = \varepsilon s_{i,t_j} + h \quad (A.35)$$

In order to parabolize Eq. (A.35) we neglect all streamwise diffusion effects. With this assumption, the three-dimensional parabolized Navier-Stokes (PNS) equations in a general curvilinear coordinate system become

$$f_{j,\xi_j} = \epsilon(s_{2,\xi_2} + s_{3,\xi_3}) + h \quad (A.36)$$

where

$$f_j = (1/J) \begin{bmatrix} \rho U_j \\ \rho u U_j + \xi_{j,x} p \\ \rho v U_j + \xi_{j,y} p \\ \rho w U_j + \xi_{j,z} p \\ \Phi \rho U_j \\ 0 \end{bmatrix} \quad (A.38)$$

$$s_n = (\mu/J) \begin{bmatrix} 0 \\ m_{nkk} u_{,\xi_n} + 0.5(m_{n1j} u_{j,\xi_n}) \\ m_{nkk} v_{,\xi_n} + 0.5(m_{n2j} u_{j,\xi_n}) \\ m_{nkk} w_{,\xi_n} + 0.5(m_{n3j} u_{j,\xi_n}) \\ \{m_{nkk} T_{,\xi_n} C_p / Pr + m_{nkk} u_j u_{j,\xi_n}\} \\ (1/3)m_{njk} u_j u_{k,\xi_n} \\ 0 \end{bmatrix} \quad (A.39)$$

where  $n = 2$  and  $n = 3$ , respectively, and

$$h = [0, 0, 0, 0, f - f(\rho, T, p)]^T \quad (A.40)$$

## APPENDIX B. EXPRESSIONS FOR THE JACOBIAN MATRICES

The three-dimensional parabolized Navier-Stokes (PNS) equations for a general gas flow in a general curvilinear coordinate system, at the  $j+1$  marching step and at the  $n+1$  iteration level, can be written in the following vectorial form:

$$\mathbf{f}_{j,\xi_j}^{j+1,n+1} = \varepsilon \mathbf{s}_{2,\xi_2}^{j+1,n+1} + \varepsilon \mathbf{s}_{3,\xi_3}^{j+1,n+1} + \mathbf{h}^{j+1,n+1} \quad (B.1)$$

Using a first-order Taylor series expansion around the previous iteration, we can write

$$\begin{aligned} \mathbf{f}_j^{j+1,n+1} &\simeq \mathbf{f}_j^{j+1,n} + \mathbf{A}_j^{j+1,n} \cdot \Delta \mathbf{q}^{n+1} \\ \mathbf{s}_2^{j+1,n+1} &\simeq \mathbf{s}_2^{j+1,n} + \mathbf{M}_2^{j+1,n} \cdot \Delta \mathbf{q}^{n+1} \\ \mathbf{s}_3^{j+1,n+1} &\simeq \mathbf{s}_3^{j+1,n} + \mathbf{M}_3^{j+1,n} \cdot \Delta \mathbf{q}^{n+1} \\ \mathbf{h}^{j+1,n+1} &\simeq \mathbf{h}^{j+1,n} + \mathbf{A}_0^{j+1,n} \cdot \Delta \mathbf{q}^{n+1} \end{aligned} \quad (B.2)$$

where

$$\Delta \mathbf{q}^{n+1} = \mathbf{q}^{j+1,n+1} - \mathbf{q}^{j+1,n} \quad (B.3)$$

The matrices  $\mathbf{A}_0$ ,  $\mathbf{A}_j$  and  $\mathbf{M}$  are called the jacobian matrices, and have the following form:

$$A_j = (1/J) \begin{bmatrix} 0 & \xi_{j,x} & \xi_{j,y} & \xi_{j,z} & 0 & 0 \\ -uU_j & \xi_{j,x}u + U_j & \xi_{j,y}u & \xi_{j,z}u & 0 & \xi_{j,x} \\ -vU_j & \xi_{j,x}v & \xi_{j,y}v + U_j & \xi_{j,z}v & 0 & \xi_{j,y} \\ -wU_j & \xi_{j,x}w & \xi_{j,y}w & \xi_{j,z}w + U_j & 0 & \xi_{j,z} \\ -\Phi U_j & \xi_{j,x}\Phi + uU_j & \xi_{j,y}\Phi + vU_j & \xi_{j,z}\Phi + wU_j & U_j & 0 \\ 0 & 0 & 0 & 0 & 0 & 0 \end{bmatrix} \quad (B.4)$$

$$M_n = (\mu/J) \begin{bmatrix} 0 & 0 & 0 & 0 & 0 & 0 \\ M_{n21} & M_{n22} & M_{n23} & M_{n24} & 0 & 0 \\ M_{n31} & M_{n32} & M_{n33} & M_{n34} & 0 & 0 \\ M_{n41} & M_{n42} & M_{n43} & M_{n44} & 0 & 0 \\ M_{n51} & M_{n52} & M_{n53} & M_{n54} & M_{n55} & 0 \\ 0 & 0 & 0 & 0 & 0 & 0 \end{bmatrix} \quad (B.7)$$

$$A_0 = \begin{bmatrix} 0 & 0 & 0 & 0 & 0 & 0 \\ 0 & 0 & 0 & 0 & 0 & 0 \\ 0 & 0 & 0 & 0 & 0 & 0 \\ 0 & 0 & 0 & 0 & 0 & 0 \\ 0 & 0 & 0 & 0 & 0 & 0 \\ f_{,\rho} & 0 & 0 & 0 & f_{,\rho T} & f_{,\rho} \end{bmatrix} \quad (B.8)$$

where the definition of  $\Phi$  depends upon the gas model used. For a perfect-gas model

$$\Phi = C_p T + 0.5 V^2 \quad (B.9a)$$

For an equilibrium-air gas model

$$\Phi = h(p, T) + 0.5V^2 \quad (B.9b)$$

The elements of the viscous jacobian matrices  $M_2$  and  $M_3$  are

$$M_{n21} = -m_{nkk}(u/\rho)_{,\xi_n} + (1/3)m_{n1j}(u_j/\rho)_{,\xi_n} \quad (B.10)$$

$$M_{n22} = (1/3)[(3m_{nkk} + m_{n11})(1/\rho)_{,\xi_n}] \quad (B.11)$$

$$M_{n23} = (1/3)m_{n12}(1/\rho)_{,\xi_n} \quad (B.12)$$

$$M_{n24} = (1/3)m_{n13}(1/\rho)_{,\xi_n} \quad (B.13)$$

$$M_{n31} = -m_{nkk}(v/\rho)_{,\xi_n} + (1/3)m_{n2j}(u_j/\rho)_{,\xi_n} \quad (B.14)$$

$$M_{n32} = (1/3)m_{n21}(1/\rho)_{,\xi_n} \quad (B.15)$$

$$M_{n33} = (1/3)[(3m_{nkk} + m_{n22})(1/\rho)_{,\xi_n}] \quad (B.16)$$

$$M_{n34} = (1/3)m_{n23}(1/\rho)_{,\xi_n} \quad (B.17)$$

$$M_{n41} = -m_{nkk}(w/\rho)_{,\xi_n} + (1/3)m_{n3j}(u_j/\rho)_{,\xi_n} \quad (B.18)$$

$$M_{n42} = (1/3)m_{n31}(1/\rho)_{,\xi_n} \quad (B.19)$$

$$M_{n43} = (1/3)m_{n32}(1/\rho)_{,\xi_n} \quad (B.20)$$

$$M_{n44} = (1/3)[(3m_{nkk} + m_{n33})(1/\rho)_{,\xi_n}] \quad (B.21)$$

$$M_{n51} = -(T/\rho)_{,\xi_n} C_p / Pr - m_{nkk}(V^2/\rho)_{,\xi_n} - 2m_{njk}u_j(u_k/\rho)_{,\xi_n}/3 \quad (B.22)$$

$$M_{n52} = m_{nkk}(u/\rho)_{,\xi_n} + m_{n1j}(u_j/\rho)_{,\xi_n}/3 \quad (B.23)$$

$$M_{n53} = m_{nkk}(v/\rho)_{,\xi_n} + m_{n2j}(u_j/\rho)_{,\xi_n}/3 \quad (B.24)$$

$$M_{n54} = m_{nkk}(w/\rho)_{,\xi_n} + m_{n3j}(u_j/\rho)_{,\xi_n}/3 \quad (B.25)$$

$$M_{n55} = m_{nkk}(1/\rho)_{,\xi_n} C_p / Pr \quad (B.26)$$

## APPENDIX C. SECOND-ORDER ACCURATE SMOOTHING TERMS

The governing three-dimensional PNS equations are elliptic in the  $\xi_2$  and  $\xi_3$  directions so that we use central-differenced approximations for all  $\xi_2$  and  $\xi_3$  derivatives. However, as was also noted by Schiff and Steger (1979), the use of central-differenced schemes is typically associated with solution oscillations. This oscillatory behavior becomes more pronounced if the local velocities are small, so that the diagonal terms of the jacobian matrices become relatively small also. In order to damp these solution oscillations, it is necessary to add some additional higher-order diffusion terms to the governing PNS equations.

The search for an appropriate form of the higher-order diffusion-like terms which would permit a simple yet a fully consistent and fully implicit treatment was very tedious and involved. The use of central-difference formulas for  $\xi_2$  and  $\xi_3$  derivatives makes the solution of the PNS equations second-order accurate, that is to say the leading truncation error is  $O(\Delta\xi_2^2, \Delta\xi_3^2)$ . Thus, if we were to add  $O(\Delta\xi_2^2)$  and  $O(\Delta\xi_3^2)$  diffusion-like terms to the right-hand side of governing equations, we would not affect the formal second-order accuracy of the difference scheme in the  $\xi_2$  and  $\xi_3$  directions. The governing equations can thus be written as

$$f_{j,\xi_j}^{j+1} = \varepsilon s_{2,\xi_2}^{j+1} + \varepsilon s_{3,\xi_3}^{j+1} + h^{j+1} + [\pi_1(q^{j+1})](\Delta\xi_2)^2 + [\pi_2(q^{j+1})](\Delta\xi_3)^2 \quad (C.1)$$

The proper choice of smoothing terms was actually based on a trial and error procedure. To start with, an explicit relation relating the smoothed ( $q$ ) and unsmoothed ( $\chi$ ) variables was chosen such that it included some second-order diffusion effects. A back-tracking approach was used to obtain the corresponding smoothing terms that needed to be added to the governing equations to produce the desired result. Once these smoothing terms in the governing equations were obtained, the order of each of these terms was analyzed and lower order terms were eliminated. Then, the governing equations with the modified smoothing terms were analyzed to see the impact of these changes on the final relationship between the smoothed and unsmoothed variables. After several iterations of this trial and error procedure, we were able to find a proper choice of these smoothing terms such that not only a second-order accuracy was retained, but a simple and explicit transformation between the unsmoothed and smoothed variables was also retained.

By choosing the form of the vector  $\pi$  to be

$$\pi_1(q) = \{(A_{1/\Delta\xi_1} - A_0) \cdot q, \xi_2 \xi_2 + [(A_2 - \varepsilon M_2) \cdot q, \xi_2 \xi_2], \xi_2 + [(A_3 - \varepsilon M_3) \cdot q, \xi_2 \xi_2], \xi_3\} \quad (C.2a)$$

$$\pi_2(q) = \{(A_{1/\Delta\xi_1} - A_0) \cdot q, \xi_3 \xi_3 + [(A_2 - \varepsilon M_2) \cdot q, \xi_3 \xi_3], \xi_2 + [(A_3 - \varepsilon M_3) \cdot q, \xi_3 \xi_3], \xi_3\} \quad (C.2b)$$

one can re-write Eq. (C.1) as

$$\begin{aligned} & [f_j + A_j \cdot (-q, \xi_2 \xi_2 \Delta \xi_2^2/4 - q, \xi_3 \xi_3 \Delta \xi_3^2/4)]_{\xi_j}^{j+1} \\ & = \varepsilon [s_2 + M_2 \cdot (-q, \xi_2 \xi_2 \Delta \xi_2^2/4 - q, \xi_3 \xi_3 \Delta \xi_3^2/4)]_{\xi_2}^{j+1} \\ & + \varepsilon [s_3 + M_3 \cdot (-q, \xi_2 \xi_2 \Delta \xi_2^2/4 - q, \xi_3 \xi_3 \Delta \xi_3^2/4)]_{\xi_3}^{j+1} \\ & + [h + A_0 \cdot (-q, \xi_2 \xi_2 \Delta \xi_2^2 - q, \xi_3 \xi_3 \Delta \xi_3^2/4)]_{\xi_0}^{j+1} + O(\Delta \xi_2^2, \Delta \xi_3^2) \end{aligned} \quad (C.3)$$

Now, let us define a new intermediate quantity  $\chi^{j+1}$  as

$$\chi^{j+1} = \mathbf{q}^{j+1} - \mathbf{q}_{,\xi_2\xi_2} \Delta\xi_2^2/4 - \mathbf{q}_{,\xi_3\xi_3} \Delta\xi_3^2/4 \quad (C.4)$$

So that

$$\chi^{j+1} - \mathbf{q}^{j+1} = -\mathbf{q}_{,\xi_2\xi_2} \Delta\xi_2^2/4 - \mathbf{q}_{,\xi_3\xi_3} \Delta\xi_3^2/4 = O(\Delta\xi_2^2, \Delta\xi_3^2) \quad (C.5)$$

and

$$(\chi^{j+1} - \mathbf{q}^{j+1})^2 = O(\Delta\xi_2^4, \Delta\xi_3^4, \Delta\xi_2^2\Delta\xi_3^2) \quad (C.6)$$

Using Eqs. (C.5) and (C.6) it can be shown that to second-order accuracy we can also write Eq. (C.4) as

$$\mathbf{q}^{j+1} = \chi^{j+1} + \mathbf{q}_{,\xi_2\xi_2} \Delta\xi_2^2/4 + \mathbf{q}_{,\xi_3\xi_3} \Delta\xi_3^2/4 \quad (C.7)$$

Now consider the Taylor series expansion of vector  $\mathbf{f}_j(\chi^{j+1})$  around  $\mathbf{q}^{j+1}$ , i.e.,

$$\begin{aligned} \mathbf{f}_j(\chi^{j+1}) &= \mathbf{f}_j(\mathbf{q}^{j+1}) + [\mathbf{f}_{j,q}]^{j+1} \cdot (\chi^{j+1} - \mathbf{q}^{j+1}) \\ &\quad + [\mathbf{f}_{j,qq}]^{j+1} \cdot (\chi^{j+1} - \mathbf{q}^{j+1})^2 + \dots \\ &\simeq \mathbf{f}_j(\mathbf{q}^{j+1}) + \mathbf{A}_j \cdot (-\mathbf{q}_{,\xi_2\xi_2} \Delta\xi_2^2/4 - \mathbf{q}_{,\xi_3\xi_3} \Delta\xi_3^2/4) \end{aligned} \quad (C.8)$$

Thus, to second-order accuracy we can write the above expression as

$$\mathbf{f}_j(\chi^{j+1}) \simeq \mathbf{f}_j(\mathbf{q}^{j+1}) + \mathbf{A}_j \cdot (-\mathbf{q}_{,\xi_2\xi_2} \Delta\xi_2^2/4 - \mathbf{q}_{,\xi_3\xi_3} \Delta\xi_3^2/4) \quad (C.9)$$

Similar expansions can be obtained for  $\mathbf{s}$  and  $\mathbf{h}$  so that to second-order accuracy in  $\Delta\xi_2$  we can rewrite Eq. (C.3) in terms of an intermediate solution  $\chi^{j+1}$  as

$$[\mathbf{f}_j(\chi^{j+1})]_{,\xi_1} = \varepsilon[\mathbf{s}_2(\chi^{j+1})]_{,\xi_2} + \varepsilon[\mathbf{s}_3(\chi^{j+1})]_{,\xi_3} + \mathbf{h}(\chi^{j+1}) + O(\Delta\xi_2^2) \quad (C.10)$$

The actual solution that we seek at the  $j+1$  step is related to this intermediate solution by Eq. (C.5). If we use  $\ell$  to denote the grid points in the  $\xi_2$  direction (i.e.,  $\ell = 1, 2, 3 \dots L_{MAX}$ ) and use  $k$  to denote the grid points in the  $\xi_3$  direction (i.e.,  $k = 1, 2, 3 \dots K_{MAX}$ ), we can further express  $q^{j+1}$  in terms of the intermediate solution  $\chi^{j+1}$  as

$$(\chi^*)_{k,\ell}^{j+1} = (\chi_{k+1,\ell}^{j+1})/4 + (\chi_{k,\ell}^{j+1})/2 + (\chi_{k-1,\ell}^{j+1})/4 \quad (C.11a)$$

$$q_{k,\ell}^{j+1} = (\chi^*)_{k,\ell+1}^{j+1}/4 + (\chi^*)_{k,\ell}^{j+1}/2 + (\chi^*)_{k,\ell-1}^{j+1}/4 \quad (C.11b)$$

Thus, we see that in order to introduce a second-order accurate fully implicit smoothing, we solve a block-tridiagonal system of equations [Eq. (C.10)] which is identical in form to the differenced form of the original PNS equations. However, this solution is just an intermediate solution ( $\chi^{j+1}$ ), and the final smoothed solution ( $q^{j+1}$ ) can be explicitly obtained by using Eq. (C.11). It should be noted that computationally this procedure is no more involved than the original (unsmoothed) differenced form of the PNS equations. Furthermore, another important feature of the present second-order smoothing is that the additional diffusion terms are proportional to  $\Delta\xi_2^2$  and  $\Delta\xi_3^2$ , so that the magnitude of the aforementioned smoothing automatically decreases with a decreasing  $\xi_2$  and  $\xi_3$  grid size, while still successfully damping out the numerical solution oscillations. Also, despite its final simple form, the present smoothing approach is more accurate and performs considerably better than the conventional smoothing approaches of Schiff and Steger (1979) and Shanks et al. (1979).

## APPENDIX D. A MODEL DIFFERENTIAL/ALGEBRAIC MARCHING PROBLEM

The system of equations represented by the governing PNS equations is not a pure differential system, it consists of five partial differential equations coupled through a sixth equation which is a purely algebraic relation. In the present treatment this set of governing equations is referred to as a 'differential/algebraic system'. The most important view point to be presented in this section is that the character classification of a differential/algebraic system is significantly different from the classical character classification of purely differential systems. In other words a purely differential system has a certain character; i.e., it is either elliptic or time-like or mixed. By 'time-like' we mean that a differential system is either hyperbolic or parabolic or mixed hyperbolic-parabolic. However, as long as the differential system is time-like, the numerical solution can be marched in the time-like direction. On the other hand, if the differential system is elliptic in character, marching-like numerical solutions are invalid.

The case of the differential/algebraic systems is, however, quite different. For such differential/algebraic systems the overall character of the system may depend upon the way in which the problem is formulated. That is to say, it may be possible to have a differential/algebraic system as elliptic or conditionally elliptic if one formulates the problem in one way, and have it unconditionally marching-like if one formulates the problem in another way. This idea is new and has given rise to a fair amount of controversy. Nonetheless, it may be analytically demonstrated on a model mixed-type system.

Consider the following system involving 3 unknowns,  $\phi_1$ ,  $\phi_2$  and  $\phi_3$ ; i.e.,

$$\begin{aligned}\phi_{1,x} - \phi_{2,y} &= 0 \\ \phi_{2,x} - \phi_{1,y} + 2\phi_{2,y} + \phi_{3,y} &= 0 \\ a^2\phi_1 - \phi_3 &= 0\end{aligned}\tag{D.1}$$

with initial condition specified at  $x = 0$  and boundary conditions specified at  $y=0$  and at  $y=1$ . Suppose we consider the following initial and boundary conditions:

$$\begin{aligned}\phi_3(0,y) &= a^2\phi_1(0,y) \\ \phi_1(0,y) &= \phi_2(0,y) = y\end{aligned}\tag{D.2}$$

$$\begin{aligned}\phi_3(x,0) &= a^2\phi_1(x,0) \\ \phi_{1,y}(x,0) &= \phi_{2,y}(x,0) = 1\end{aligned}\tag{D.3}$$

and

$$\begin{aligned}\phi_3(x,1) &= a^2\phi_1(x,1) \\ \phi_1(x,1) &= 1 + x \\ \phi_2(x,1) &= 1 - (a^2 + 1)x\end{aligned}\tag{D.4}$$

The solution to Eqs. (D.1) for these boundary conditions [Eqs. (D.2), (D.3) and (D.4)] is (Bhutta and Lewis, 1985d)

$$\begin{aligned}\phi_1(x,y) &= y + x \\ \phi_2(x,y) &= y - (a^2 + 1)x \\ \phi_3(x,y) &= a^2(y + x)\end{aligned}\tag{D.5}$$

The above model problem resembles the inviscid limit of the governing PNS equations. The model problem involves only first-order derivatives in the two spatial

coordinate directions to simulate the convective derivatives of the inviscid limit of the PNS equations. The third equation of this model problem is an algebraic relation, and is used to simulate the role of the algebraic equation of state in the PNS equations. Just like the equation of state in the governing PNS equations, the algebraic relation of the model problem appears not only as a relation to be satisfied within the solution domain, but it also appears in the initial conditions and the boundary conditions. The variable  $\phi_3$  of the model problem plays a similar role as played by pressure in the governing PNS equations. Now consider the following two different formulations of the model problem.

### D.1. Formulation I

In this approach we can substitute the third equation of Eq. (D.1) into the second equation and obtain

$$\begin{aligned}\phi_{1,x} - \phi_{2,y} &= 0 \\ \phi_{2,x} + (a^2 - 1)\phi_{1,y} + 2\phi_{2,y} &= 0\end{aligned}\tag{D.6}$$

Or we may simply write

$$\Psi_x + \mathbf{A} \cdot \Psi_y = 0\tag{D.7}$$

where

$$\Psi = [\phi_1, \phi_2]^T\tag{D.8}$$

and the eigenvalues of  $\mathbf{A}$  are

$$\begin{aligned}\lambda_1 &= 1 + (2 - a^2)^{0.5} \\ \lambda_2 &= 1 - (2 - a^2)^{0.5}\end{aligned}\quad (D.9)$$

It is shown by Bhutta and Lewis (1985d) that we can write Eq. (D.7) as

$$\begin{aligned}\psi_{1,x} + \lambda_1 \psi_{1,y} &= 0 \\ \psi_{2,x} + \lambda_2 \psi_{2,y} &= 0\end{aligned}\quad (D.10)$$

where

$$\begin{aligned}\phi_1 &= \psi_1 + \psi_2 \\ \phi_2 &= -\lambda_1 \psi_1 - \lambda_2 \psi_2\end{aligned}\quad (D.11)$$

Thus, we see that Eqs. (D.10), and equivalently Eqs. (D.6), are time-like if  $\lambda_1$  and  $\lambda_2$  are real ( $a^2 \leq 2$ ). When  $\lambda_1$  and  $\lambda_2$  are not real ( $a^2 > 2$ ), Eqs. (D.6) and (D.10) are elliptic in nature. In other words, a marching-like solution of Eqs. (D.6) will be valid only if  $a^2 \leq 2$ . Furthermore, it has been shown by Bhutta and Lewis (1985d) that for  $a^2 \leq 2$  the analytic solution to Eqs. (D.6) can be found, and it is the same as given by Eqs. (D.5).

## D.2. Formulation II

From the earlier discussion on Formulation I of the model problem, we see that the variable 'a' of the model problem is like the speed of sound in the governing PNS equations. That is to say, in the classical PNS schemes where the speed of sound appears in the eigenvalues through the pressure terms and the accompanying equation of state (Schiff and Steger, 1979, and Shanks et al., 1979), in the model problem the vari-

able 'a' appears in the eigenvalues through the variable  $\phi_3$ , and the corresponding algebraic relation. Now, for this model problem, if we can devise another formulation such that the variable 'a' no longer contributes to the eigenvalues of the system, it may provide us with a key to attempt a similar treatment of the governing PNS equations. Such a re-formulation of the model problem is mathematically possible, and it will be called Formulation II.

In Formulation I, the overall differential/algebraic system was reduced to a pure differential system. In Formulation II we attempt to solve directly the actual differential/algebraic system [Eq. (D.1)], and look at the character of the resulting system. At first glance it does not seem likely to be able to do that. However, it is possible to do such an analysis if one looks at Eq. (D.1) as the limiting case of a small-perturbation problem. Such an approach is valid as long as the small-perturbation problem being considered allows us to take this limit without any singular behavior.

For this purpose, consider the following problem (where  $\epsilon \geq 0$ )

$$\begin{aligned}\phi_{1,x} - \phi_{2,y} &= 0 \\ \phi_{2,x} - \phi_{1,y} + 2\phi_{2,y} + \phi_{3,y} &= 0 \\ \epsilon\phi_{3,x} - a^2\phi_1 - \phi_3 &= 0\end{aligned}\tag{D.12}$$

with

$$\begin{aligned}\phi_1(0,y) &= y \\ \phi_2(0,y) &= y \\ \phi_3(0,y) &= a^2y\end{aligned}\tag{D.13}$$

$$\begin{aligned}
 \phi_{1,y}(x,0) &= 1 \\
 \phi_{2,y}(x,0) &= 1 \\
 \varepsilon\phi_{3,x}(x,0) &= a^2\phi_1(x,0) - \phi_3(x,0)
 \end{aligned} \tag{D.14}$$

and

$$\begin{aligned}
 \phi_1(x,1) &= 1 + x \\
 \phi_2(x,1) &= 1 - (a^2 + 1)x \\
 \varepsilon\phi_{3,x}(x,1) &= a^2\phi_1(x,1) - \phi_3(x,1)
 \end{aligned} \tag{D.15}$$

Thus, the small perturbation problem being presented has the correct initial conditions, and the boundary conditions at  $y=0$  and  $y=1$  are consistent with the governing equations [Eqs. (D.12)].

The complete solution of this problem is given by Bhutta and Lewis (1985d). However, briefly speaking, Eqs. (D.12) can be written as

$$\mathbf{q}_x + \mathbf{A} \cdot \mathbf{q}_y - (1/\varepsilon)\mathbf{B} \cdot \mathbf{q} = 0 \tag{D.16}$$

The eigenvalues of  $\mathbf{A}$  are

$$\begin{aligned}
 \lambda_1 &= 1 + \sqrt{2} \\
 \lambda_2 &= 1 - \sqrt{2} \\
 \lambda_3 &= 0
 \end{aligned} \tag{D.17}$$

It is shown by Bhutta and Lewis (1985d) that we can write Eqs. (D.16) as

$$\begin{aligned}
 \psi_{1,x} + \lambda_1 \psi_{1,y} - \lambda_2 (f/\varepsilon) &= 0 \\
 \psi_{2,x} + \lambda_2 \psi_{2,y} + \lambda_1 (f/\varepsilon) &= 0 \\
 \psi_{3,x} - (\lambda_1 - \lambda_2) (f/\varepsilon) &= 0
 \end{aligned} \tag{D.18}$$

where

$$f = [a^2(\psi_1 + \psi_2) + (a^2 - 1)\psi_3]/(\lambda_1 - \lambda_2) \tag{D.19}$$

and

$$\begin{aligned}
 \phi_1 &= \psi_1 + \psi_2 + \psi_3 \\
 \phi_2 &= -\lambda_1 \psi_1 - \lambda_2 \psi_2 \\
 \phi_3 &= \psi_3
 \end{aligned} \tag{D.20}$$

Since  $\lambda_1$  and  $\lambda_2$  are real [see Eqs. (D.17)], we can see that Eqs. (D.18) are unconditionally time-like, and a marching-type numerical solution of Eqs. (D.18) will be unconditionally valid.

In order to answer the question, "How does the small perturbation problem of Eqs. (D.12) relate to the original problem of Eqs. (D.1)?", we can see that under the limiting condition

$$\varepsilon \rightarrow 0^+ \tag{D.21}$$

Eqs. (D.12) reduce to Eqs. (D.1), and the boundary conditions given by Eqs. (D.14) and (D.15) reduce to the actual boundary conditions given by Eqs. (D.3) and (D.4). The initial conditions are the same anyway.

A question arises --- "Is it valid to take the limit of Eqs. (D.18)?", or in other words "Does Eqs. (D.18) behave singularly because of the  $1/\epsilon$  factor?" To answer to this question, the third equation of this system [Eqs. (D.18)] shows that for all  $\epsilon$

$$f/\epsilon = \psi_{3,x}/(\lambda_1 - \lambda_2) \quad (D.22)$$

In other words, Eq. (D.22) indicates that ' $f/\epsilon$ ' is always defined, if  $\psi_{3,x}$  is defined for  $\epsilon \geq 0$ .

The demonstration that  $\psi_{3,x}$  is bounded for  $\epsilon \geq 0$  [i.e., Eqs. (D.18) is not singular when  $\epsilon \rightarrow 0^+$ ], comes from the actual analytic solution of Eqs. (D.18). It is shown by Bhutta and Lewis (1985d) that the analytic solution to Eqs. (D.18) and (D.20) is

$$\begin{aligned} \phi_1(x,y) &= y + x \\ \phi_2(x,y) &= y - (a^2 + 1)x \\ \phi_3(x,y) &= a^2(y + x) - a^2\epsilon[1 - \exp(-x/\epsilon)] \end{aligned} \quad (D.23)$$

where

$$\epsilon \geq 0 \quad (D.24)$$

It should be noted that we are marching in the  $x$  direction, so that our  $x$  is always positive and increasing. Thus, we see that with  $\epsilon \rightarrow 0^+$ , Eqs. (D.22) does not appear to be singular [or, equivalently Eqs. (D.22) does not appear to be singular] and, furthermore, this solution seems to be valid even for  $\epsilon = 0$  (Bhutta and Lewis, 1985d). Also, we see that with  $\epsilon \rightarrow 0^+$ , the solution to our hypothetical small perturbation problem appears to correctly approach the solution to our actual model problem; i.e.,

$$\begin{aligned}
 \phi_1(x,y) &= y + x \\
 \phi_2(x,y) &= y - (a^2 + 1)x \\
 \phi_3(x,y) &\rightarrow a^2(y + x)
 \end{aligned} \tag{D.25}$$

The aforementioned mathematical exercise is only used to present the conclusion --- There exist a class of 'differential/algebraic' system-of-equations where it is possible to have a conditionally time-like behavior if one formulates the problem in one way, and it is also possible to have the same problem as unconditionally time-like if one formulates the problem in a slightly different manner.

The model problem [Eqs. (D.1)] presented herein, bears considerable similarity to the inviscid limit of the governing PNS equations. The classical treatments of these PNS equations (Schiff and Steger, 1979; Vigneron et al., 1978; Shanks et al., 1979; etc.) correspond to the Formulation I presented earlier, which was conditionally time-like. The present scheme, however, follows the approach of Formulation II, which had an unconditionally time-like character.

### D.3. Numerical Solution of the Model Problem

The key point to be understood before attempting a solution of the model problem is that this model problem does not have an asymptotic limit; i.e., the solution grows as one marches on. Also, for this problem the equations governing the propagation of errors are the same as the governing equations. Consequently, the errors also convect and grow as the solution marches away from the initial conditions. This in itself is not a big

problem because if the problem were only limited to this, the solution and associated errors grow at comparable rates and the relative error (which is actually the important quantity) does not change much. However, the problem with truncation errors is that these errors not only convect and grow (as dictated by the governing equations), but at each step the cause for the generation of numerical errors remains there and keeps on adding to the existing errors. Thus, the net effect of this is that the growth of truncation errors is faster than the actual growth of the solution itself, and if one does not control these errors they can (and will) become large enough to start affecting the solution.

It is important to note that the solution in the y-coordinate direction is not only the initial source of truncation errors, but also the subsequent reason for their increased rate of growth (because at each step it adds to the existing error). Thus, it should be clear that the growth of these truncation errors is actually governed by the number of times the y-solution (and associated truncation errors) are committed. In other words, the errors will grow more rapidly if one takes smaller steps and, thus, commits a larger number of times the y-solution and the associated errors. This could be wrongfully interpreted as a step-size (departure) problem, but the fact remains that the step-size has nothing to do with the actual cause of the problem which is simply the inaccuracies in doing the numerical solution.

A clear advantage of an analytic solution of the problem (if possible) is that it does not suffer from solution inaccuracies and presents the true picture. Furthermore, when using numerical solutions to either validate or contradict analytic analysis, it is essential that either the numerical truncation errors be eliminated or controlled before one can focus on anything else as the potential source of any problems with the numerical solution.

In the following sections we will consider two different approaches to the numerical solution of Eqs. (D.1). The first approach will use an explicit Lax method (Anderson et al., 1984), and will focus on controlling the growth of errors at a marching step. In the second approach we will use an implicit bidiagonal scheme and will focus on the elimination of truncation errors. Thus, by controlling/eliminating the truncation errors, we will obtain numerical solutions which will truly reflect the character of the governing equations and not the effects of numerical inaccuracies.

The explicit Lax method has been used for the  $\varepsilon = 0$  case only, while the bidiagonal implicit method has been used for zero and nonzero values of  $\varepsilon$ . The main thrust of our numerical study is the bidiagonal implicit scheme because it is the most accurate. On the other hand, the explicit Lax method (although less accurate) is also interesting because the solution procedure is identical to the one used for a classical two-dimensional wave propagation problem, and the stability constraint obtained is comparable to the classical CFL condition.

### D.3.1. Explicit Lax Method

This approach is modeled after the Lax method for solving a linear first-order hyperbolic set of equations (Anderson et al., 1984, pp. 78). In this method the x-derivatives are forward differenced, so that the y-derivatives become explicitly known from the previous marching step. At the same time the solution values at the previous marching step are averaged, which is an  $O(\Delta y^2)$  approximation. The idea for this approach is that by avoiding the implicit solution in the y-direction we substantially reduce and limit the generation of numerical truncation errors. Furthermore, in this case an

eigenvalue analysis can be performed on the error-propagation equations to obtain a constraint condition which theoretically limits the growth of errors. Since numerically at each step we still cause a truncation error (however small), the actual errors still grow in magnitude, but this growth is extremely small if we maintain the stability constraint.

The important thing to note about this method is that for a given step size in the y-direction ( $\Delta y$ ), there is only an upper bound on the marching step size ( $\Delta x$ ) and not a lower bound which would have implied the classical departure-like behavior. As for the upper bound on the marching step-size, a similar analysis of the wave equations also gives an upper bound, which is the classical CFL condition (Anderson et al., 1984, pp. 78). Thus, this upper bound on the marching step-size is consistent with the classical treatments of true marching problems.

If we denote the x-direction by the superscript 'i' and the y-direction by the superscript 'j', the Eqs. (D.1) take the form

$$\begin{bmatrix} 1 & 0 & 0 \\ 0 & 1 & 0 \\ -a^2 & 0 & 1 \end{bmatrix} \begin{bmatrix} \phi_1 \\ \phi_2 \\ \phi_3 \end{bmatrix}^{i+1,j} = (1/2) \left( \begin{bmatrix} \phi_1 \\ \phi_2 \\ 0 \end{bmatrix}^{i,j+1} + \begin{bmatrix} \phi_1 \\ \phi_2 \\ 0 \end{bmatrix}^{i,j-1} \right) - \Delta x \begin{bmatrix} 0 & -1 & 0 \\ -1 & 2 & 1 \\ 0 & 0 & 0 \end{bmatrix} \begin{bmatrix} \phi_1 \\ \phi_2 \\ \phi_3 \end{bmatrix}_{,y}^{i,j} \quad (D.26)$$

where we have used forward-differenced approximations for the x-derivatives and an averaging of the solution at the previous (i-th) marching step. Furthermore, we make use of the fact that the solution at the previous (i-th) marching step is correctly known

and satisfies the following algebraic relations (which come from the governing equations applied at the  $i$ -th step):

$$\begin{aligned}\phi_3^{i,j+1} &= a^2 \phi_1^{i,j+1} \\ \phi_3^{i,j-1} &= a^2 \phi_1^{i,j-1}\end{aligned}\quad (D.27)$$

Thus, the Eqs. (D.26) reduce to simply the following

$$\begin{aligned}\begin{bmatrix} \phi_1 \\ \phi_2 \end{bmatrix}^{i+1,j} &= (1/2) \left( \begin{bmatrix} \phi_1 \\ \phi_2 \end{bmatrix}^{i,j+1} + \begin{bmatrix} \phi_1 \\ \phi_2 \end{bmatrix}^{i,j-1} \right) \\ &\quad - (k/2) \begin{bmatrix} 0 & -1 \\ (a^2 - 1) & 2 \end{bmatrix} \left( \begin{bmatrix} \phi_1 \\ \phi_2 \end{bmatrix}^{i,j+1} - \begin{bmatrix} \phi_1 \\ \phi_2 \end{bmatrix}^{i,j-1} \right)\end{aligned}\quad (D.28)$$

and

$$\phi_3^{i+1,j} = a^2 \phi_1^{i+1,j} \quad (D.29)$$

where  $k = (\Delta x / \Delta y)$ . The numerical solution of the above system is simple as all the quantities on the right-hand side of Eqs. (D.28) are known from the previous step and the values of  $\phi_1^{i+1,j}$  and  $\phi_2^{i+1,j}$  can then be explicitly obtained. Once  $\phi_1^{i+1,j}$  is known, the value of  $\phi_3^{i+1,j}$  is obtained from Eq. (D.29).

Suppose we denote the errors in  $\phi_1$  and  $\phi_2$  by  $E_1$  and  $E_2$ , respectively. An error analysis of Eqs. (D.28) can be performed if we assume these errors to be of the form

$$\begin{aligned}E_1^{i+1} &= e_1^{i+1} \exp[-iky] \\ E_2^{i+1} &= e_2^{i+1} \exp[-iky]\end{aligned}\quad (D.30)$$

and look at the amplification of the amplitudes of these errors (i.e.,  $e_1$  and  $e_2$ ) as we march in the  $x$  direction (Anderson et al., 1984, pp. 78). A Fourier analysis of the error equations can now be performed and shows that error amplitudes will not grow if

$$|k^2(c^2 + d^2) + dk| < 1 \quad (D.31)$$

where

$$(c + id) = 1 + (2 - a^2)^{0.5} \quad (D.32)$$

Further simplification shows that the constraint of Eq. (D.31) reduces to the following constraint on  $k = \Delta x / \Delta y$ ; i.e.,

$$|k - k_0| < [k_0^2 + 1/(c^2 + d^2)]^{0.5} \quad (D.33)$$

where

$$k_0 = -d/[2(c^2 + d^2)] \quad (D.34)$$

This constraint condition gives an upper bound on the choice of 'k' ( $k_{\max}$ ) or, equivalently, an upper bound on  $\Delta x$  for a given choice of  $\Delta y$ .

Figures D.1 to D.3 show the results obtained with the aforementioned explicit algorithm. These results are for a choice of  $a^2 = 10$  which corresponds to  $k_{\max} = 0.2$ . Two cases have been considered. Case 1 uses  $\Delta y = 0.1$  and  $\Delta x = 0.001$  ( $k = 0.01$ ), and Case 2 is for a choice of  $\Delta y = 0.05$  and  $\Delta x = 0.001$  ( $k = 0.02$ ). In other words, Case 1 uses 11 grid points in the  $y$  direction and 5000 marching steps in the  $x$  direction, while Case 2 uses 21 grid points in the  $y$  direction and 5000 marching steps in the  $x$  direction. Figures D.1, D.2 and D.3 show the  $\phi_1$ ,  $\phi_2$  and  $\phi_3$  solution at  $y = 0$ , respectively. For both cases the

solution was carried out until  $x = 5.0$ , at which location the maximum error in both solutions was of the order of  $10^{-29}$ . For these cases the truncation errors at the first marching station were of the order of  $10^{-31}$ - $10^{-32}$ . Figure D.4 shows the effect of violating the stability constraint (for this case) of  $k_{\max} = 0.2$ . It shows solutions for  $\Delta y = 0.1$  and for  $\Delta x$  values of 0.001, 0.005, 0.01, 0.02 and 0.1 (11 grid points in the  $y$  direction and 5000, 1000, 500, 250 and 50 steps, respectively, in the  $x$  direction). These values correspond to  $k$  values of 0.01, 0.05, 0.1, 0.2 and 1.0, respectively. It can be seen that for large values of  $k$  ( $> 0.2$ ) the maximum errors start to increase quite rapidly.

### D.3.2. Bidiagonal Implicit Method

The idea behind this approach is to eliminate the numerical truncation errors resulting from the floating-point roundoff (especially during the division operations). Multiplication by whole numbers and addition/subtraction operations do not contribute to the roundoff errors as much as the division operation by numbers with decimal fraction parts. Thus, the most desirable case would be to either have no division operations or at worst have division by whole numbers such as 2, 4, 5, etc. (because division operations for such numbers can be done exactly for almost all cases). One way of achieving this would be to (if possible) do as much of the algebra by hand as possible (such as matrix inversions, multiplications, etc.) and adjust the various solution parameters such as to have either no divisions or divisions by numbers such as 2, 4, 5, etc. Fortunately, in the case of this model problem this is possible to do. In order to do so in the following discussion we will focus on the case of  $a^2 = 3$  and for  $k = \Delta x / \Delta y = 0.5$ . The choice of these variables is solely based on the algebra simplification they introduce, and this makes the following analysis simple.

For the purely differential problem of Eqs. (D.12), we note that if we use one-sided (forward) difference operators for the  $y$ -derivatives, the solution at a given marching step can be integrated downwards from the specified boundary conditions at the  $y=1$  boundary toward the  $y=0$  boundary, where the solution can be obtained using the implicit boundary conditions of Eqs. (D.14). This method would in general be  $O(\Delta y)$  accurate; however, it will be exact for solutions having a linear behavior in  $y$ -direction. With such forward-difference approximations for the  $y$ -derivatives and backward-difference approximations for the  $x$ -derivatives, Eqs. (D.12) take the following form (for  $a^2 = 3$  and  $\Delta x = 0.5\Delta y$ ):

$$\begin{bmatrix} 2 & 1 & 0 \\ 1 & 0 & 1 \\ -3 & -1 & (1+\alpha) \end{bmatrix} \begin{bmatrix} \phi_1 \\ \phi_2 \\ \phi_3 \end{bmatrix}^{i+1,j} = \begin{bmatrix} 0 & 1 & 0 \\ 1 & -2 & -1 \\ 0 & 0 & 0 \end{bmatrix} \begin{bmatrix} \phi_1 \\ \phi_2 \\ \phi_3 \end{bmatrix}^{i+1,j+1} + \begin{bmatrix} 2 & 0 & 0 \\ 0 & 2 & 0 \\ 0 & 0 & \alpha \end{bmatrix} \begin{bmatrix} \phi_1 \\ \phi_2 \\ \phi_3 \end{bmatrix}^{i,j} \quad (D.35)$$

where  $\alpha = \epsilon/\Delta x$ . These equations are further simplified by doing the associated matrix inversion and using the information that

$$(1+\alpha)\phi_3^{i+1,j+1} = 3\phi_1^{i+1,j+1} + \alpha\phi_3^{i,j+1} \quad (D.36)$$

The use of Eq. (D.36) is correct because the solution progresses in the decreasing 'j' direction (decreasing  $y$ ), so that while solving for the solution at  $(i+1,j)$  grid point the solution at  $(i+1,j+1)$  grid point has already been obtained and satisfies Eqs. (D.35) applied at the  $(i+1,j+1)$  grid point. In other words, Eq. (D.36) is simply the last equation of Eqs. (D.35) when applied at the  $(i+1,j+1)$  grid point. At the  $y=1$  boundary, Eq. (D.36) is simply the differenced form of the boundary condition on  $\phi_3$  [see Eqs. (D.14)].

With the abovementioned operations the solution at (i+1,j) grid point can be written as

$$\phi_1^{i+1,j} = \phi_1^{i+1,j+1} + k_1(\phi_2^{i+1,j+1} - \phi_2^{i,j}) + k_2(\phi_3^{i,j+1} - \alpha\phi_3^{i,j}) \quad (D.37)$$

$$\phi_2^{i+1,j} = -k_3\phi_1^{i+1,j+1} + \phi_2^{i+1,j+1} + 2(\phi_1^{i,j} + \phi_2^{i,j}) - k_4(3\phi_1^{i+1,j} - \phi_3^{i,j} + \phi_3^{i,j+1}) \quad (D.38)$$

$$\phi_3^{i+1,j} = k_5\phi_1^{i+1,j} + k_4\phi_3^{i,j} \quad (D.39)$$

where

$$\begin{aligned} k_1 &= 2(1 + \alpha)/(2 - \alpha) \\ k_2 &= \alpha/(2 - \alpha) \\ k_3 &= (2 - \alpha)/(1 + \alpha) \\ k_4 &= \alpha(1 + \alpha) \\ k_5 &= 3/(1 + \alpha) \end{aligned} \quad (D.40)$$

The values of these coefficients ( $k_1, k_2, k_3, k_4$  and  $k_5$ ) for  $\alpha=0, 1$  and  $3$  ( $\varepsilon=0, \Delta x$  and  $2\Delta x$ , respectively) are given in Table D.1. As can be seen from this table, for  $\alpha=0$  the coefficients are whole numbers and no division operations are involved while for  $\alpha=1$  and  $3$  only division by 2 and 4 is involved which introduces minimal errors (if any). Solutions were obtained with different grids for the cases of  $\alpha=0$  and  $1$ . Figures D.5 to D.7 show the solutions for the  $\alpha=0$  case, while Figs. D.8 to D.11 show the solutions for the  $\alpha=1$  case.

Figures D.5, D.6 and D.7 show the solutions for  $\phi_1, \phi_2$  and  $\phi_3$  at  $y=0$  for the case of  $\alpha=0$ . Solutions were obtained with  $\Delta x$  values of 0.0025, 0.005, 0.01, 0.025, 0.05 and 0.10 (corresponding to 6, 11, 21, 51, 101 and 201 grid points in the y-direction and 4000,

2000, 1000, 400, 200 and 100 steps, respectively, in the  $x$  direction). In each case the solution was marched from  $x = 0$  to  $x = 10$ , and the numerical results showed that for all these cases the solution error was exactly zero at all stages of marching. This is indeed to be expected, because the exact solutions are bilinear space functions [Eqs. (D.5)], and for such bilinear functions one-sided differences in the  $x$  and  $y$  directions are mathematically exact. It is important to note that these solutions have been obtained by putting in  $\alpha = 0$  in the differenced form of Eqs. (D.12). No singular behavior or associated numerical difficulty was encountered in doing so, and the solution was the exact bilinear solution to the differential-algebraic system of Eqs. (D.1). This confirms the earlier conclusion that the Eqs. (D.1) are the true limiting case of Eqs. (D.12) with  $\varepsilon = 0$ , and that this limit is valid and can be taken without any singular behavior.

The solutions  $\phi_1$ ,  $\phi_2$  and  $\phi_3$  at  $y = 0$  and for  $\alpha = 1$  are shown in Figs. D.8, D.9 and D.10, respectively. Solutions are presented for  $\Delta x$  values of 0.10, 0.025 and 0.01, corresponding to  $\Delta y$  values of 0.2, 0.05, and 0.02, respectively (corresponding to  $6 \times 100$ ,  $21 \times 400$  and  $51 \times 1000$  grid points, respectively). The results show that the solutions for  $\phi_1$  and  $\phi_2$  are exact, while the solution for  $\phi_3$  is not exact. However, it can be seen from Fig. 10 that with decreasing  $\Delta x$  the numerical solution of  $\phi_3$  starts approaching the exact solution. This behavior is explained by the fact that the actual solution of  $\phi_3$  for  $\varepsilon > 0$  has a nonlinear exponential behavior in the  $x$  direction, which can not be properly modeled by a simple backward-differenced approximation of the  $\phi_{3,x}$  term. However, this modeling improves as the marching step size ( $\Delta x$ ) is decreased, and this is exactly the behavior shown by the numerical results for  $\phi_3$ . The analysis presented in Section D.2 had shown that the solution of  $\phi_1$  and  $\phi_2$  for nonzero values of  $\alpha$  (or equivalently  $\varepsilon$ ) were composed of bilinear space functions. The numerical solutions of these variables do give the exact bilinear space variations and, thus, confirm the analytic solution of

Eqs. (D.12) obtained in Section D.3. Figure D.11 shows the percentage error in the solution of  $\phi_3$  for the three different step-size distributions that were tried. This clearly shows the improvement in accuracy obtained by a decreasing sequence of marching step sizes.

It is worth pointing out that we also attempted a solution of the aforementioned  $\alpha = 0$  case in which we numerically inverted the matrices rather than using the aforementioned coefficients ( $k_1$  to  $k_5$ ). In principal there should have been no difference in these two treatments; however, such was not the case. We tried the case with  $\Delta x = 0.01$  and found that solution suffered from truncation errors which grew in magnitude as the number of marching steps increased, and after a couple of hundred steps these errors significantly degenerated the solution accuracy. Again, the only difference between this calculation and the similar calculation using Eqs. (D.37-D.39) was the numerical accuracy of the solution, and had nothing to do with the character of the governing equations which remain time-like.

### D.3.3. Concluding Remarks on the Numerical Solution

Based on the results of this study following conclusion have been drawn.

- (a) The results of this numerical study confirm the analysis of Bhutta-Lewis model problem. These results show that the solution of the Bhutta-Lewis model problem can be properly and accurately marched, provided one controls or eliminates the numerical errors and maintains solution accuracy.

- (b) The numerical results confirm that the model differential-algebraic problem is the true limiting case of a purely differential system with an unconditional time-like character. This limit can even be taken numerically without any singular behavior, and this limiting solution is the correct solution to the model differential-algebraic problem.
- (c) For marching problems which do not have an asymptotic limit, it is important to control the growth and generation of truncation errors. These truncation errors not only convect and grow in the same way as the actual solution, but in addition to this new truncation errors are also generated at each marching step. Consequently, the rate of growth of these errors may be more than the rate of growth of the actual solution. Thus, after a sufficient number of marching steps, these errors may become large enough to substantially degenerate the solution. In other words, in case of an inaccurate numerical algorithm the smaller the marching step-size, the larger the number of times we have to do an inaccurate solution in the  $y$  direction and, thus, the larger the number of times we cause the numerical errors to generate. This behavior could wrongfully be thought of as a problem caused by the small step-size; whereas, the small marching step has nothing to do with the problem except that by doing so the numerical inaccuracies start affecting the solution much sooner. The real solution to these problems lies not in the step-size manipulation, but in improving our solution accuracy and limiting or eliminating associated numerical truncation errors.

Table D.1. Coefficients of the Bidiagonal Implicit Scheme

$\alpha = \varepsilon/\Delta x$	Coefficients of the Bidiagonal Scheme				
	$k_1$	$k_2$	$k_3$	$k_4$	$k_5$
0	1	0	2	0	3
1	4	1	1/2	1/2	3/2
3	-8	-3	-1/4	3/4	3/4

KEY:

- o CASE 1 ( $\Delta y=0.10$ ,  $\Delta x=0.001$ ,  $k=0.01$ ,  $a^2=10$ ,  $\epsilon=0$ )
- △ CASE 2 ( $\Delta y=0.05$ ,  $\Delta x=0.001$ ,  $k=0.02$ ,  $a^2=10$ ,  $\epsilon=0$ )

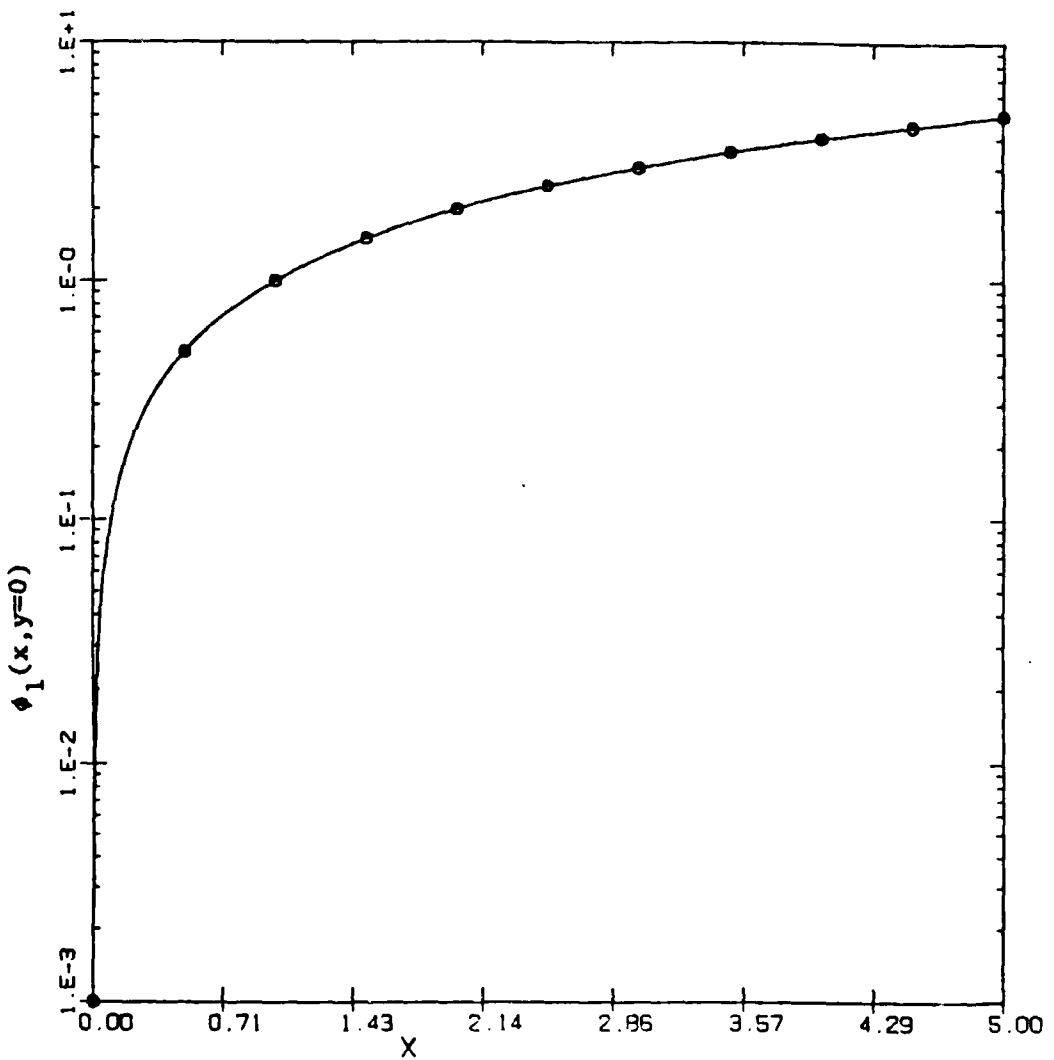


Fig. D.1. Solution for  $\phi_1(x, y=0)$  with the Lax method for the case of  $a^2=10$  and  $\epsilon=0$

KEY:

- CASE 1 ( $\Delta y=0.10$ ,  $\Delta x=0.001$ ,  $k=0.01$ ,  $a^2=10$ ,  $\epsilon=0$ )
- △ CASE 2 ( $\Delta y=0.05$ ,  $\Delta x=0.001$ ,  $k=0.02$ ,  $a^2=10$ ,  $\epsilon=0$ )

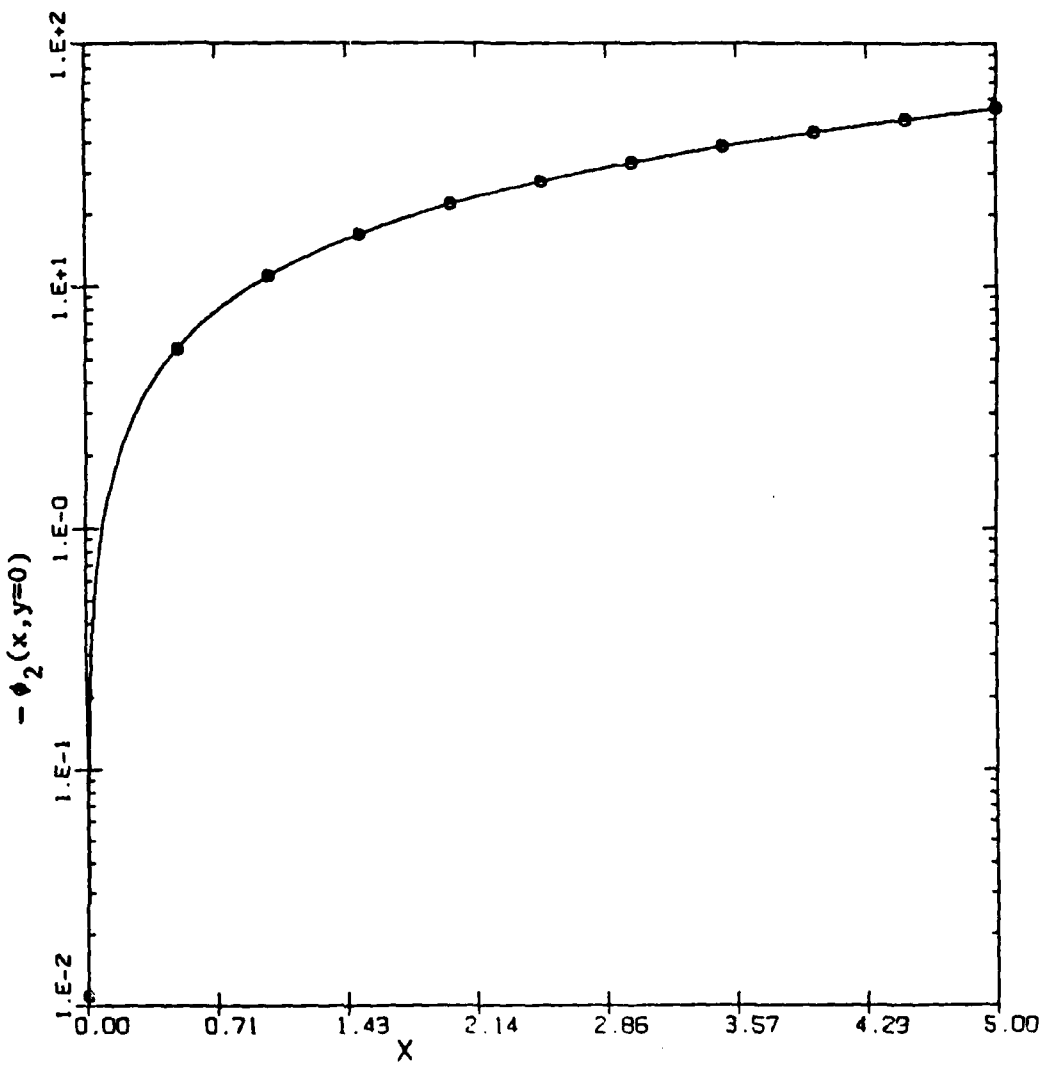


Fig. D.2. Solution for  $\phi_2(x, y=0)$  with the Lax method for the case of  $a^2=10$  and  $\epsilon=0$

KEY:

- o CASE 1 ( $\Delta y=0.10$ ,  $\Delta x=0.001$ ,  $k=0.01$ ,  $a^2=10$ ,  $\varepsilon=0$ )
- $\Delta$  CASE 2 ( $\Delta y=0.05$ ,  $\Delta x=0.001$ ,  $k=0.02$ ,  $a^2=10$ ,  $\varepsilon=0$ )

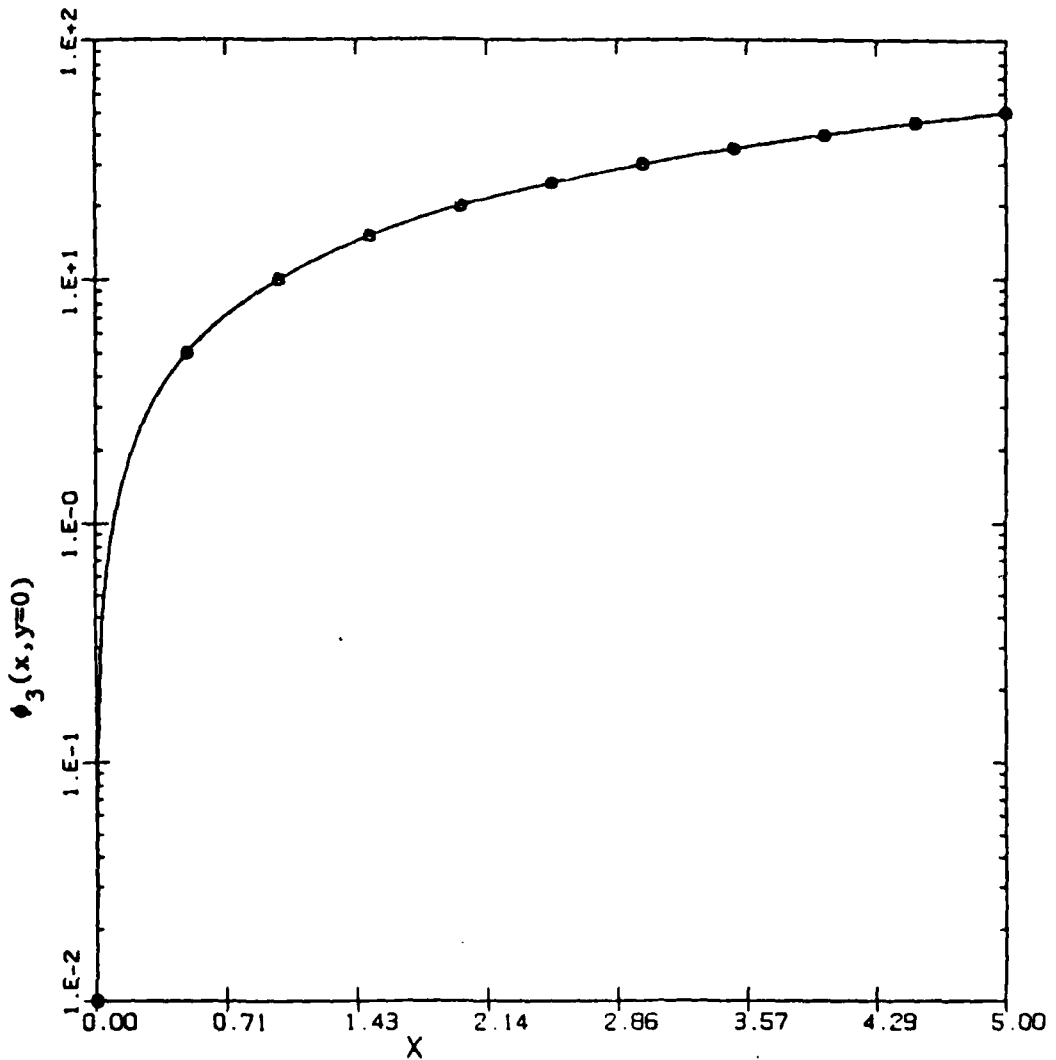


Fig. D.3. Solution for  $\phi_3(x, y=0)$  with the Lax method for the case of  $a^2=10$  and  $\varepsilon=0$

KEY:

- o  $k=0.01$  ( $\Delta y=0.10, \Delta x=0.001, a^2=10, \epsilon=0$ )
- $\Delta$   $k=0.05$  ( $\Delta y=0.10, \Delta x=0.005, a^2=10, \epsilon=0$ )
- +  $k=0.10$  ( $\Delta y=0.10, \Delta x=0.010, a^2=10, \epsilon=0$ )
- x  $k=0.20$  ( $\Delta y=0.10, \Delta x=0.020, a^2=10, \epsilon=0$ )
- $\diamond$   $k=1.00$  ( $\Delta y=0.10, \Delta x=0.100, a^2=10, \epsilon=0$ )

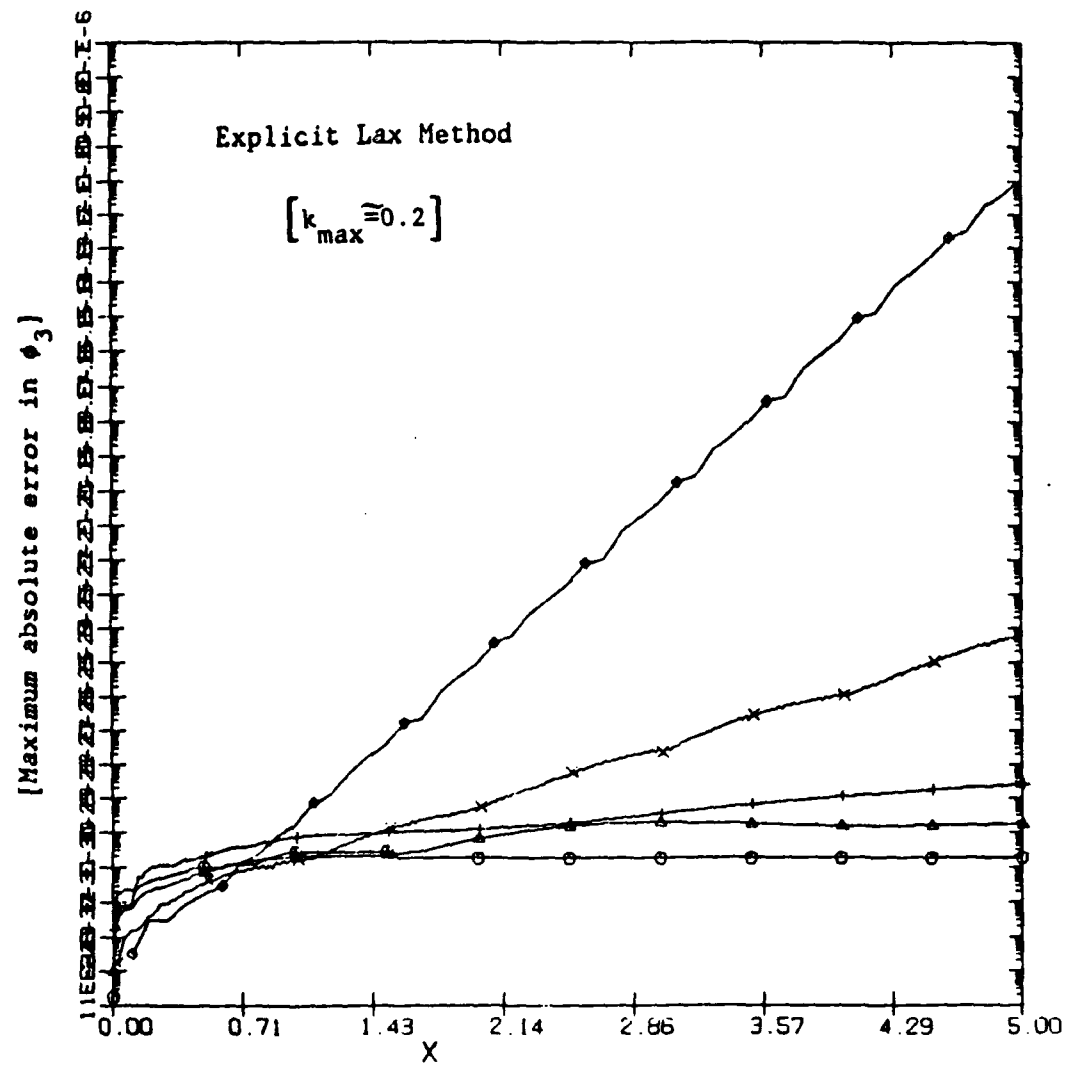


Fig. D.4. Effect of increasing the ratio  $k=\Delta x/\Delta y$  on the maximum absolute error in  $\phi_3$ .

KEY:

- $\Delta x=0.0025$  ( $\Delta y=0.0050$ ,  $k=0.50$ ,  $\varepsilon=0$ ,  $a^2=3$ )
- △  $\Delta x=0.0050$  ( $\Delta y=0.0100$ ,  $k=0.50$ ,  $\varepsilon=0$ ,  $a^2=3$ )
- +  $\Delta x=0.0100$  ( $\Delta y=0.0200$ ,  $k=0.50$ ,  $\varepsilon=0$ ,  $a^2=3$ )
- ×  $\Delta x=0.0250$  ( $\Delta y=0.0500$ ,  $k=0.50$ ,  $\varepsilon=0$ ,  $a^2=3$ )
- ◊  $\Delta x=0.0500$  ( $\Delta y=0.1000$ ,  $k=0.50$ ,  $\varepsilon=0$ ,  $a^2=3$ )
- ◆  $\Delta x=0.1000$  ( $\Delta y=0.2000$ ,  $k=0.50$ ,  $\varepsilon=0$ ,  $a^2=3$ )

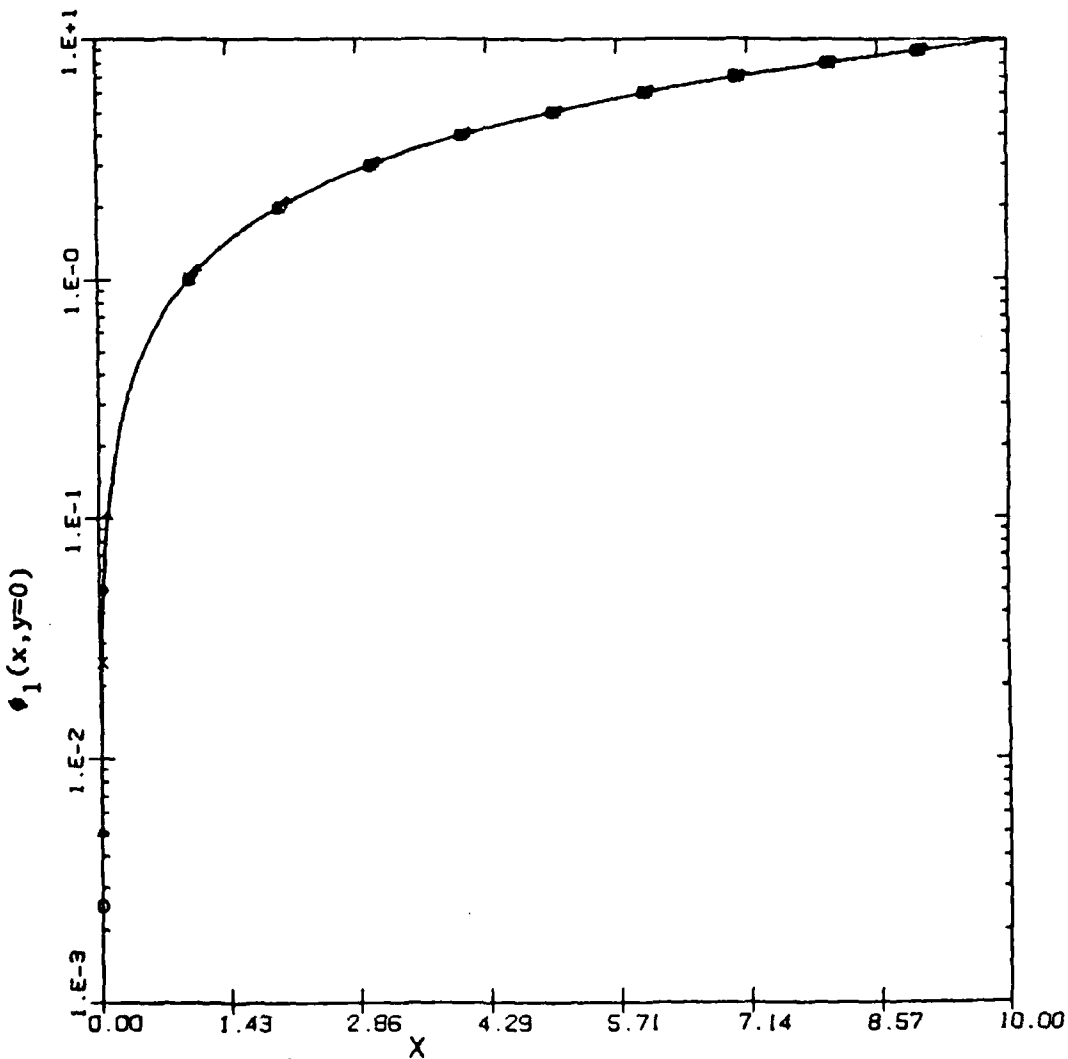


Fig. D.5. Solution for  $\phi_1(x, y=0)$  with the bidiagonal implicit method for  $a^2=3$  and  $\varepsilon=0$  ( $\alpha=0$ )

KEY:

- o  $\Delta x=0.0025$  ( $\Delta y=0.0050$ ,  $k=0.50$ ,  $\epsilon=0$ ,  $a^2=3$ )
- $\Delta$   $\Delta x=0.0050$  ( $\Delta y=0.0100$ ,  $k=0.50$ ,  $\epsilon=0$ ,  $a^2=3$ )
- +  $\Delta x=0.0100$  ( $\Delta y=0.0200$ ,  $k=0.50$ ,  $\epsilon=0$ ,  $a^2=3$ )
- x  $\Delta x=0.0250$  ( $\Delta y=0.0500$ ,  $k=0.50$ ,  $\epsilon=0$ ,  $a^2=3$ )
- $\diamond$   $\Delta x=0.0500$  ( $\Delta y=0.1000$ ,  $k=0.50$ ,  $\epsilon=0$ ,  $a^2=3$ )
- $\blacktriangleleft$   $\Delta x=0.1000$  ( $\Delta y=0.2000$ ,  $k=0.50$ ,  $\epsilon=0$ ,  $a^2=3$ )

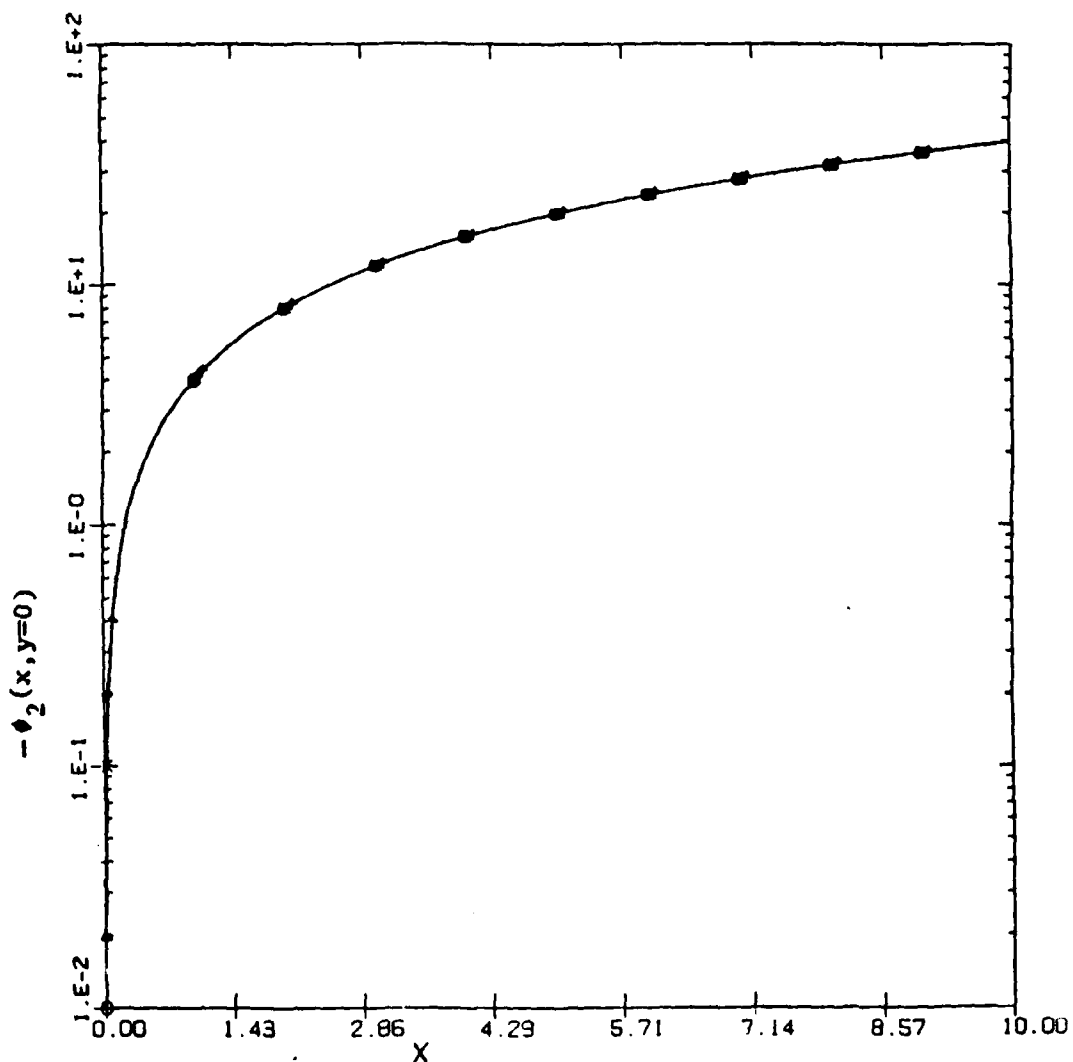


Fig. D.6. Solution for  $\phi_2(x, y=0)$  with the bidiagonal implicit method for  $a^2=3$  and  $\epsilon=0$  ( $\alpha=0$ )

KEY:

- $\Delta x=0.0025$  ( $\Delta y=0.0050$ ,  $k=0.50$ ,  $\epsilon=0$ ,  $a^2=3$ )
- △  $\Delta x=0.0050$  ( $\Delta y=0.0100$ ,  $k=0.50$ ,  $\epsilon=0$ ,  $a^2=3$ )
- +  $\Delta x=0.0100$  ( $\Delta y=0.0200$ ,  $k=0.50$ ,  $\epsilon=0$ ,  $a^2=3$ )
- ×  $\Delta x=0.0250$  ( $\Delta y=0.0500$ ,  $k=0.50$ ,  $\epsilon=0$ ,  $a^2=3$ )
- ◇  $\Delta x=0.0500$  ( $\Delta y=0.1000$ ,  $k=0.50$ ,  $\epsilon=0$ ,  $a^2=3$ )
- ▲  $\Delta x=0.1000$  ( $\Delta y=0.2000$ ,  $k=0.50$ ,  $\epsilon=0$ ,  $a^2=3$ )

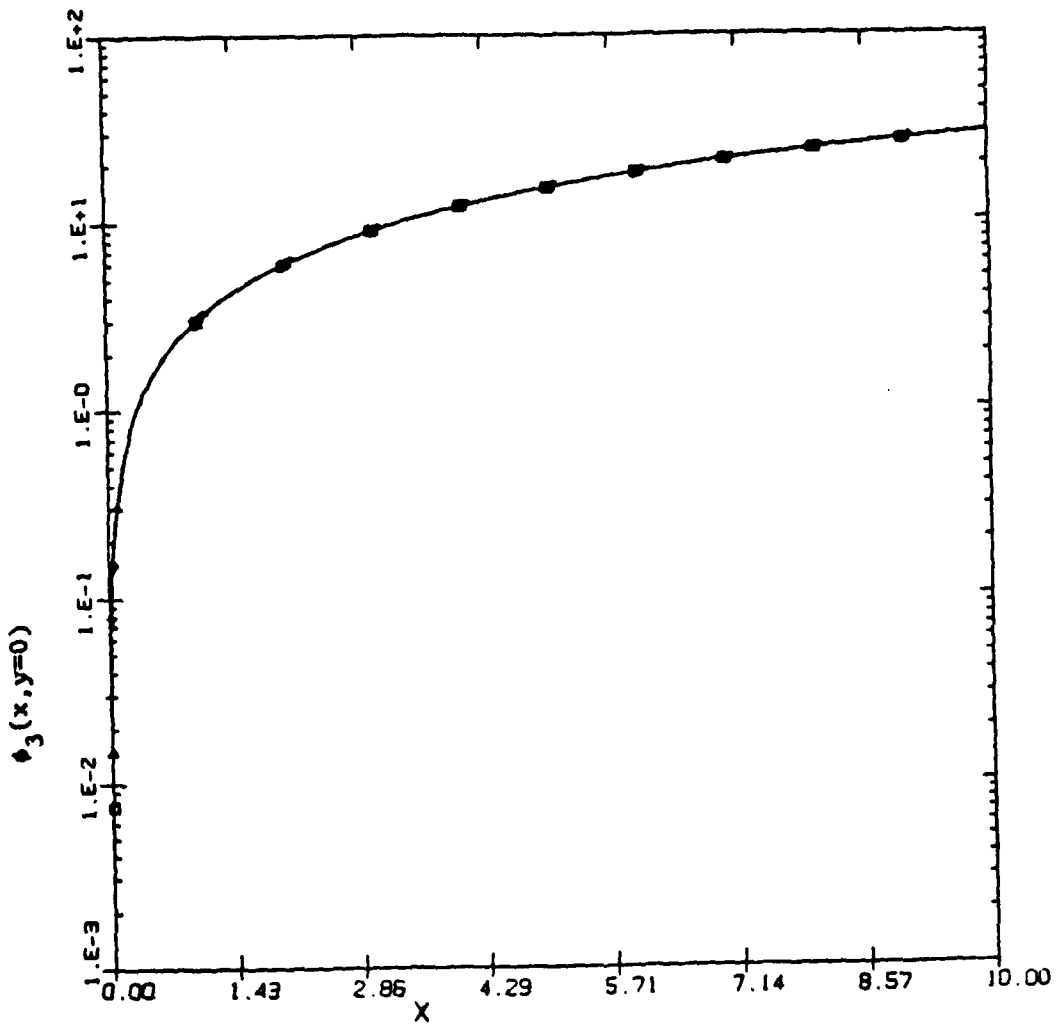


Fig. D.7. Solution for  $\phi_3(x, y=0)$  with the bidiagonal implicit method for  $a^2=3$  and  $\epsilon=0$  ( $\alpha=0$ )

KEY:

- o  $\Delta x=0.010$  ( $\Delta y=0.02$ ,  $k=0.50$ ,  $\epsilon=\Delta x$ ,  $a^2=3$ )
- $\Delta$   $\Delta x=0.025$  ( $\Delta y=0.05$ ,  $k=0.50$ ,  $\epsilon=\Delta x$ ,  $a^2=3$ )
- +  $\Delta x=0.100$  ( $\Delta y=0.20$ ,  $k=0.50$ ,  $\epsilon=\Delta x$ ,  $a^2=3$ )

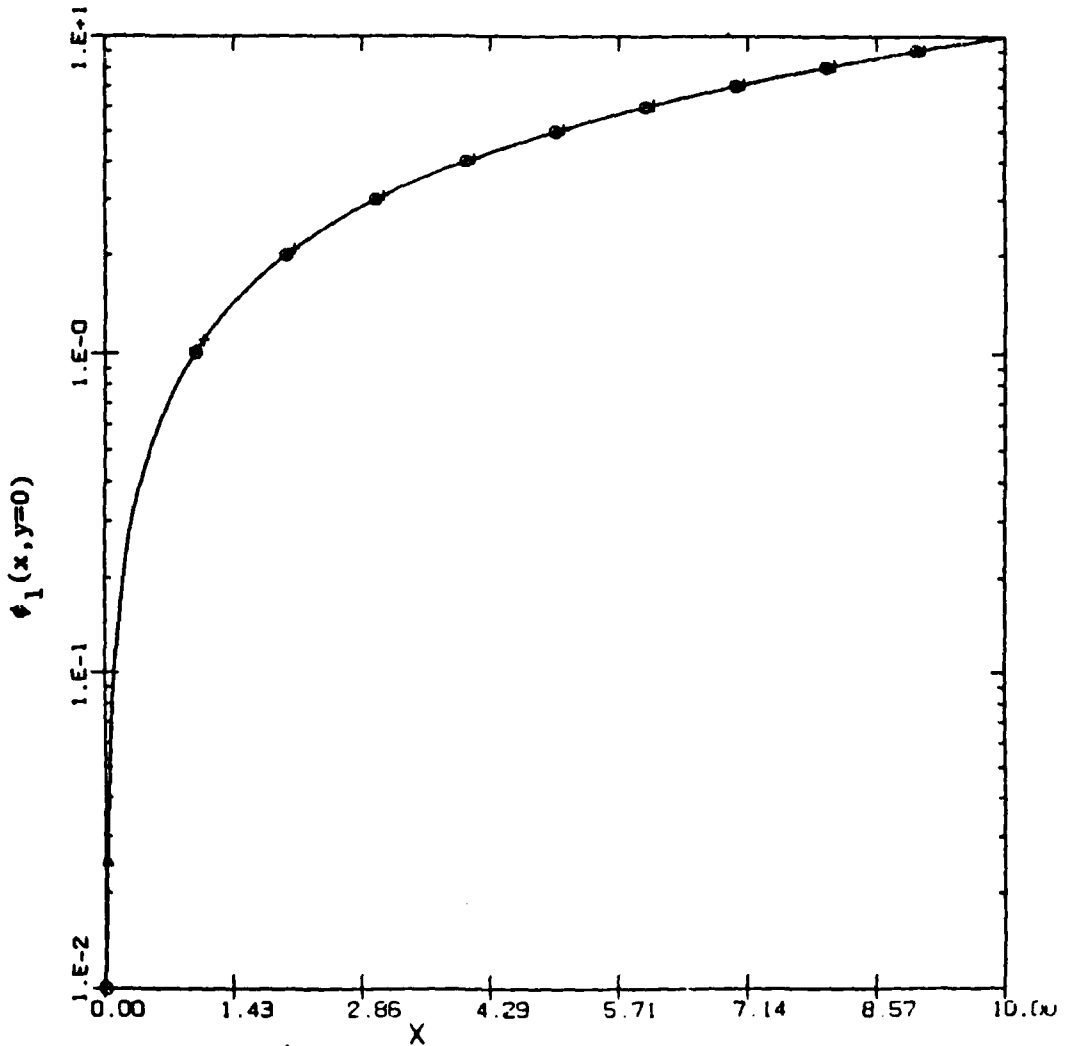


Fig. D.8. Solution for  $\phi_1(x, y=0)$  with the bidiagonal implicit method for  $a^2=3$  and  $\epsilon=\Delta x$  ( $\alpha=1$ )

KEY:

- $\Delta x=0.010$  ( $\Delta y=0.02$ ,  $k=0.50$ ,  $\epsilon=\Delta x$ ,  $a^2=3$ )
- △  $\Delta x=0.025$  ( $\Delta y=0.05$ ,  $k=0.50$ ,  $\epsilon=\Delta x$ ,  $a^2=3$ )
- +  $\Delta x=0.100$  ( $\Delta y=0.20$ ,  $k=0.50$ ,  $\epsilon=\Delta x$ ,  $a^2=3$ )

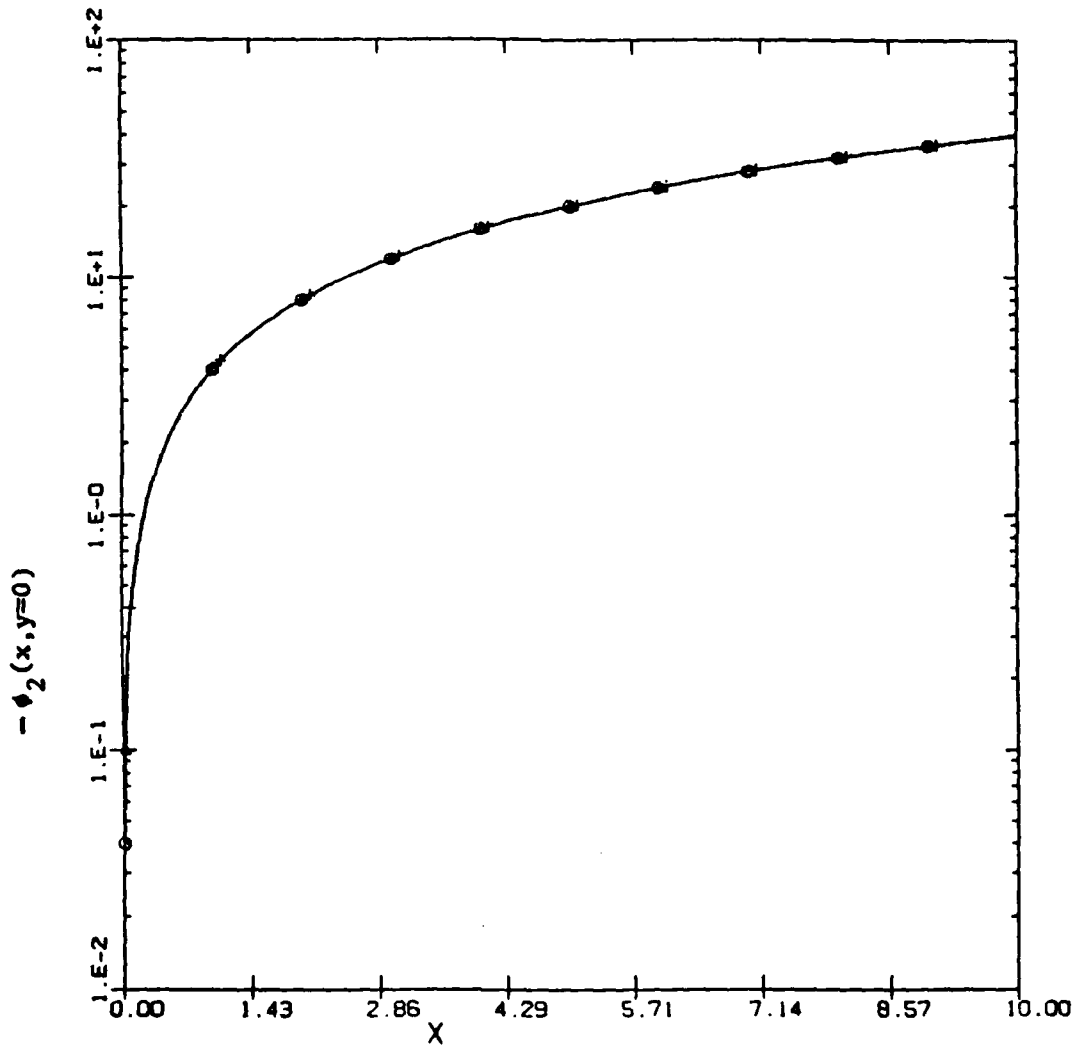


Fig. D.9. Solution for  $\phi_2(x, y=0)$  with the bidiagonal implicit method for  $a^2=3$  and  $\epsilon=\Delta x$  ( $\alpha=1$ )

KEY:

- o  $\Delta x=0.010$  ( $\Delta y=0.02$ ,  $k=0.50$ ,  $\epsilon=\Delta x$ ,  $a^2=3$ )
- $\Delta$   $\Delta x=0.025$  ( $\Delta y=0.05$ ,  $k=0.50$ ,  $\epsilon=\Delta x$ ,  $a^2=3$ )
- +  $\Delta x=0.100$  ( $\Delta y=0.20$ ,  $k=0.50$ ,  $\epsilon=\Delta x$ ,  $a^2=3$ )

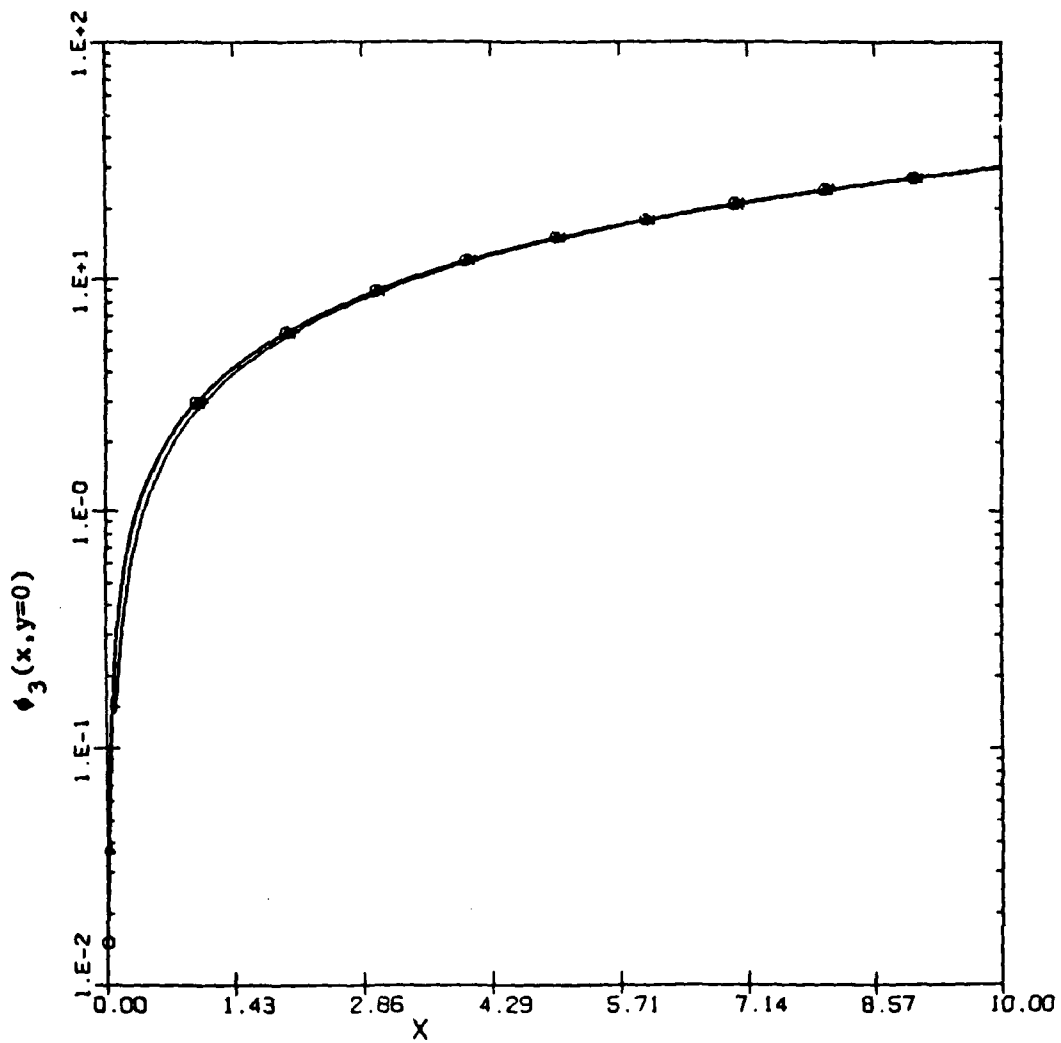


Fig. D.10. Solution for  $\phi_3(x, y=0)$  with the bidiagonal implicit method for  $a^2=3$  and  $\epsilon=\Delta x$  ( $\alpha=1$ )

KEY:

- $\Delta x=0.010$  ( $\Delta y=0.02$ ,  $k=0.50$ ,  $\epsilon=\Delta x$ ,  $a^2=3$ )
- △  $\Delta x=0.025$  ( $\Delta y=0.05$ ,  $k=0.50$ ,  $\epsilon=\Delta x$ ,  $a^2=3$ )
- +  $\Delta x=0.100$  ( $\Delta y=0.20$ ,  $k=0.50$ ,  $\epsilon=\Delta x$ ,  $a^2=3$ )

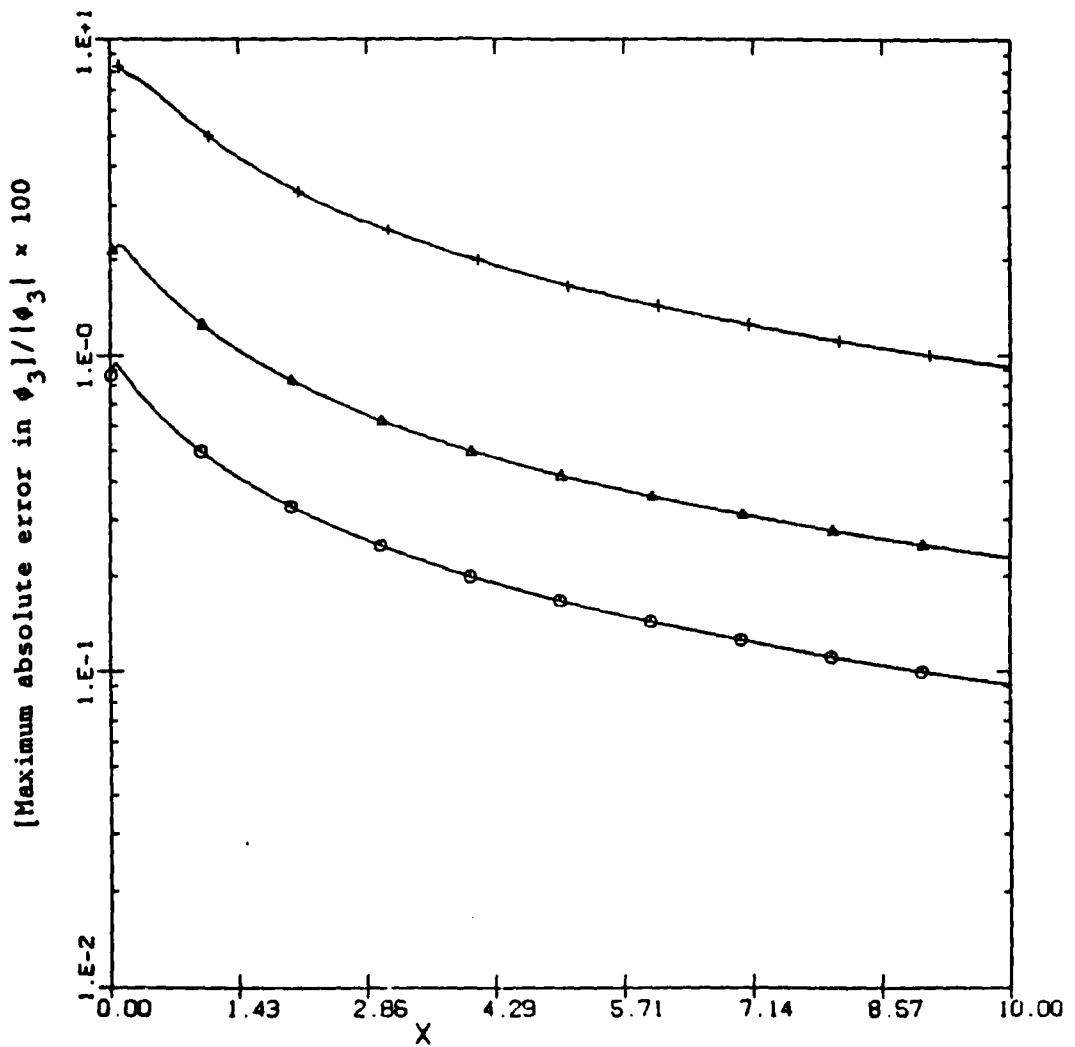


Fig. D.11. Improvement in the solution of  $\phi_3$  by decreasing the marching step size ( $\Delta x$ ) for  $a^2=3$  and  $\epsilon=\Delta x$  ( $\alpha=1$ ) and using the bidiagonal implicit method

## REFERENCES

Bhutta, B.A., and Lewis, C.H., (1985a) "Low Reynolds Number Flows Past Complex Multiconic Geometries," AIAA Paper No. 85-0362, Jan. 1985.

Bhutta, B.A. and Lewis, C.H., (1985b) "An Implicit Parabolized Navier-Stokes Scheme for High-Altitude Reentry Flows," AIAA Paper No. 85-0036, Jan. 1985.

Bhutta, B.A., and Lewis, C.H., (1985c) "Prediction of Three-Dimensional Hypersonic Reentry Flows Using a PNS Scheme," AIAA Paper No. 85-1604, July 1985.

Bhutta, B.A., and Lewis C.H., (1985d) "Parabolized Navier-Stokes Predictions of High-Altitude Reentry Flowfields," VRA-TR-85-02, VRA, Inc., Blacksburg, VA, April 1985.

Bhutta, B.A., Lewis, C.H. and Kautz II, F.A., (1985a) "A Fast Fully-Iterative Parabolized Navier-Stokes Scheme for Chemically-Reacting Reentry Flows," AIAA Paper No. 85-0926, June 1985.

Bhutta, B.A., Kautz II, F.A., and Lewis, C.H., (1985b) "Influence of Aerodynamic Prediction Methodology on Performance Evaluation of Reentry Vehicle Configurations", Journal of Spacecraft and Rockets, Vol. 22, Sept.-Oct. 1985, pp. 541-547.

Chaussee, D.S., Patterson, J.L., Kutler, P., Pulliam, T.H., and Steger, J.L., (1981) "A Numerical Simulation for Hypersonic Viscous Flows Over Arbitrary Geometries at High Angle of Attack," AIAA Paper No. 81-0050, Jan. 1981.

Cleary, J.W., (1969) "Effects of Angle of Attack and Bluntness on Laminar Heating-Rate Distribution of a 15° Cone at a Mach Number of 10.6," NASA TN D-5450, October 1969.

Guidos, B.J., and Sturek, W.B., (1987) "Computational Aerodynamic Analysis for a Range-Limited 25mm Training Round," BRL-TR-2833, US Army Ballistic Research Laboratory, Aberdeen Proving Ground, Maryland, August 1987.

Helliwell, W.S., Dickinson, R.P., and Lubard, S.C., (1980) "Viscous Flows Over Arbitrary Geometries at High Angle of Attack," AIAA Paper No. 80-0064, Jan. 1980.

Kaul, U.K., and Chaussee, D.S., (1983) "AFWAL Parabolized Navier-Stokes Coded: 1983 AFWAL/NASA Merged Baseline Version", AFWAL-TR-83-3118, Flight Dynamics Laboratory, AF Wright Aeronautical Laboratories, Wright-Patterson AFB, OH, Oct. 1983.

Kim, J., (1984) "Computation of Three-Dimensional Turbulent Flow with Parabolized Navier-Stokes Equations and K-E Turbulence Model," Masters Thesis, Mechanical and Aerospace Engineering Department, University of Delaware, January 1984.

Kumar, A., (1986) "High-Speed Inlet Analysis," Paper presented at the First National Aerospace Plane Technology Symposium, Langley Research Center, Hampton, Va., May 1986.

Lubard, S.C., and Helliwell, W.S., (1973) "Calculation of the Flow on a Cone at High Angle of Attack," Report No. RDA-TR-150, R & D Associates, Santa Monica, CA, Feb. 1973.

Miner, E.W., Anderson, E.C., and Lewis, C.H., (1971) "A Computer Program for Two-Dimensional and Axisymmetric Nonreacting Perfect Gas and Equilibrium Chemically Reacting Laminar Transitional and/or Turbulent Boundary Layer Flows," Virginia Polytechnic Institute and State University, Blacksburg, VA, VPI-E-71-8, May 1971.

Murray, A.L., and Lewis, C.H. (1978), "Hypersonic Three-Dimensional Viscous Shock-Layer Flows Over Sphere-Cones at High Altitudes and High Angles of Attack, VPI&SU AERO-078, Virginia Polytechnic Institute and State University, Blacksburg, VA, January 1978.

Peng, T.C., and Pindroh, A.L., (1962) "An Improved Calculation of Gas Properties at High Temperature Air," Boeing Report D2-11722, Aerospace Division, The Boeing Co., 1962.

Peyert, R. and Viviand, H., (1975) "Computations of Viscous Compressible Flows Based on the Navier-Stokes Equations," AGARD-AG-212, 1975.

Richardson, P., (1986) "High-Speed configuration Aerodynamic CFD," Paper presented at the First National Aerospace Plane Technology Symposium, Langley Research Center, Hampton, Va, May 1986.

Rizk, Y.M., Chaussee, D.S., and Mcrae, D.S., (1981) "Computations of Hypersonic Viscous Flow Around Three-Dimensional Bodies at High Angle of Attack," AIAA Paper 81-1261, 1981.

Sahu, J., (1984) "Navier-Stokes Computational Study of Axisymmetric Transonic Turbulent Flows with a Two-Equation Model of Turbulence," Ph.D Dissertation, Mechanical and Aerospace Engineering Department, University of Delaware, June 1984.

Sahu, J., (1986) "Drag Predictions for Projectiles at Transonic and Supersonic Speeds," BRL-MR-3523, US Army Ballistic Research Laboratory, Aberdeen Proving Ground, Maryland, June 1986.

Sahu, J., (1987) "Three-Dimensional Base Flow Calculations for Projectile at Transonic Velocity," BRL-MR-3610, US Army Ballistic Research Laboratory, Aberdeen Proving Ground, Maryland, June 1987.

Sahu, J., and Nietubicz, C.J., (1987) "Improved Numerical Predictions of Transonic Flow," BRL-TR-2784, US Army Ballistic Research Laboratory, Aberdeen Proving Ground, Maryland, March 1987.

Schiff, L.B. and Steger, J.L., (1979) "Numerical Simulation of Steady Supersonic Viscous Flows," AIAA Paper No. 79-0130, Jan. 1979.

Shanks, S.P., Srinivasan, G.R. and Nicolet, W.E., (1979) "AFWAL Parabolized Navier-Stokes Code: Formulation and User's-Manual," AFWAL-TR-823034, Air Force Flight Dynamics Laboratory, Wright Patterson AFB, OH, June 1979. Stalnaker, J.F., (1986) "Improvements to the AFWAL PNS Code Formulation," 85 Parabolized Navier-Stokes Workshop ... Transitioning Numerical Fluid Mechanics to the Design Environment, Bergamo Center, Dayton, OH, Sept 1985.

Thareja, R.R., Szema, K.Y., and Lewis, C.H., (1983a) "Chemical Equilibrium Laminar or Turbulent Three-Dimensional Viscous Shock-Layer Flows," Journal of Spacecraft and Rockets,

Thareja, R. R., Szema, K. Y., and Lewis, C. H., (1983b) "Viscous Shock-Layer Predictions for Hypersonic Laminar or Turbulent Flows in Chemical Equilibrium over the Windward Surface of a Shuttle-Like Vehicle," Progress in Astronautics and Aeronautics, Vol. 85, 1983. Vol. 20, No. 5, Sept. 1983, pp. 454-460.

Thompson, R.A., Lewis, C.H., and Kautz, II, F.A., (1983) "Comparison Techniques for Predicting 3-D Viscous Flows Over Ablated Shapes," AIAA Paper 8-0345, Jan. 1983.

Viviand, H., (1974) "Conservative Forms of Gas Dynamics Equations," La Recherche Aerospaciale, No. 1, Jan.-Feb. 1974, pp. 65-68.

Vigneron, Y.C., Rakich, J.V., and Tannehill, J.C., (1978) "Calculations of Supersonic Viscous Flows over Delta Wings with Sharp Subsonic Leading Edges," AIAA Paper No. 78-1137, July 1978.

Weinacht, P., Guidos, B.J., Sturek, W.B., and Hodes, B.A., (1986) "PNS Computations of Spinning Shell at Moderate Angles of Attack and for Long L/D/ Finned Projectiles," BRL-MR-3522, US Army Ballistic Research Laboratory, Aberdeen Proving Ground, Maryland, June 1986.

White, F.M., (1974) Viscous Fluid Flow, McGraw-Hill Book Co., 1974.

Table 1. Freestream conditions for test case

Quantity	
Mach number	10.600
Reynolds number	1.32E+5
Pressure (N/m <sup>2</sup> )	132.061
Density (Kg/m <sup>3</sup> )	9.71276
Temperature (K)	47.3377
Velocity (m/sec)	1.46E+3
Wall temperature (K)	300.000
Angle of attack (deg)	20.000

Table 2. Comparison of total computing times <sup>a</sup>

Case	x/Rn	Grid	Time <sup>a</sup>
	From-to	$\xi_1$ $\xi_2$ $\xi_3$	(m:s)
Case 1	1.75-17.5	28 x 50 x 31	4:45
Case 2	1.75-17.5	26 x 50 x 25	3:14
Case 3	1.75-17.5	26 x 50 x 17	2:07
Case 4	1.75-10.5	16 x 50 x 31	2:10

(a) On IBM 3090 with VS-compiler and scalar LEVEL=3 optimization

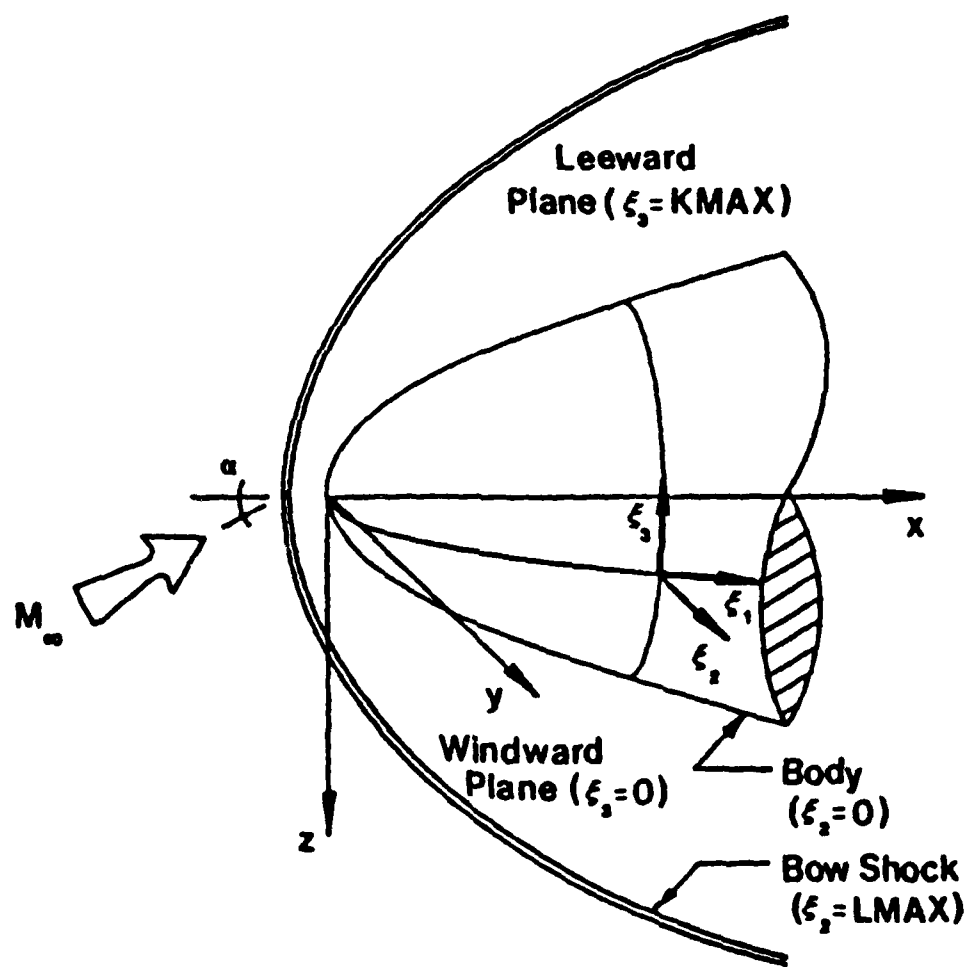
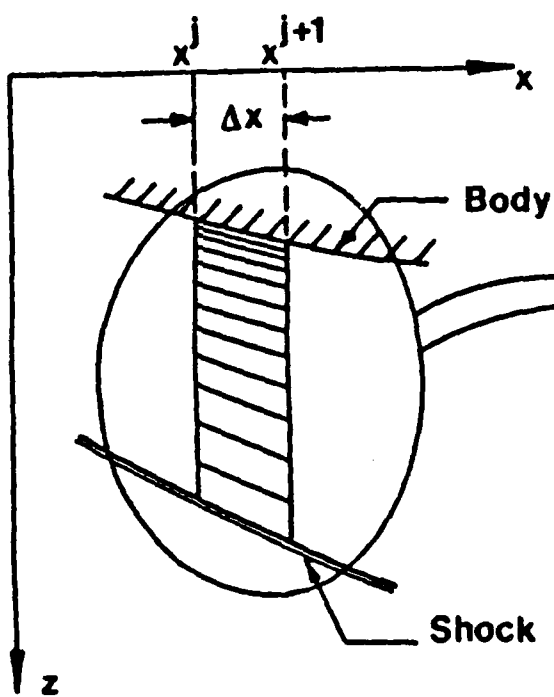


Figure 1. Coordinate system.

x-y-z Space



$\xi_1-\xi_2-\xi_3$  Space

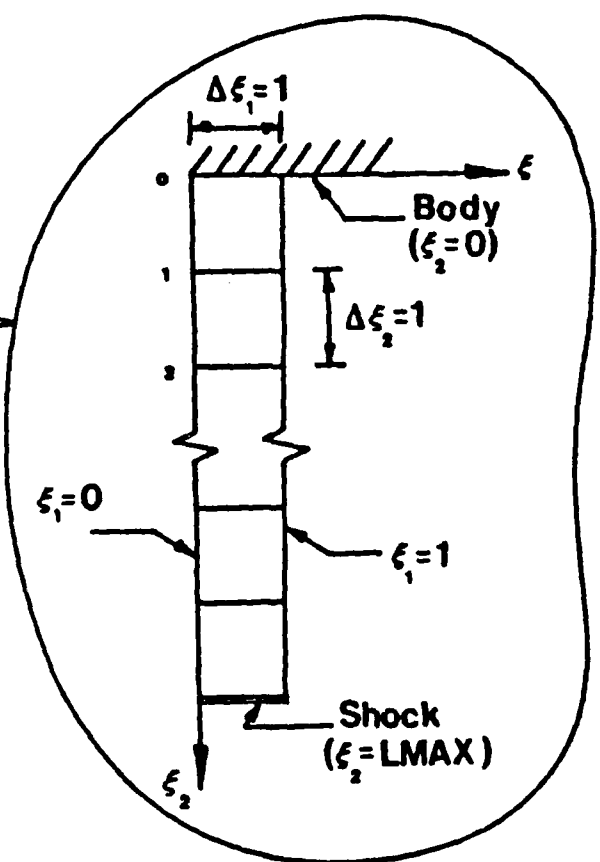


Figure 2. Coordinate transformation.

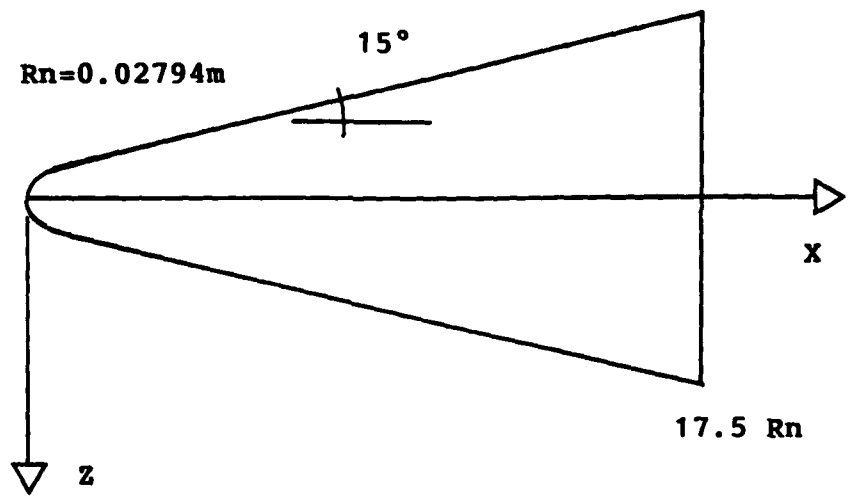


Figure 3. Sphere-cone vehicle geometry.

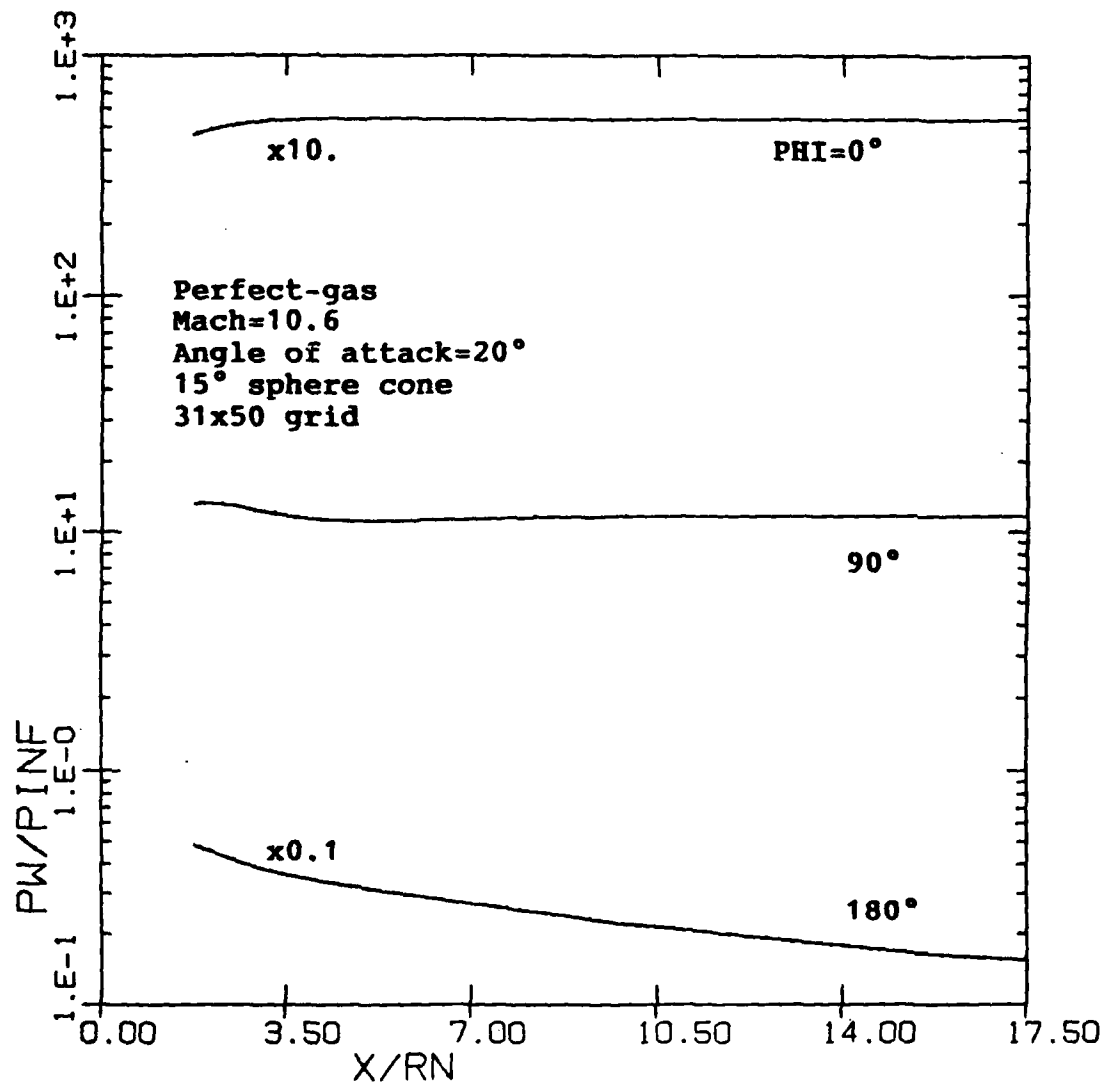


Figure 4. Axial distribution of wall pressures.

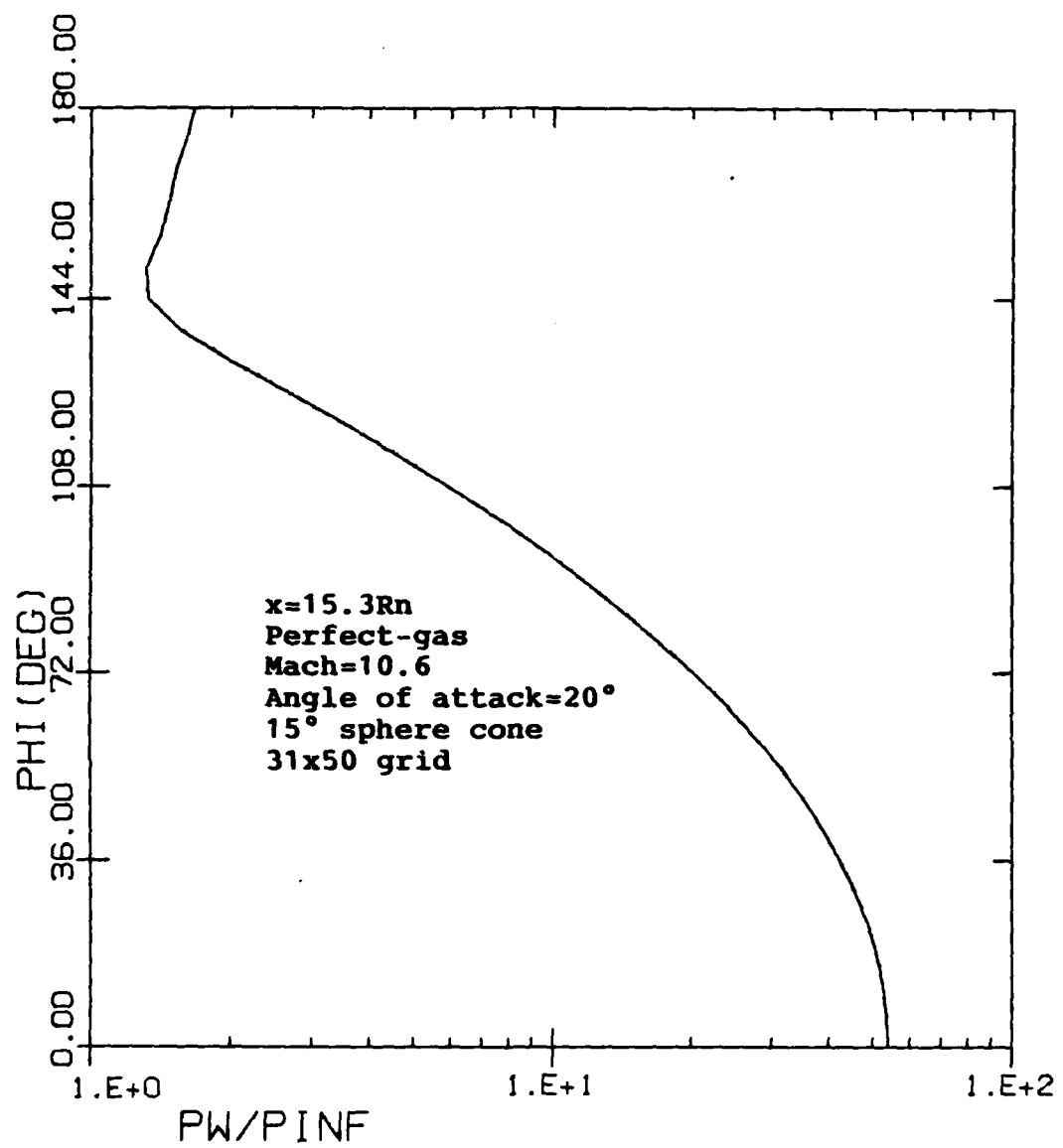


Figure 5. Crossflow distribution of wall pressures.

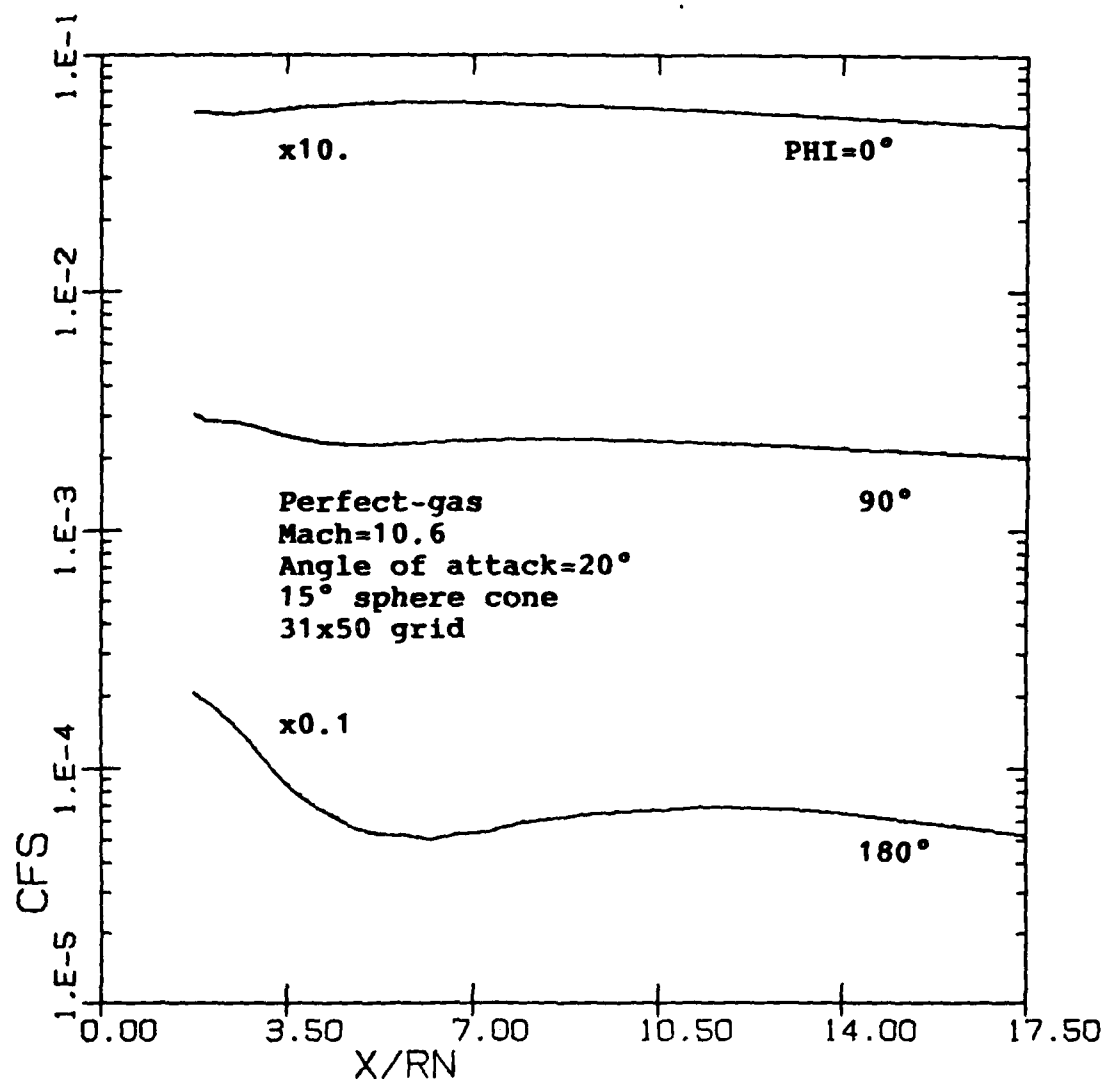


Figure 6. Axial distribution of skin-friction coefficient.

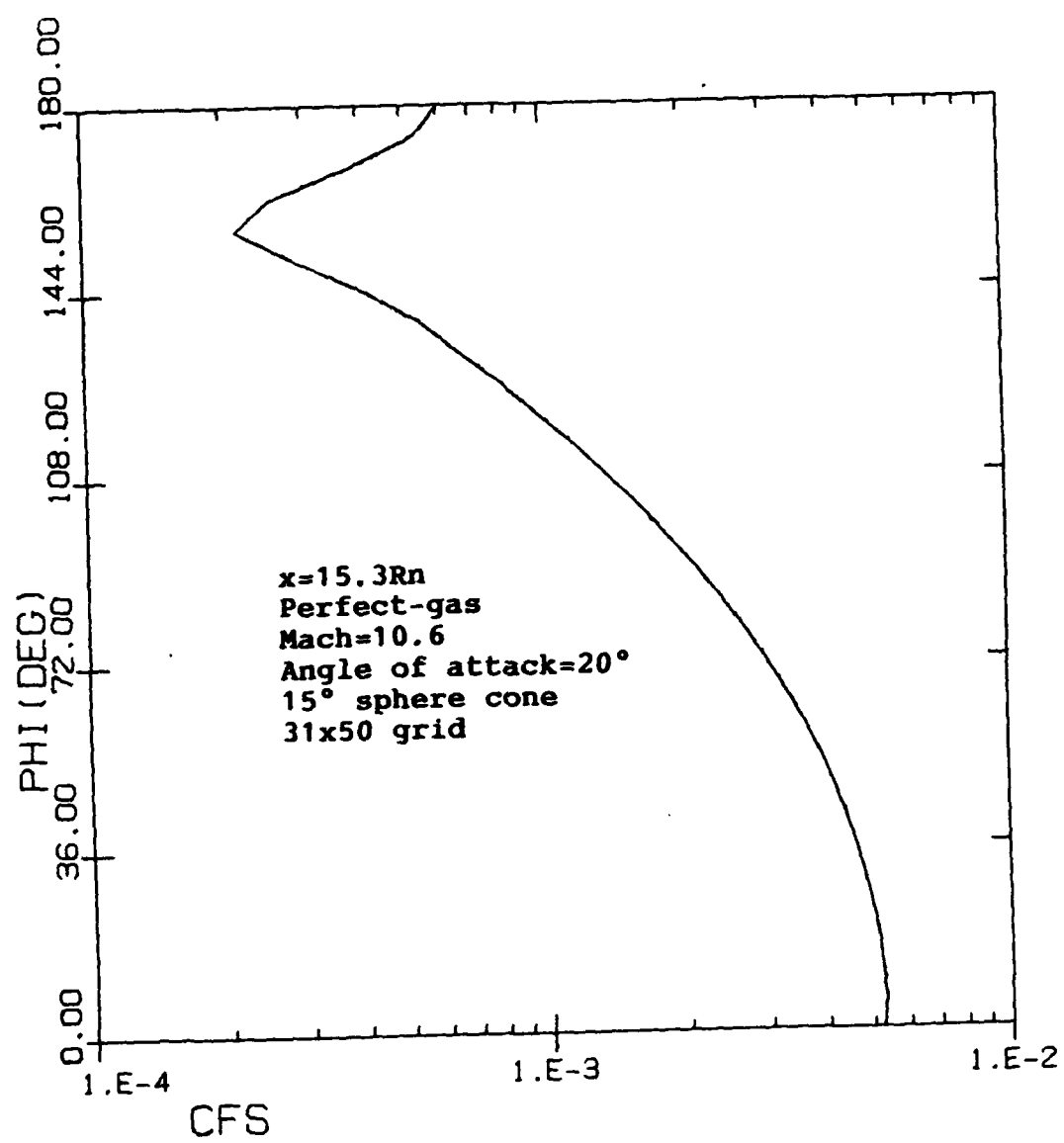


Figure 7. Crossflow distribution of skin-friction coefficient.

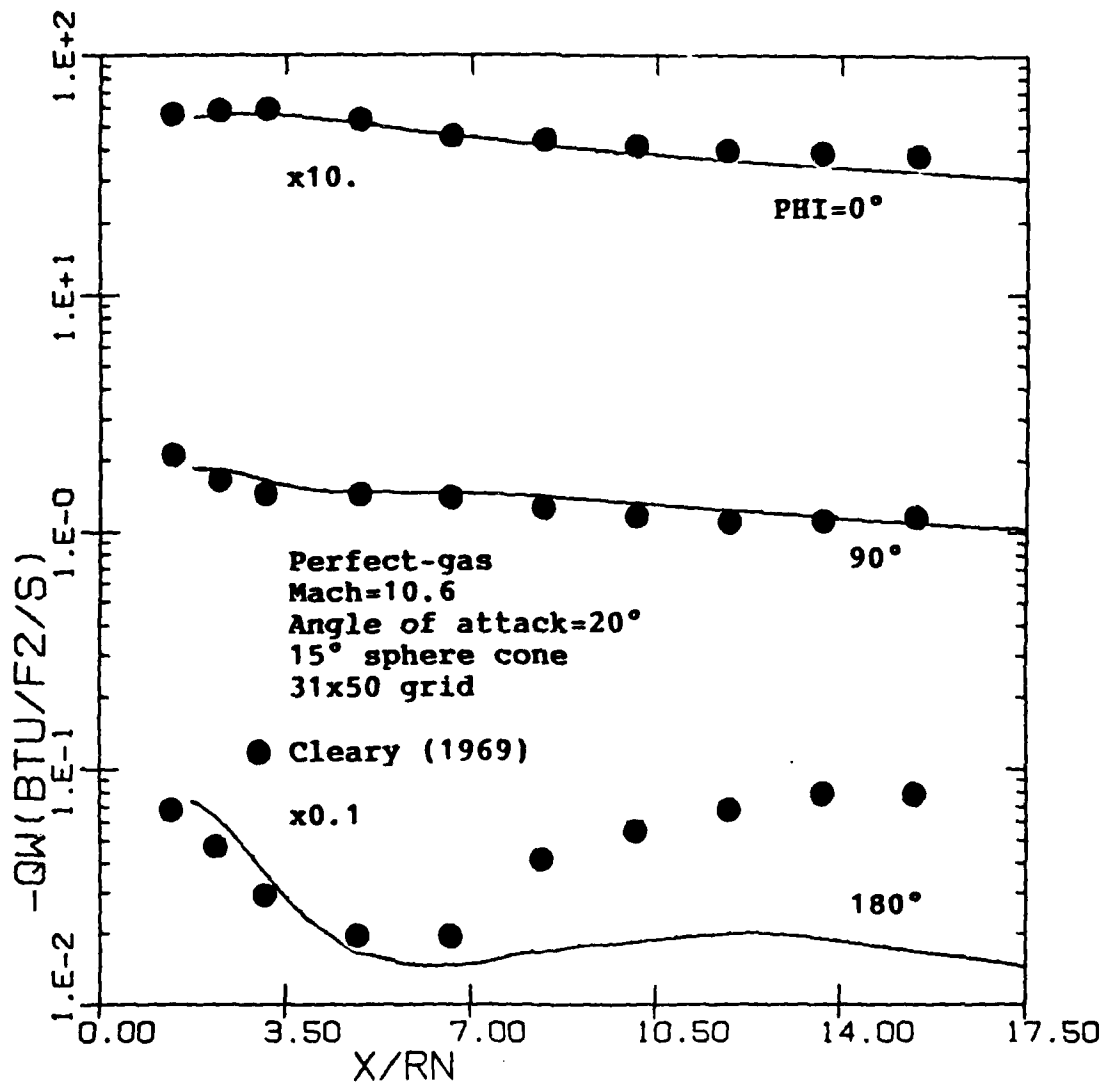


Figure 8. Axial distribution of wall heat-transfer rates.

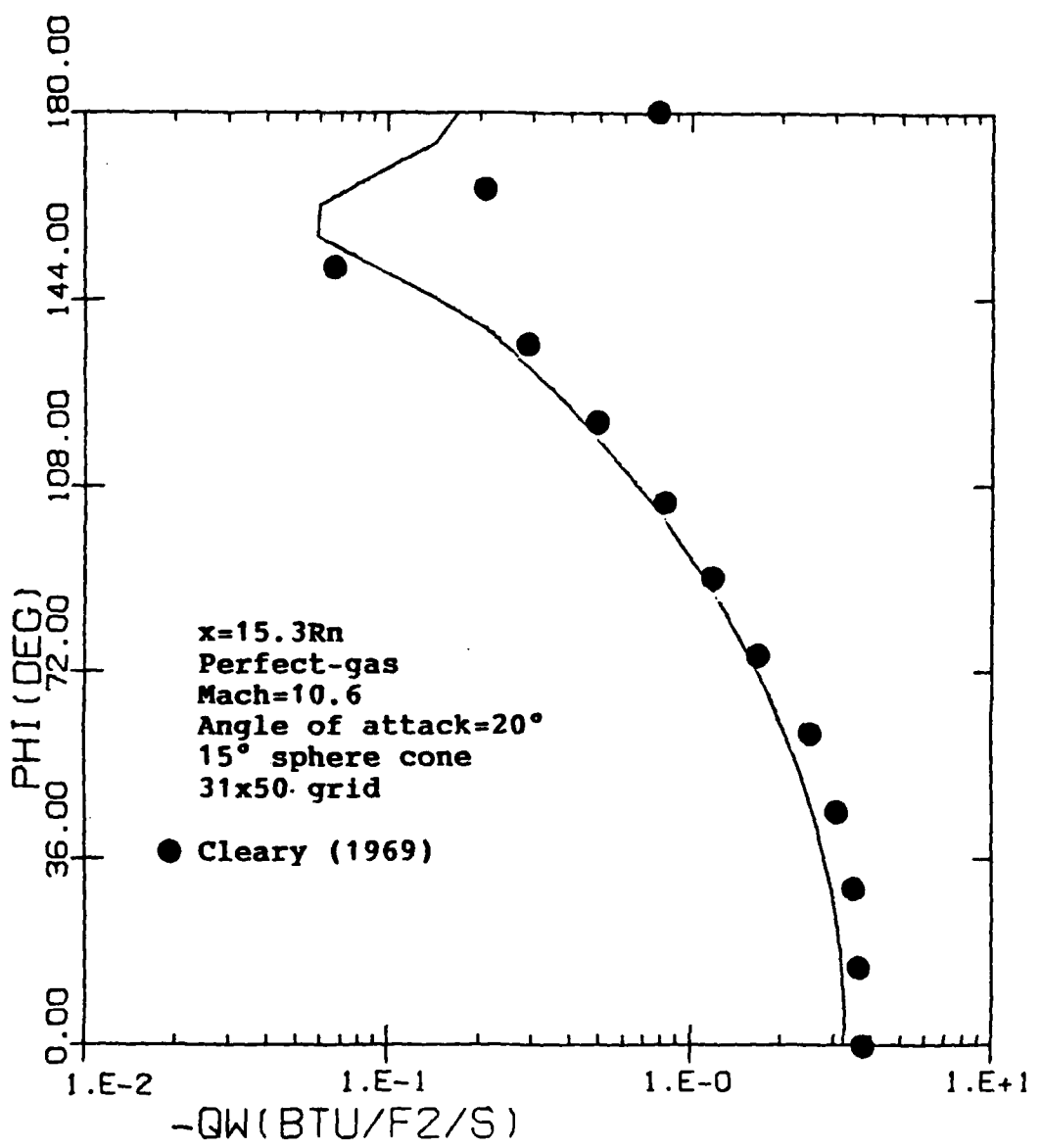


Figure 9. Crossflow distribution of wall heat-transfer rates.

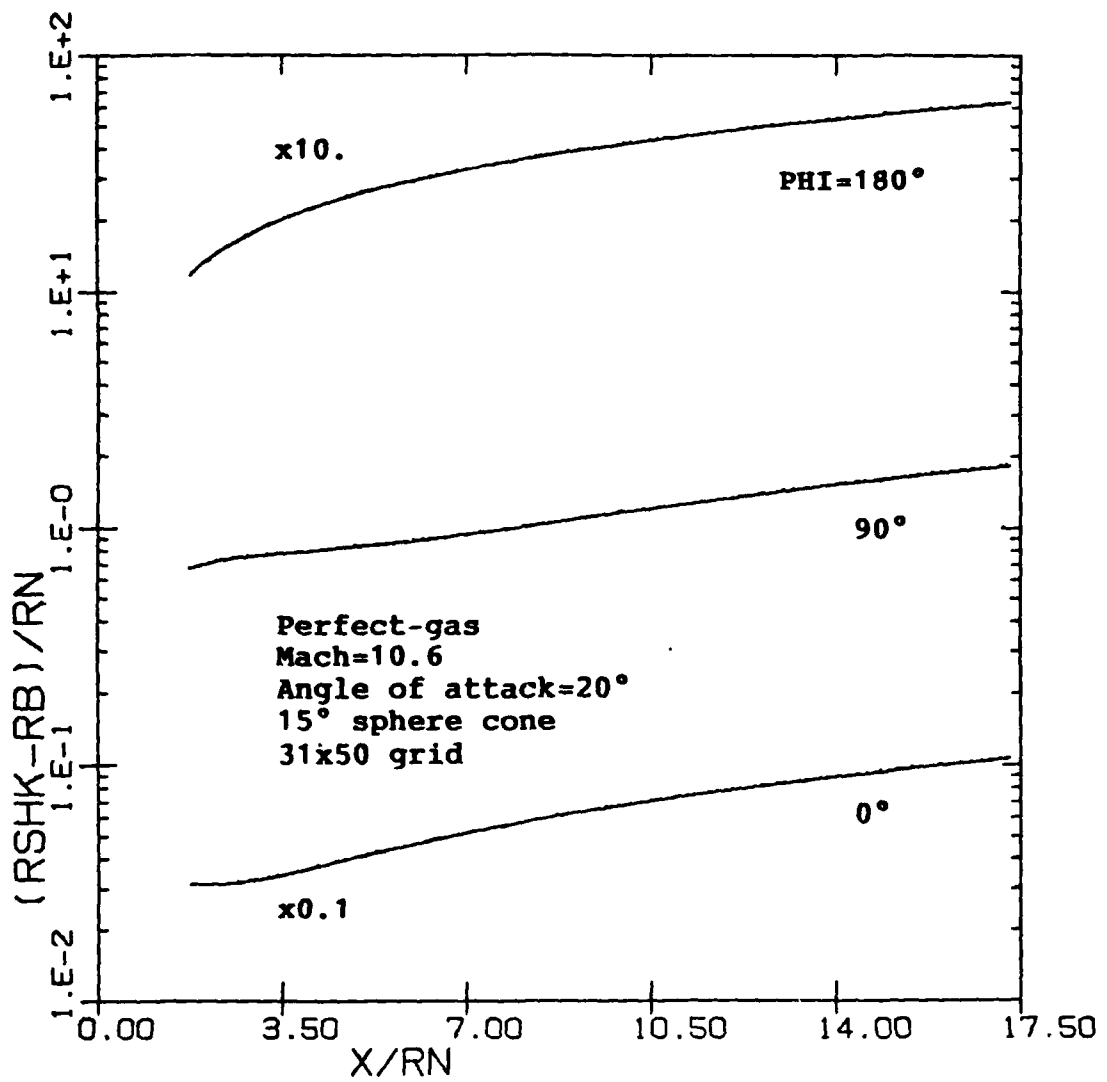


Figure 10. Axial variation of bow shock shape.

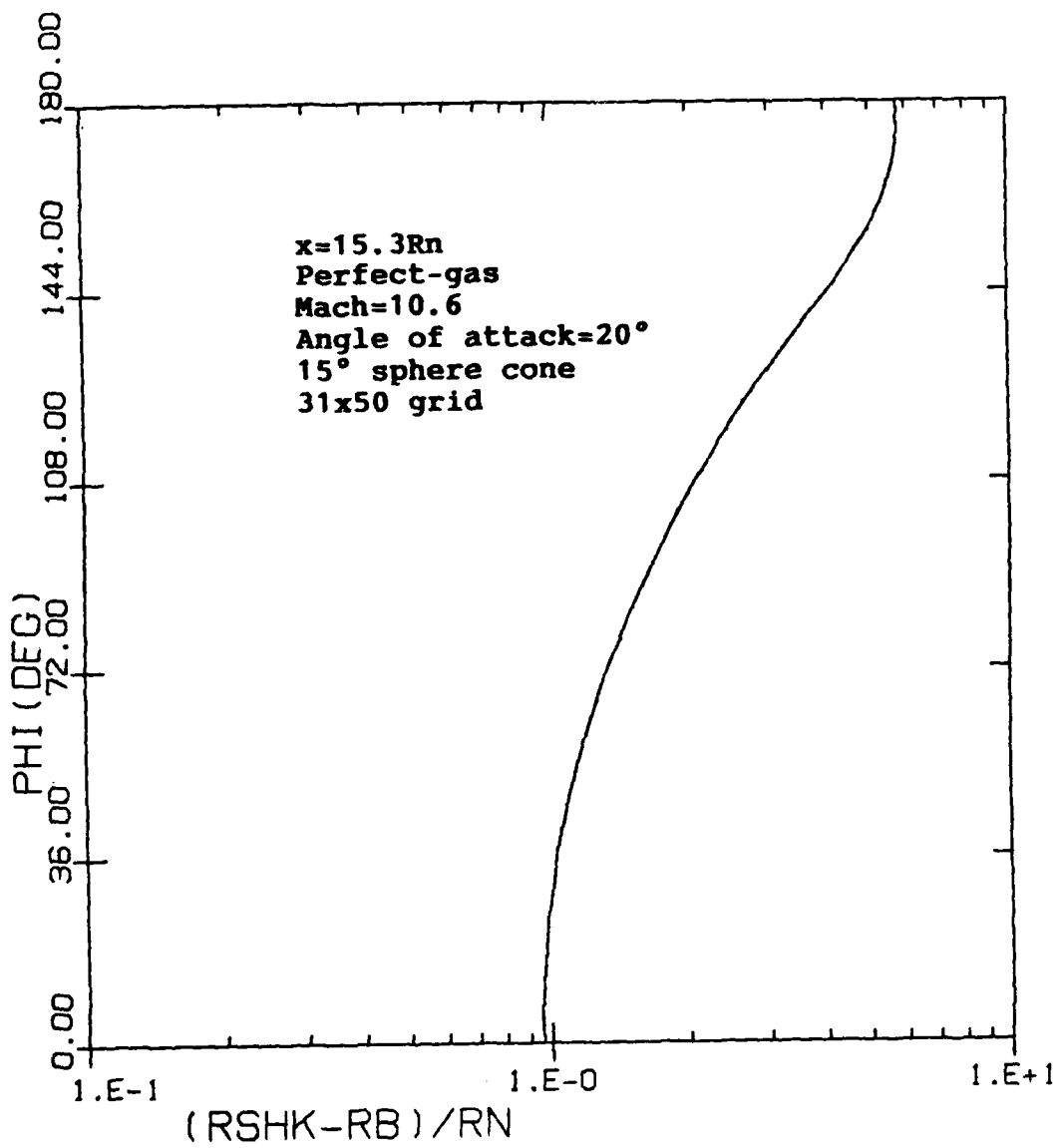


Figure 11. Crossflow variation of bow shock shape.

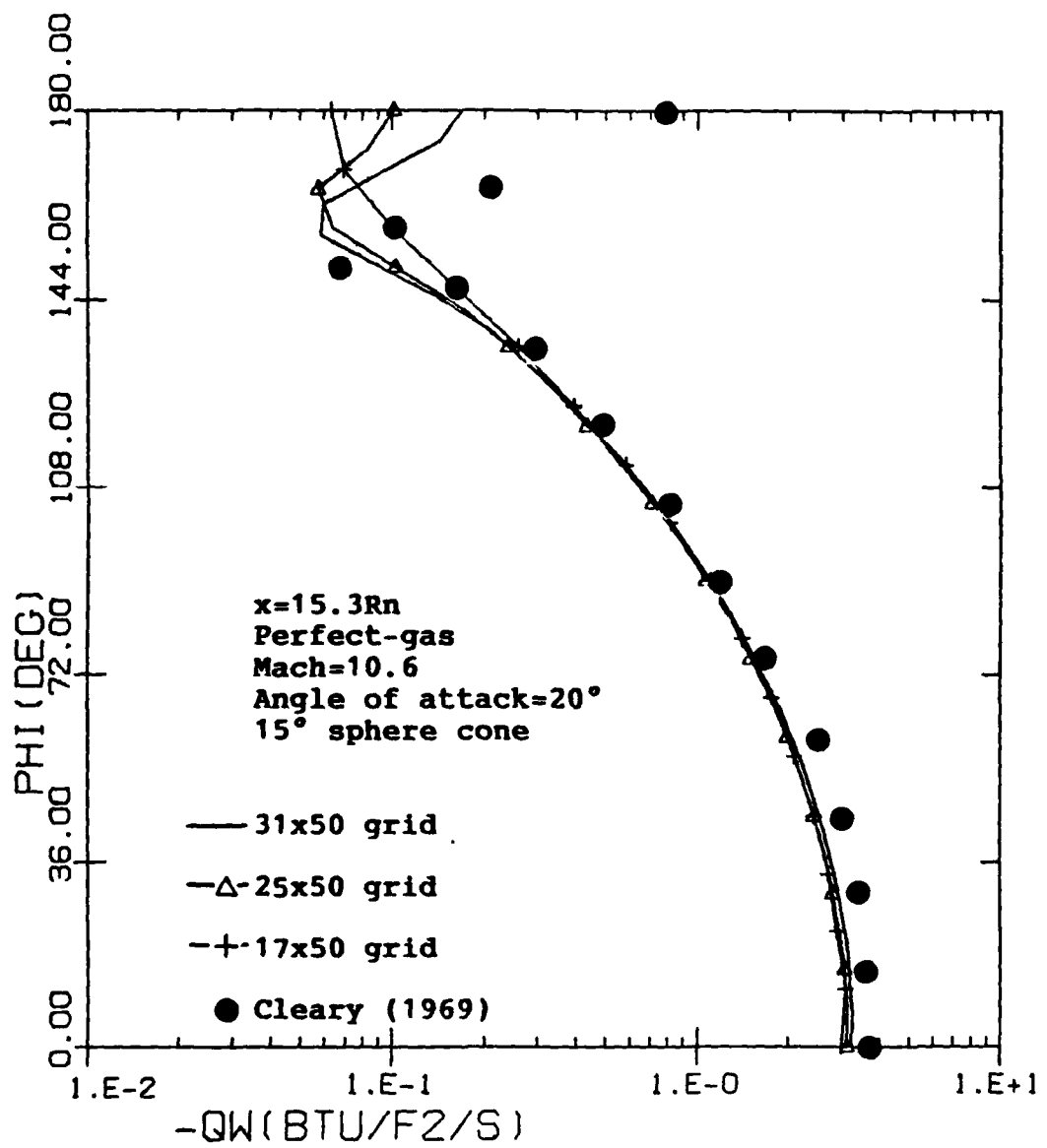


Figure 12. Effects of crossflow grid refinement on the wall heat-transfer rates.

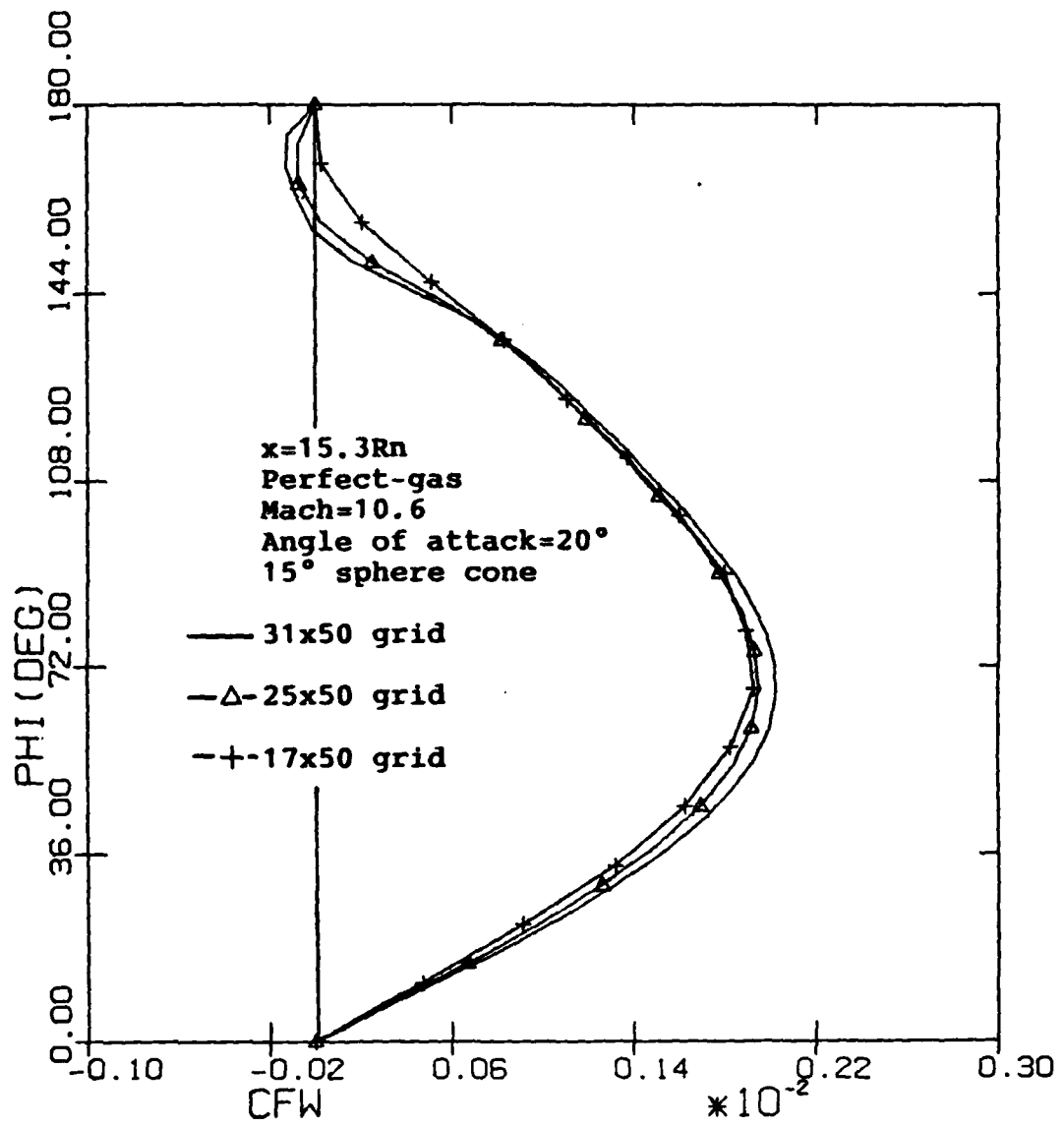


Figure 13. Effects of crossflow grid refinement on the crossflow skin-friction coefficient.

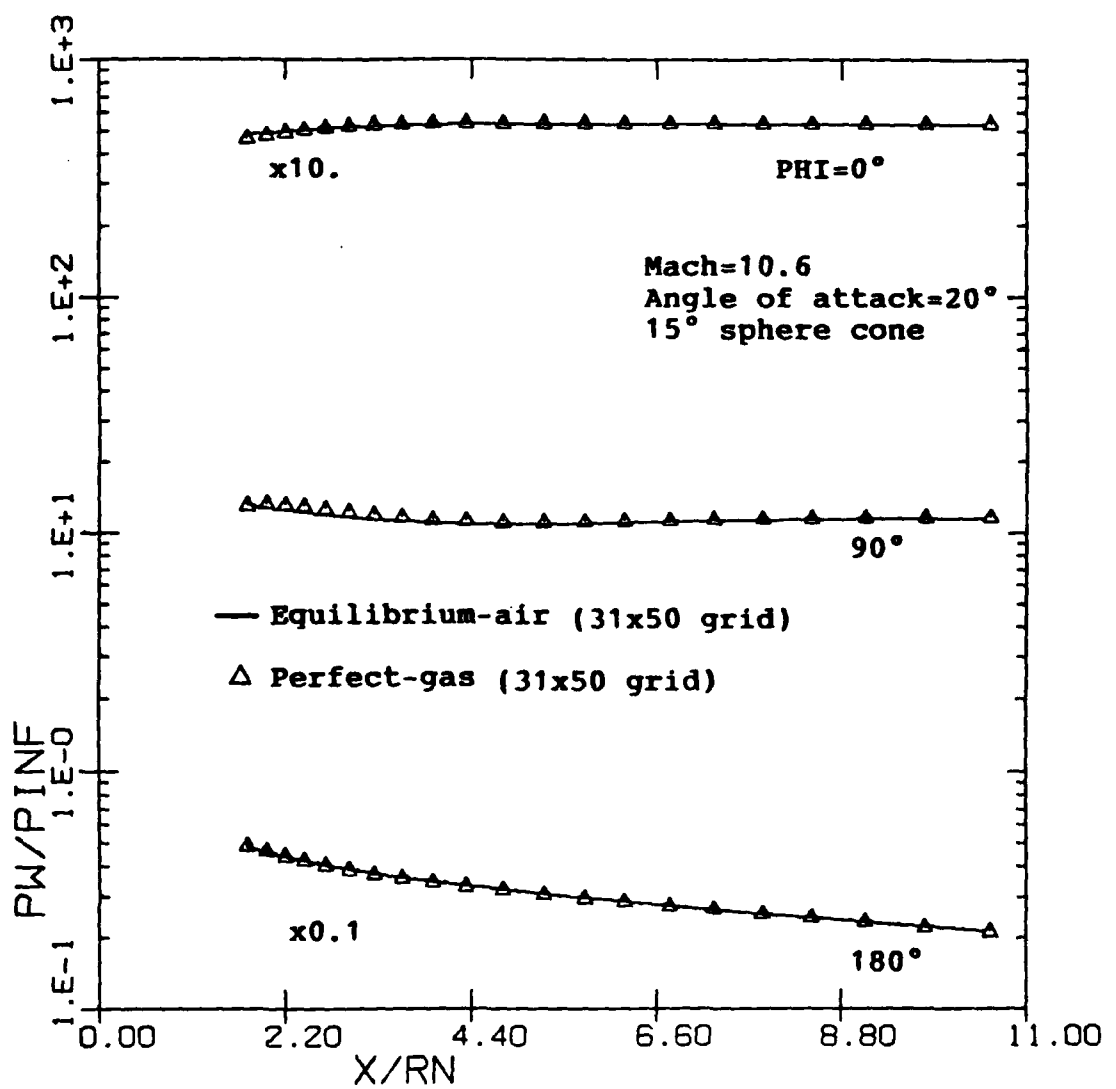


Figure 14. Effects of gas model on the axial distribution of wall pressures.

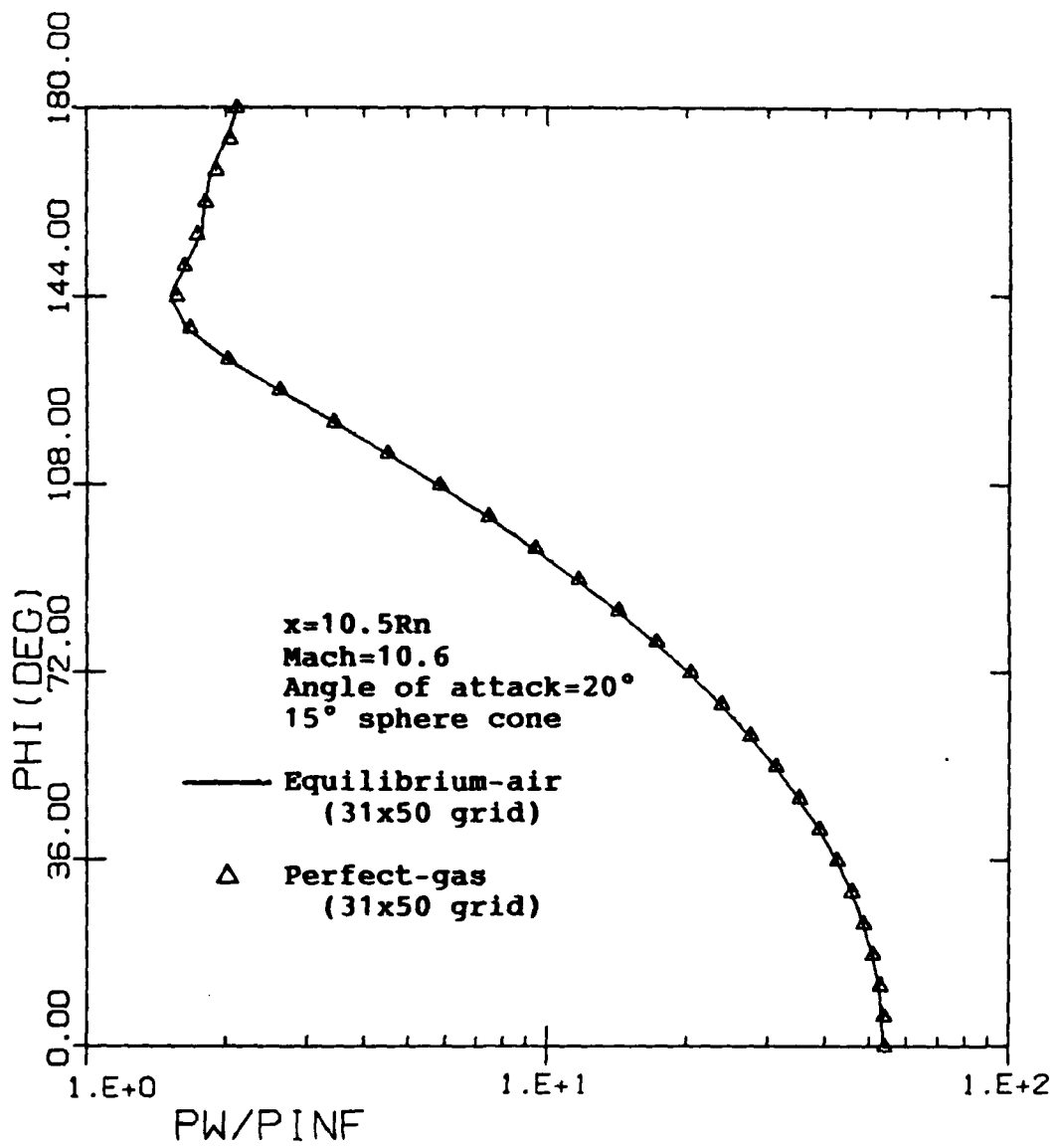


Figure 15. Effects of gas model on the crossflow distribution of wall pressures.

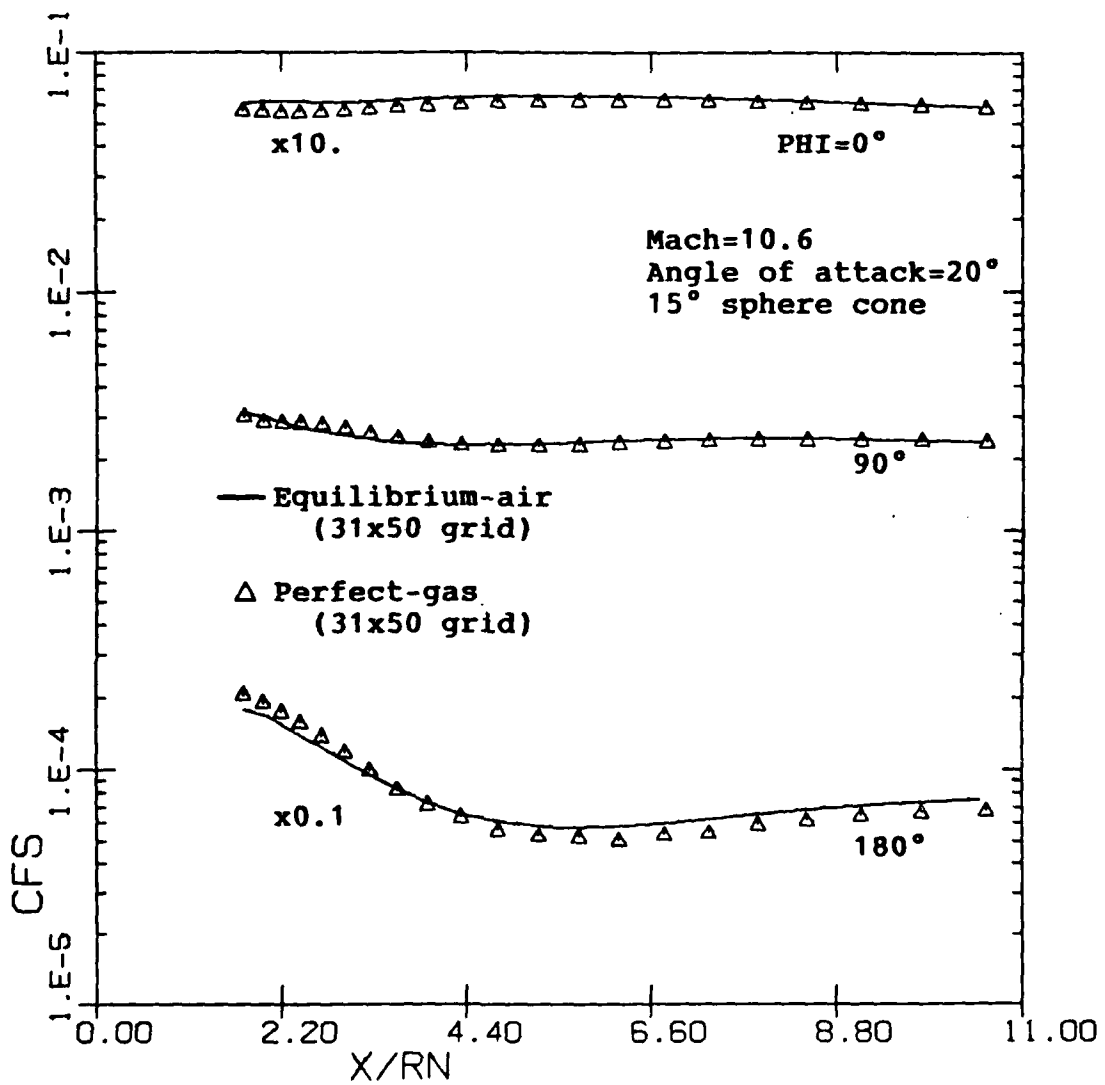


Figure 16. Effects of gas model on the axial distribution of the skin-friction coefficient.

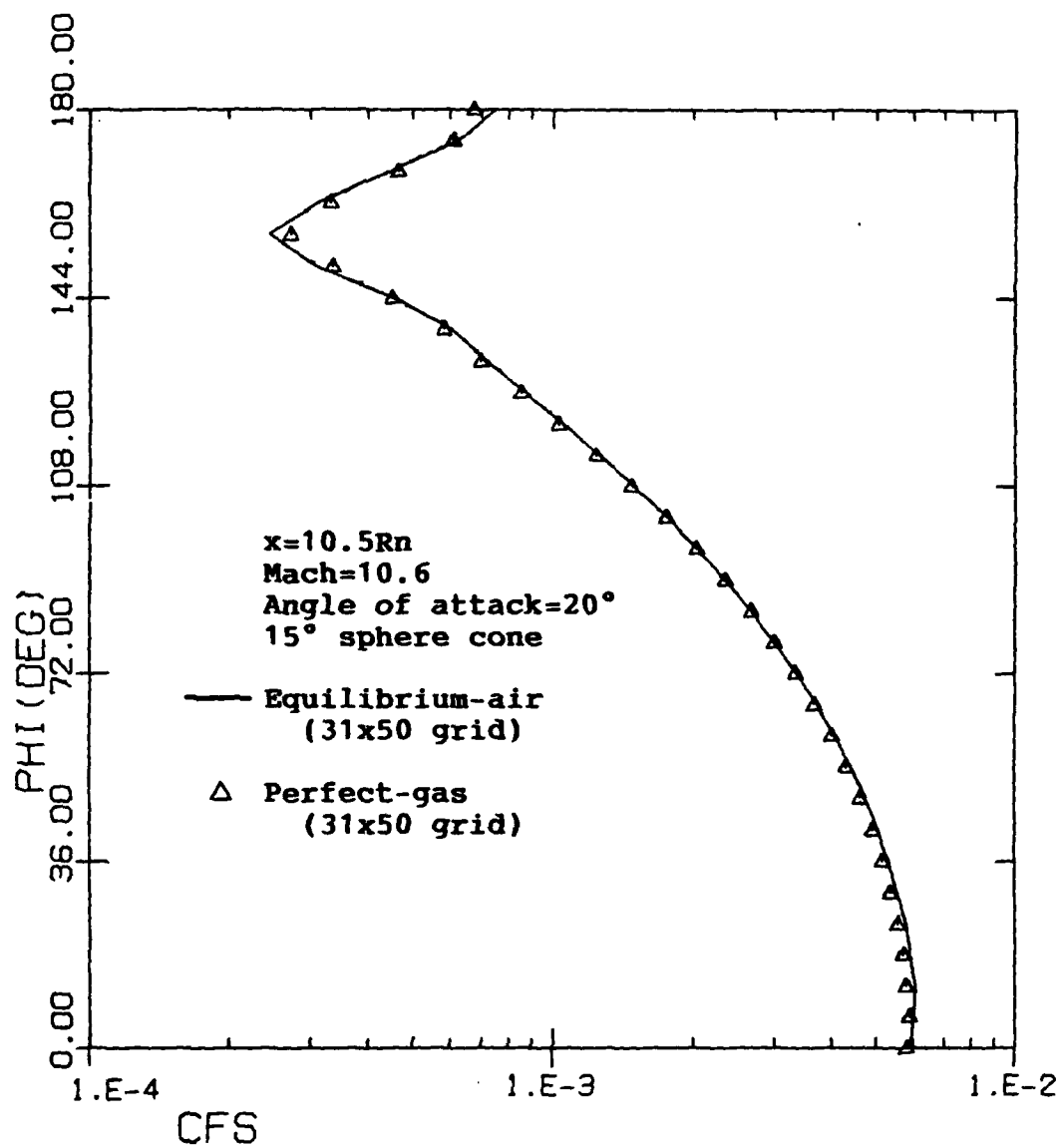


Figure 17. Effects of gas model on the crossflow distribution of the skin-friction coefficient.

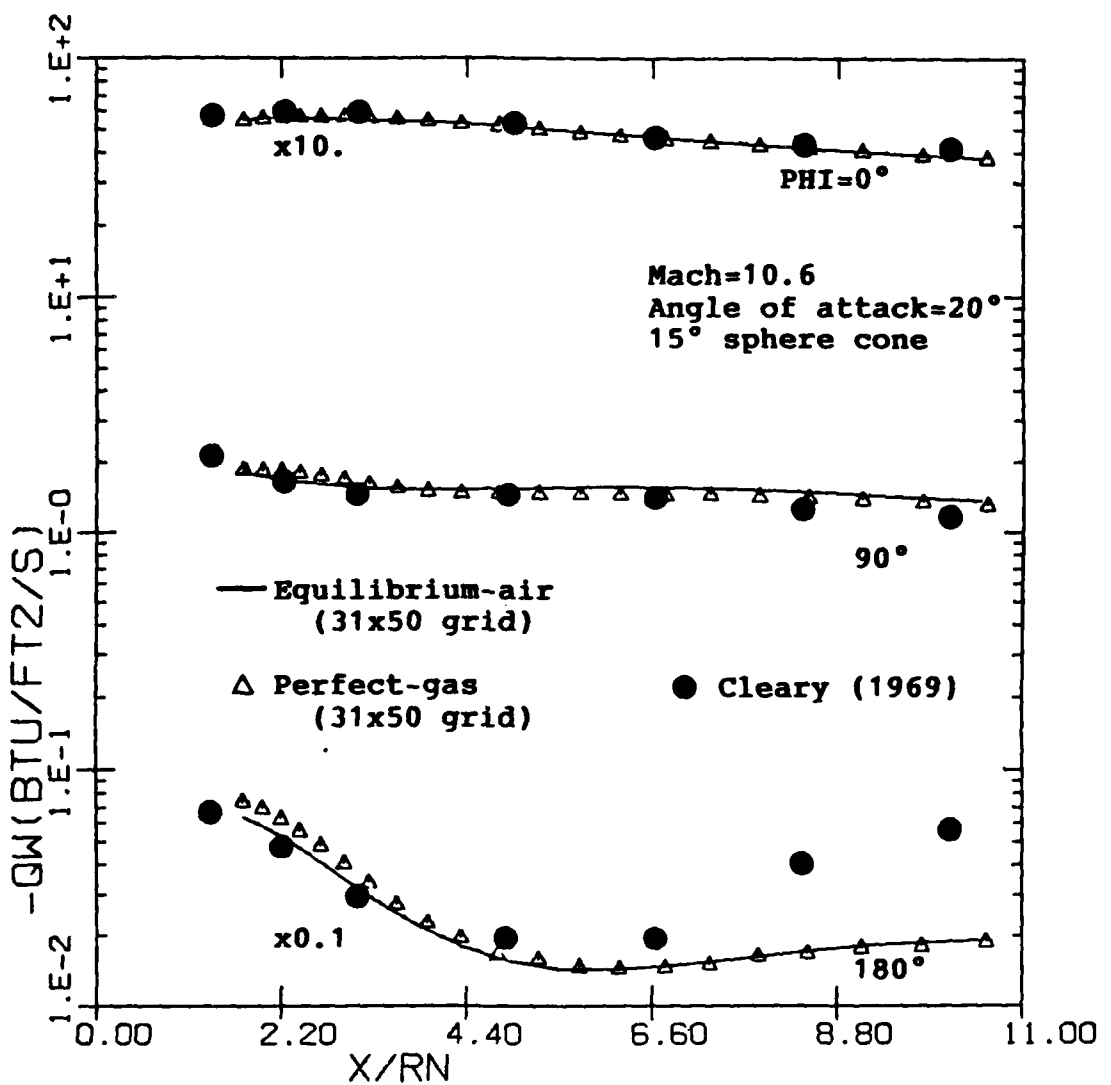


Figure 18. Effects of gas model on the axial distribution of the wall heat-transfer rates.

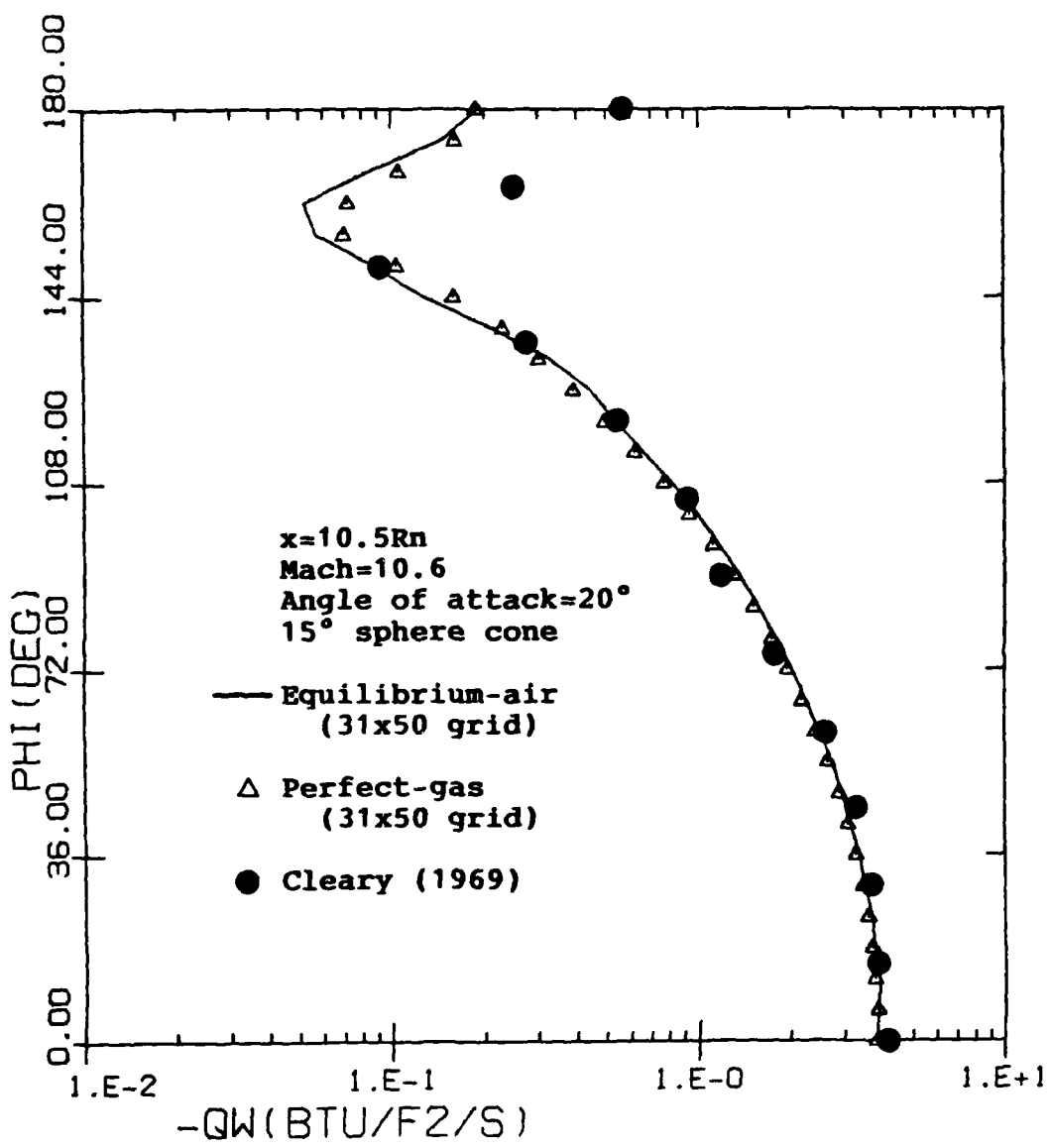


Figure 19. Effects of gas model on the crossflow distribution of the wall heat-transfer rates.

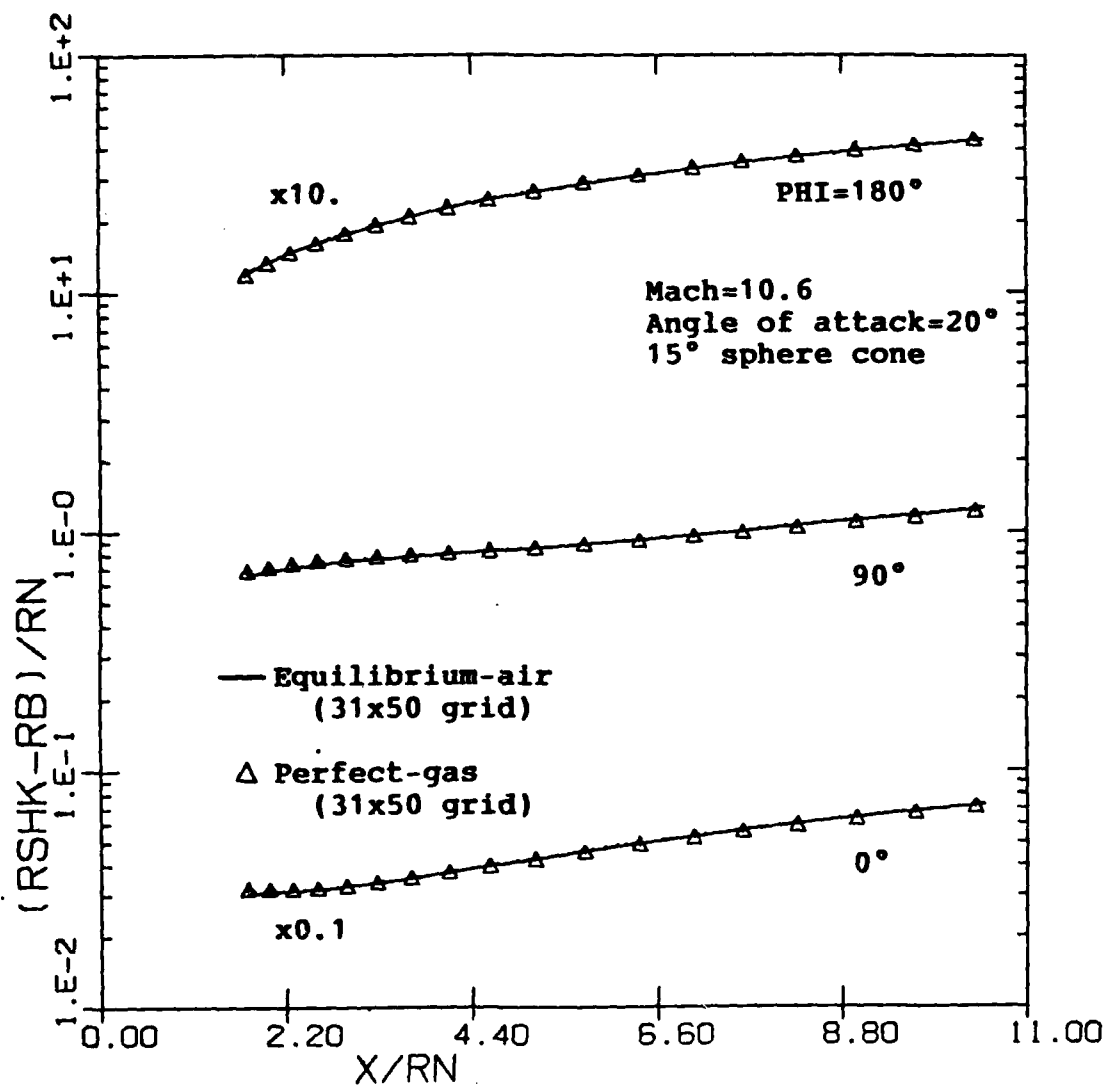


Figure 20. Effects of gas model on the axial variation of the bow shock shape.

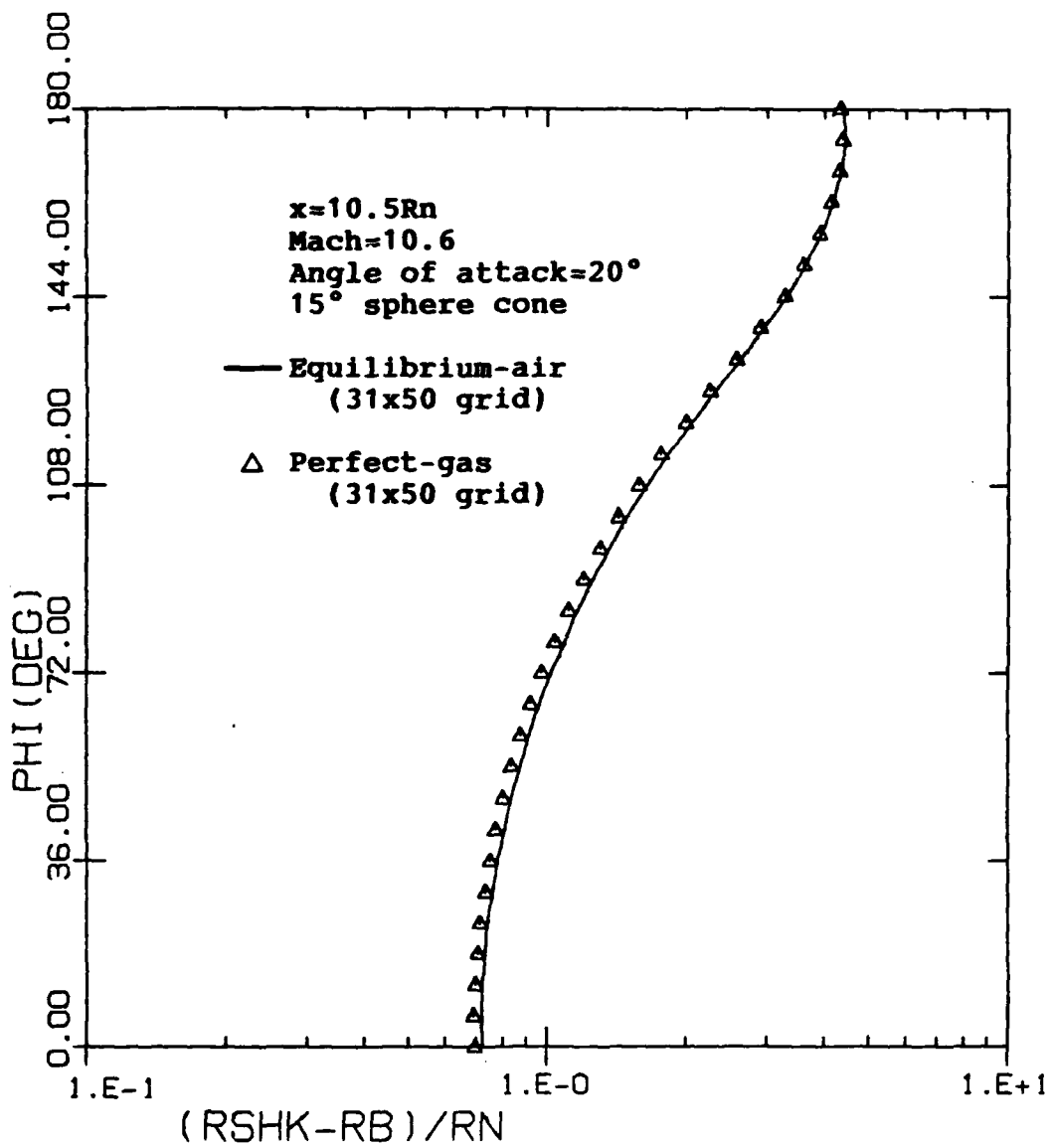


Figure 21. Effects of gas model on the crossflow variation of the bow shock shape.

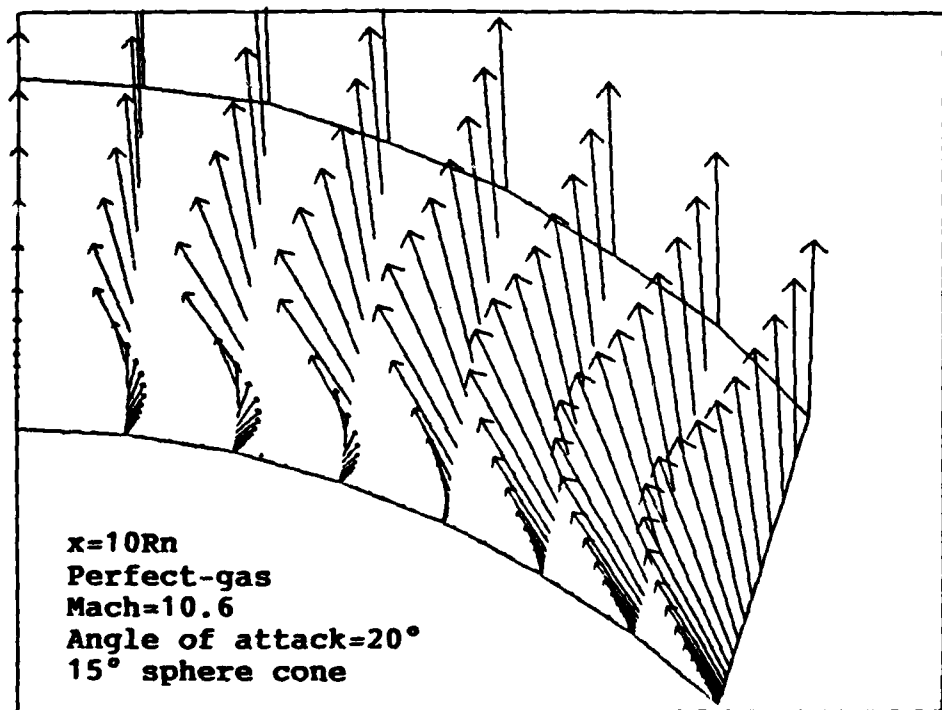


Figure 22. Crossflow separated region predicted with a perfect-gas model.

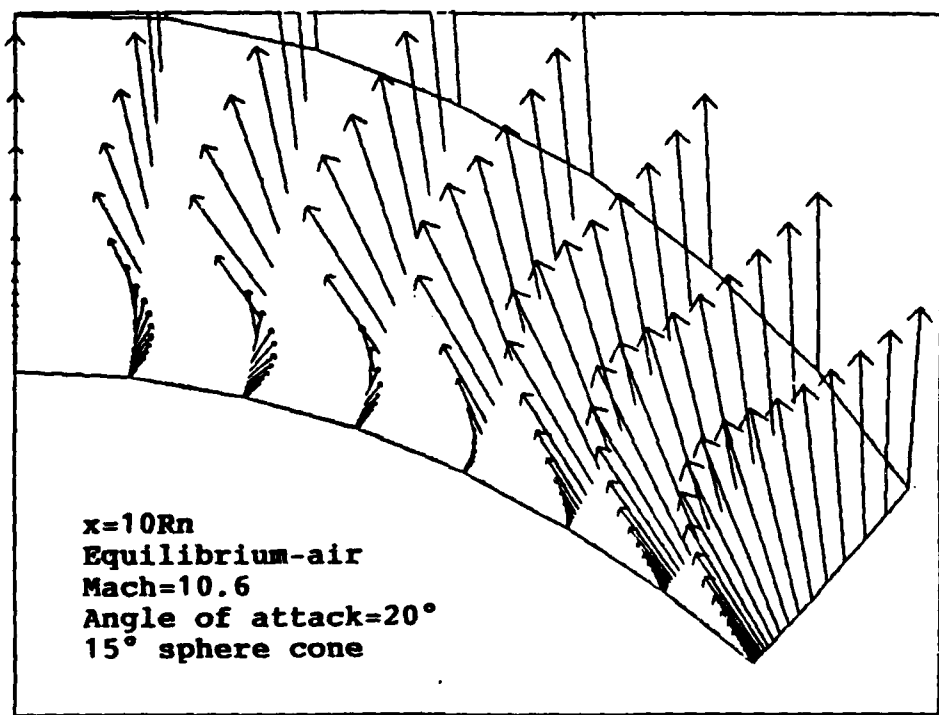
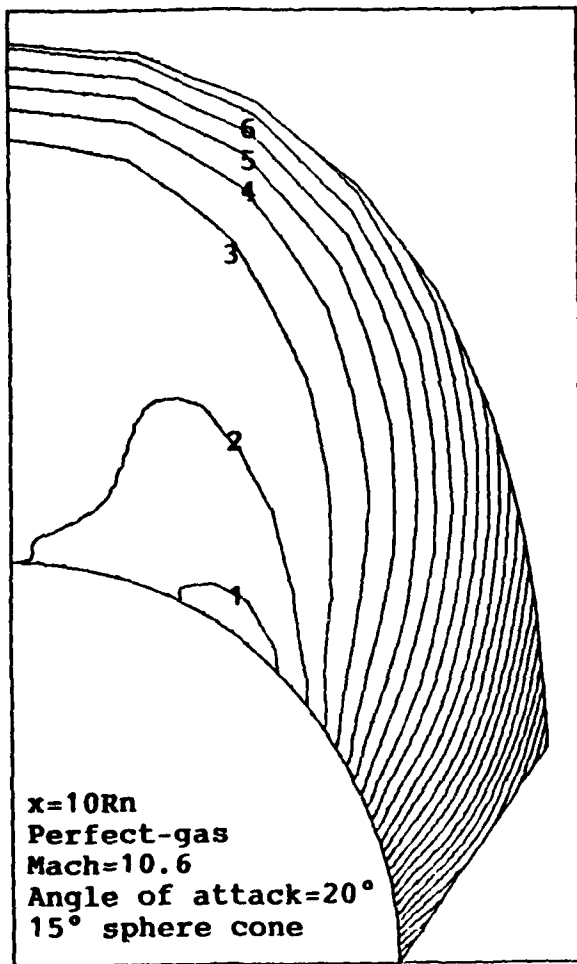


Figure 23. Crossflow separated region predicted with an equilibrium-air model.

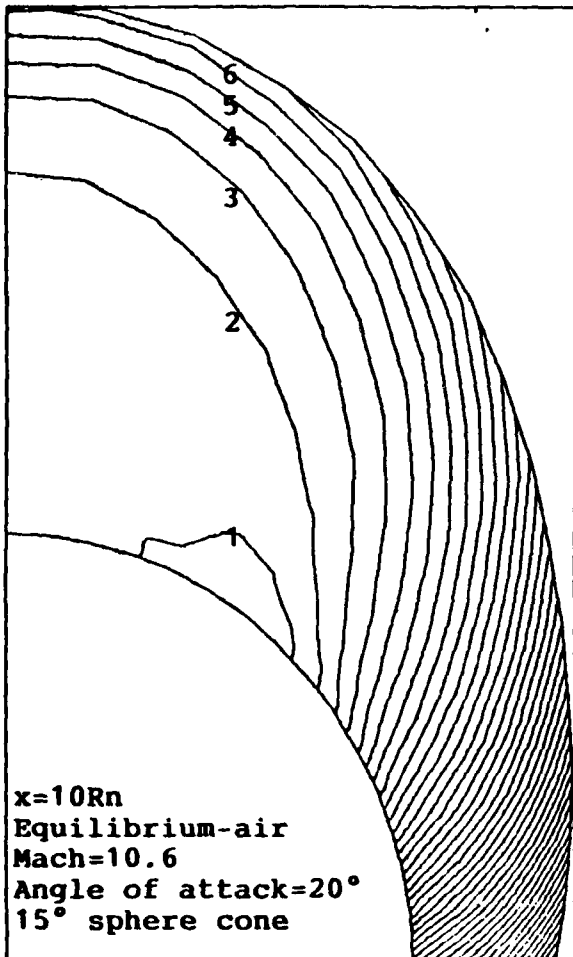


$$p_1 = 1.8 \times P_{\infty}$$

$$p_2 = 2.2 \times P_{\infty}$$

constant contour  
separation of  
0.4  $\times P_{\infty}$

Figure 24. Detailed leeward pressure contours predicted using a perfect-gas model.



$p_1=1.8 \times P_{\text{IN}}\text{F}$

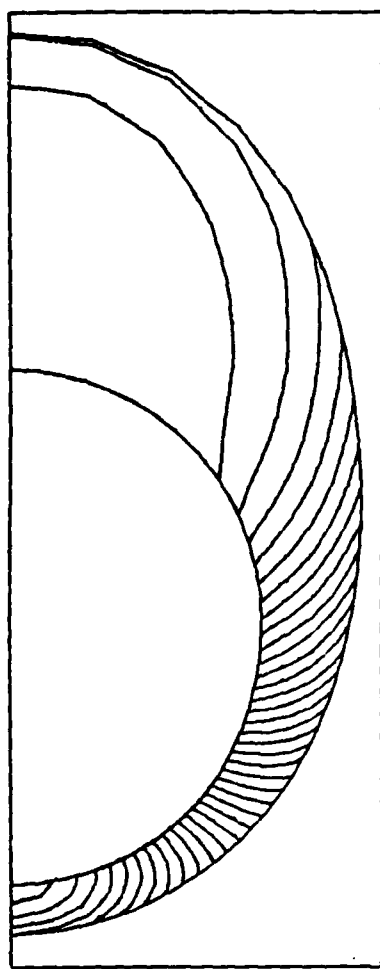
$p_2=2.2 \times P_{\text{IN}}\text{F}$

constant contour  
separation of  
 $0.4 \times P_{\text{IN}}\text{F}$

Figure 25. Detailed leeward pressure contours predicted using a equilibrium-air model.

(a)

$x=10R_n$   
Perfect-gas  
Mach=10.6  
Angle of attack=20°  
15° sphere cone



(b)

$x=10R_n$   
Equilibrium-air  
Mach=10.6  
Angle of attack=20°  
15° sphere cone

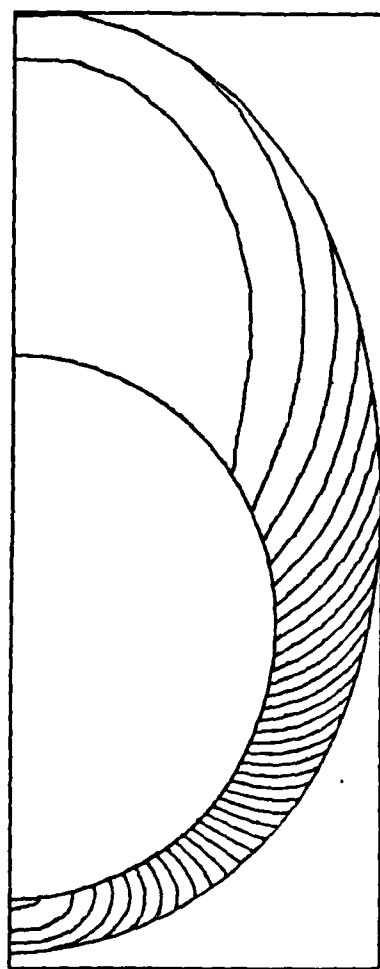
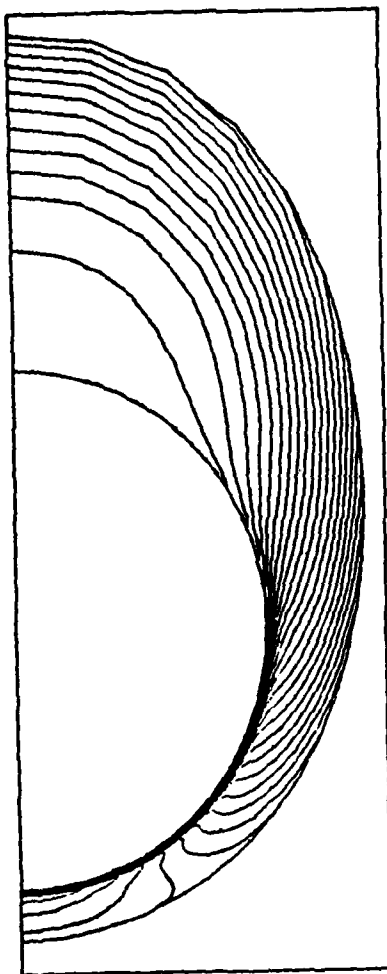


Figure 26. Effects of gas model on the crossflow pressure contours.

(a)

$x=10R_n$   
Perfect-gas  
Mach=10.6  
Angle of attack=20°  
15° sphere cone



(b)

$x=10R_n$   
Equilibrium-air  
Mach=10.6  
Angle of attack=20°  
15° sphere cone

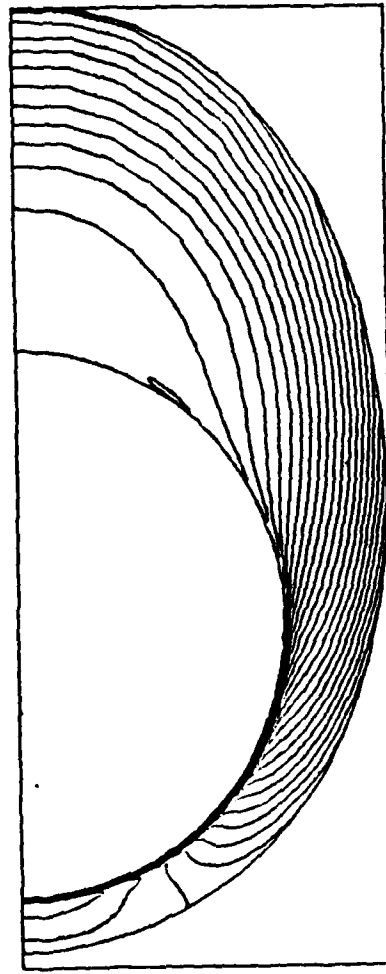
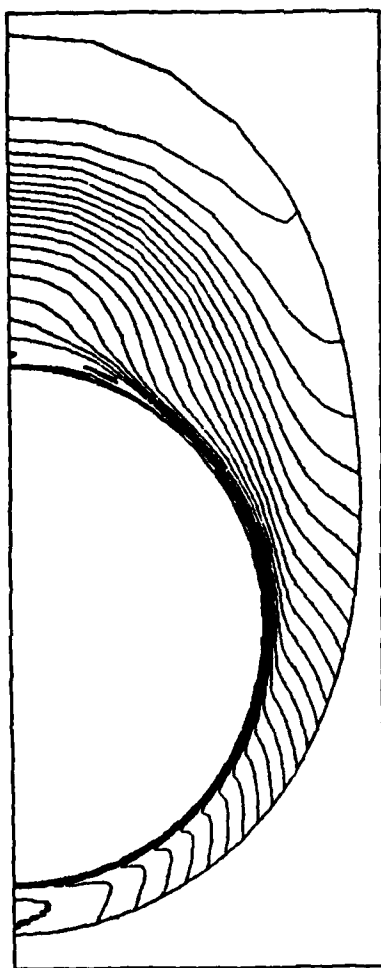


Figure 27. Effects of gas model on the crossflow temperature contours.

(a)

$x=10R_n$   
Perfect-gas  
Mach=10.6  
Angle of attack=20°  
15° sphere cone



(b)

$x=10R_n$   
Equilibrium-air  
Mach=10.6  
Angle of attack=20°  
15° sphere cone

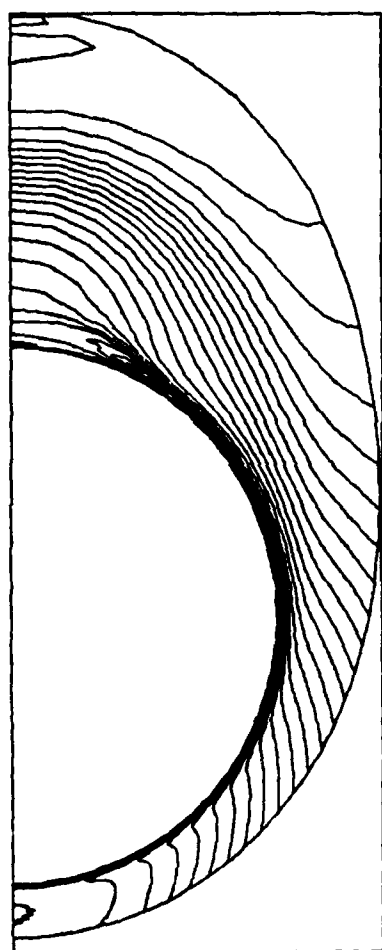


Figure 28. Effects of gas model on the crossflow density contours.